

AD-A019 525

CHAFF AERODYNAMICS

James Brunk, et al

Alpha Research, Incorporated

Prepared for:

Air Force Avionics Laboratory

November 1975

Reproduced From  
Best Available Copy

DISTRIBUTED BY:



National Technical Information Service  
U. S. DEPARTMENT OF COMMERCE

20000726029

## UNCLASSIFIED

SECURITY CLASSIFICATION OF THIS PAGE (When Data Entered)

REPORT DOCUMENTATION PAGE		READ INSTRUCTIONS BEFORE COMPLETING FORM
1. REPORT NUMBER <b>AFAL-TR-75-81</b>	2. GOVT ACCESSION NO.	3. RECIPIENT'S CATALOG NUMBER
4. TITLE (and Subtitle) <b>CHAFF AERODYNAMICS</b>		5. TYPE OF REPORT & PERIOD COVERED <b>Technical Report 11 Feb 74 to 11 Jan 75</b>
		6. PERFORMING ORG. REPORT NUMBER
7. AUTHOR(s) James Brunk Dennis Mihora Peter Jaffe		8. CONTRACT OR GRANT NUMBER(s) <b>F33615-74-C-1052</b>
9. PERFORMING ORGANIZATION NAME AND ADDRESS Alpha Research, Inc. Santa Barbara, CA 93105		10. PROGRAM ELEMENT, PROJECT, TASK AREA & WORK UNIT NUMBERS <b>62204F 7633 13 37</b>
11. CONTROLLING OFFICE NAME AND ADDRESS Air Force Avionics Laboratory 45433 Air Force Systems Command, WPAFB, OH		12. REPORT DATE <b>November 1975</b>
14. MONITORING AGENCY NAME & ADDRESS(if different from Controlling Office)		13. NUMBER OF PAGES <b>166</b>
		15. SECURITY CLASS. (of this report) <b>Unclassified</b>
		16a. DECLASSIFICATION/DOWNGRADING SCHEDULE
16. DISTRIBUTION STATEMENT (of this Report)  <b>Approved for public release; distribution unlimited.</b>		
17. DISTRIBUTION STATEMENT (of the abstract entered in Block 20, if different from Report)		
18. SUPPLEMENTARY NOTES		
19. KEY WORDS (Continue on reverse side if necessary and identify by block number) <b>Chaff, Aerodynamics, Chaff Force Coefficients, Chaff Moment Coefficients, Dynamics, Six Degrees of Freedom Chaff Simulator</b>		
20. ABSTRACT (Continue on reverse side if necessary and identify by block number)  The aerodynamic characteristics of thirteen distinct chaff dipole configurations were determined from drop tests of individual elements in a special enclosed test chamber. The dipole motion and trajectory were recorded by multi-image photographs taken by orthogonal still cameras equipped with specially designed synchronized rotating shutters.  The dynamic behavior and descent rate of the dipoles was found to (cont'd)		

DD FORM 1 JAN 73 1473 EDITION OF 1 NOV 68 IS OBSOLETE

1 UNCLASSIFIED  
SECURITY CLASSIFICATION OF THIS PAGE (When Data Entered)

UNCLASSIFIED

SECURITY CLASSIFICATION OF THIS PAGE(When Data Entered)

depend greatly upon the principal cross-section dimensions of the filaments.

Aerodynamic forces and moment coefficients for each dipole configuration were computed from the photographic multi-image motion data using photogrammetric and aerodynamic data reduction programs developed as part of the effort. The resulting aerodynamic coefficient data were successfully correlated with Reynolds number, angle of attack, and various other parameters. While the force coefficients were found to be large and in general agreement with the various theories for creeping flow, the moment coefficients were extremely small and resulted primarily from configurational asymmetries.

Using both the experimental data and theory, aerodynamic coefficient tables for representative dipole configurations, suitable for 6-DOF simulation of dipole motion, were prepared. These aerodynamic data were subsequently used in conjunction with a 6-DOF Monte Carlo trajectory program, modified for inclusion of stochastic atmospheric turbulence, for preliminary simulations of chaff dipole motion in both quiescent and turbulent atmospheres.

Turbulence was found to have a large effect on the translational motion of the dipole, but only a small effect on its angular motion.

1(a)

UNCLASSIFIED

SECURITY CLASSIFICATION OF THIS PAGE(When Data Entered)

## FOREWORD

This final report documents work accomplished during the period 11 February 1974 through 11 January 1975 by Alpha Research, Inc., Santa Barbara, California under Contract F33615-74-C-1052, Project 7633, Task 13, (Chaff Aerodynamics) with the Air Force Avionics Laboratory, Wright-Patterson AFB, Ohio. The project monitor for the Air Force was Mr. Vittal Pyati (AFAL/WRP).

The principal investigator for the contractor was Mr. James E. Brunk. The test program was accomplished by sub-contract with Astro Research Corporation, under the direction of Mr. Dennis Mihora. Mr. Peter Jaffe provided aerodynamic consultant services. Computer program modifications were supervised by Mr. William Davidson. Mr. James Christ assisted with the aerodynamic data processing. This report was submitted in May 1975.

The report is unclassified.

## TABLE OF CONTENTS

<u>Section</u>	<u>Page</u>
I. Introduction	1
II. Test Facilities	4
1. Enclosed Test Chamber	4
2. Instrumentation and Equipment	6
3. MCAS Drop Facility	8
III. Test Articles	13
IV. Test Conditions and Procedures	17
1. Photogrammetric Calibration	17
2. Development of Photographic Procedure	17
3. Investigation of Test Chamber Air Currents	20
4. Dipole Steady-State Tests	20
5. Dipole Transient Motion Tests	20
6. Special Investigations of Chaff Dynamics	21
V. Data Reduction	23
1. Photographic Data Processing	23
2. Dipole Trajectory and Motion Data	23
3. Aerodynamic Data Reduction	23
VI. Results	28
1. A Qualitative View of Chaff Dipole Dynamics	28
2. Quantitative Analysis of Dipole Dynamics	31
3. Aerodynamic Coefficient Correlations	36
4. Chaff Cluster Dispersion Tests	52
VII. Six-Degrees-of-Freedom Motion Simulations	58
1. 6-DOF Computer Program	58
2. Aerodynamic Coefficient Data	59
3. Coefficient Tables for Alternate Chaff Lengths	66
4. Monte Carlo Simulations	68
5. Simulation of Dipole Flight in a Turbulent Atmosphere	68
VIII. Summary, Conclusions, and Recommendations	72

Preceding page blank

**TABLE OF CONTENTS (Concluded)**

<u>Appendix</u>		<u>Page</u>
<b>A</b>	<b>Photogrammetric Data Reduction</b>	<b>74</b>
1.	Determination of Dipole Position and Attitude (Cameras 1 and 3)	74
2.	Determination of Dipole Position and Attitude (Cameras 1 and 2)	81
3.	Calibration	82
4.	Computer Program	83
<b>B</b>	<b>Aerodynamic Data Reduction Program</b>	<b>84</b>
1.	Data Input and Smoothing	84
2.	Angle of Attack and Flight Path Angles	86
3.	Aerodynamic Forces	89
4.	Aerodynamic Moments	89
<b>C</b>	<b>Chaff Aerodynamic Theory</b>	<b>92</b>
1.	Theoretical Aerodynamics of Symmetric Dipole at Low Reynolds Number	92
2.	Aerodynamic Forces Acting Upon a Symmetric Dipole	100
3.	Aerodynamic Characteristics of an Asymmetric Dipole	107
4.	Aerodynamic Damping	115
5.	Spiral Dynamics	119
<b>D</b>	<b>Isotropic Turbulence</b>	<b>124</b>
1.	Eulerian Coordinates	124
2.	Lagrangian Coordinates	129
3.	Joint Correlation Functions	130
4.	Numerical Modeling	132
<b>E</b>	<b>Atmospheric Turbulence Data</b>	<b>136</b>
1.	Single Valued Turbulence	136
2.	Turbulence as a Function of Altitude	141
<b>References</b>		<b>146-149</b>

## LIST OF ILLUSTRATIONS

Figure	Title	Page
1	Chaff Aerodynamic Test Chamber	5
2	Camera System and Rotating Shutter	7
3	Schematic of Rotating Shutter System	9
4	Filament Holder/Release Mechanism	10
5	Chaff Filament Holder Assembly	11
6	Relationship Between Dipole Image Size and Film Resolution	18
7	Multi-Image Photography of 2-mil x 2-inch Dipole	24
8	Multi-Image Photography of .006 x .00045 x .36-inch Dipole	25
9	Multi-Image Photography of .040-Inch Width Dipole from Camera Positions 1 and 3	26
10	Spiral Rate Statistics	29
11	Multi-Image Photography of .040-Inch Width Dipoles in Autorotative Motion	32
12	Vertical View of Typical Dipole Trajectory	33
13	Time Histories of Motion Parameters and Aerodynamic Normal Force and Axial Force Coefficients for a Typical Dipole	34
14	Time Histories of Motion Parameters, Aerodynamic Side Force Coefficient, and Aerodynamic Moment Coefficients for a Typical Dipole	35
15	Correlation of Descent Angle, $\gamma$ , with Angle of Attack, $\alpha$	37
16	Aerodynamic Force and Moment Coefficient Definitions	38
17	Correlation of Normal Force Coefficient with Reynolds Number for Large Angle of Attack ( $\alpha > 80$ deg)	40

**LIST OF ILLUSTRATIONS (Continued)**

Figure	Title	Page
18	<b>Correlation of Axial Force Coefficient with Reynolds Number for Small Angle of Attack Motions (<math>\alpha &lt; 30</math> deg)</b>	42
19	<b>Correlation of Normal Force Coefficient Parameter <math>C_N \cdot U</math> with Angle of Attack (Glass-Type Dipoles)</b>	44
20	<b>Correlation of Normal Force Coefficient Parameter <math>C_N \cdot U</math> with Angle of Attack (Foil-Type Dipoles)</b>	45
21	<b>Correlation of Axial Force Coefficient Parameter <math>C_A \cdot U</math> with Angle of Attack (Foil-Type Dipoles)</b>	47
22	<b>Correlation of Side Force Coefficient with Normal Force Coefficient for Foil-Type Dipoles</b>	48
23	<b>Correlation of Static Overturning Moment Coefficient and Static Side Moment Coefficient with Angle of Attack</b>	51
24	<b>Ground-Level Dispersion Patterns for Small Chord Foil-Type Dipole as a Function of Release Height</b>	53-55
25	<b>Probable Radial Dispersion from Mean Center of Impact as a Function of Cluster Release Height (Foil-Type Dipoles)</b>	56
26	<b>Monte Carlo Trajectory Simulation for .006 x .00045 x 1.78-inch Foil-Type Dipole (Zero Wind)</b>	69
27	<b>Motion Simulation with Representative Low Altitude Turbulence (.006 x .00045 x 1.78-inch Foil-Type Dipole)</b>	71
A-1	<b>Coordinate System for Motion Recording Cameras</b>	75
B-1	<b>Euler Angle Notation</b>	85
B-2	<b>Polar Coordinates</b>	85
B-3	<b>Angle of Attack Parameters</b>	87
B-4	<b>Flight Path Parameters</b>	87
B-5	<b>Definition of Angle <math>\bar{\phi}</math></b>	88
E-6	<b>Force Vector Definitions</b>	90
B-7	<b>Moment Vector Definitions</b>	90

**LIST OF ILLUSTRATIONS (Concluded)**

Figure	Title	Page
C-1	<b>Effect of Chaff Size on Reynolds Number for Steady Descent (Sea Level Conditions)</b>	95
C-2	<b>Drag Parameters of Long Cylinder in Axial Flow</b>	102
C-3	<b>Aerodynamic Force Notation for Foil-Type Dipole</b>	105
C-4	<b>Effect of Chaff Orientation Parameter <math>\phi</math> on Section Lift and Drag Coefficients (2-Dimensional Flat Plate Theory)</b>	106
C-5	<b>Schematic of Aerodynamic Moment Due to Axial Viscous Force (Dipole with Longitudinal Bend)</b>	110
C-6	<b>Schematic of Aerodynamic Moment Due to Normal Force (Dipole with Longitudinal Bend)</b>	112
C-7	<b>Asymmetric Dipole Configurations</b>	113
C-8	<b>Schematic of Forces and Moments Acting Upon a Spiraling Dipole</b>	120
C-9	<b>Schematic of Dipole Dispersion Due to Steady Spiral</b>	123
D-1	<b>Reference Coordinates and Turbulent Velocity Components</b>	126
E-1	<b>Theoretical Mixture of Gaussian Amplitudes of Medium Altitude Atmospheric Turbulence</b>	139
E-2	<b>Power Spectral Density of Turbulent Spectrum; Comparing Dryden Formulation to MEDCAT Data</b>	140
E-3	<b>The Nominal Intensity of Turbulent Fluctuations as a Function of Altitude</b>	142
E-4	<b>Turbulent Scale Length Variations with Altitude in Neutral Stability Over Flat Terrain</b>	144

## LIST OF TABLES

Table	Title	Page
1	Designation of Chaff Types	14
2	Chaff Dipole Weight and Inertia Summary	16
3	Basic Aeroballistic Coefficient for Cylindrical Glass Dipole (.001 x 1.0 Inches); and Moment Coefficients Due to Bending	60-61
4	Basic Aeroballistic Coefficients for Foil Dipole (.006 x .00045 x 1.78 Inches); and Additional Body-Fixed Coefficients for Foil Dipole	63-64
5	Summary of Aerodynamic Constants for Computing Coefficient Functional Dependence Upon $\dot{\alpha}$ and $\dot{\phi}$	67
C-1	Characteristic Functional Dependence of Dipole Aerodynamic Coefficients on $\dot{\alpha}$ and $\dot{\phi}$	114
E-1	Compiled Data on Medium Altitude Turbulence Properties	137
E-2	Turbulence Parameters with Neutrally Stable Conditions Used in the Computer Namelist Input	145

## LIST OF SYMBOLS

$a$	fraction of steady-state descent velocity, Equation (1)
$a$	body dimensional parameter (Appendix C)
$b, c$	radius of cylindrical body, Equations (C-14) and C-9)
$c$	width of foil-type dipole
$C$	ratio of minimum to maximum normal force
$CF$	centrifugal force
$C_A$	axial force coefficient
$C_D$	drag coefficient
$C_{Df}, C_{Dv}$	friction or viscous drag coefficient
$C_L$	lift coefficient
$C_l$	rolling moment coefficient
$\Delta C_l$	rolling moment coefficient contribution due to $\phi$
$C_{l\phi_1}$	harmonic coefficient for roll dependency (Equation 19)
$C_{l\rho}$	roll damping coefficient based on $\rho l/2V$
$C_{l\delta}$	rolling moment coefficient due to twist
$C_N$	normal force coefficient
$\Delta C_N$	normal force coefficient contribution due to $\phi$
$C_{N1}$	harmonic coefficient for roll dependency (Equation 15)
$\bar{C}_N$	modified normal force coefficient; $\frac{(C_N)\pi/2}{V}$
$C_{Np}$	magnus force coefficient (Equation 9)
$C_n$	coefficient for yawing moment due to angular rotation $r$
$C_{nr}$	damping coefficient for side moment plane based on $rl/2V$
$C_M$	overturning moment coefficient (pitch plane)
$\Delta C_M$	pitching moment coefficient contribution due to $\phi$
$C_{M1}$	harmonic coefficient for roll dependency (Equation 17)
$C_{M\delta}$	pitching moment coefficient due to longitudinal bend
$C_{Mq}$	damping coefficient for angle of attack plane based on $ql/2V$
$C_{SF}$	side force coefficient

## LIST OF SYMBOLS (Continued)

$\Delta C_{SF}$	side force contribution due to $\Phi$
$C_{SF_1}$	harmonic coefficient for roll dependency (Equation 16)
$C_{SM}$	side moment coefficient
$\Delta C_{SM}$	side moment coefficient due to $\Phi$
$C_{SM_1}, C_{SM_2}$	harmonic coefficients for roll dependency (Equation 18)
$d$	dipole diameter
$F$	aerodynamic force
$F_x, F_y, F_z$	aerodynamic force vectors in xyz coordinates
$F_N$	normal force
$F_S$	side force
$F_v$	viscous force on slender dipole in axial flow
$F_T$	viscous force per unit length
$g$	acceleration due to gravity
$G, H, J$	Gaussian random numbers with zero mean and standard deviation $\sigma$ (Appendix D)
$h$	altitude
$h_1$	descent distance for one complete spiral (Appendix C)
$i$	turbulence intensity (Appendix D, E)
$I_x$	axial moment of inertia
$I_y, I_z$	transverse moments of inertia
$k$	functional aerodynamic force coefficient (Table C-1)
$K$	functional aerodynamic moment coefficient (Table C-1)
$K_1$	spacial wave number (Appendix D)
$K_1, K_2, K_3$	factors for resistance tensor (Equation C-9)
$\bar{K}$	ratio of resistance factors (Equation C-13)
$l$	dipole length (aerodynamic reference length)
$L, M, N$	aerodynamic moment vectors in xyz coordinates
$m$	dipole mass
$M_S, SM$	side moment (Appendix B, C)

### LIST OF SYMBOLS (Continued)

$M_N$	overturning moment (Appendix B)
$M_x$	rolling moment (Appendix B)
$n$	shedding frequency of flow (Appendix C)
$\rho$	angular velocity about dipole $x$ axis (roll rate)
$P, Q, R$	history functions in regression analysis (Appendix D)
$q$	angular velocity about dipole $y$ axis (pitch rate)
$q$	dynamic pressure
$r$	angular velocity about dipole $z$ axis (yaw rate)
$r$	radial dispersion from release point
$\bar{r}$	probable radial dispersion from mean center of impact (50th percentile)
$R$	radial position parameter for polar coordinates (Equation B-2)
$R$	radius of longitudinal bend
$R$	radius of spiral (Figure C-8)
$R$	correlation function (Appendix D)
$R_N$	Reynolds number
$s$	descent distance, Equation (1)
$s$	displacement along dipole with longitudinal bend
$S$	aerodynamic reference area (see Figure 17)
$S$	Strouhal number (Appendix C)
$\bar{S}$	parameter for theoretical aerodynamic coefficients; Equations (C-19) and (C-20)
$t$	time
$t$	thickness of foil-type dipole
$u, v, w$	dipole velocity components along $xyz$ moving coordinates
$u_a, v_a, w_a$	aerodynamic velocity components of dipole
$U$	dipole velocity
$U, V, W$	velocity components of turbulence (Appendix D)
$U_A, U_N$	axial and normal velocity components (Figure C-3)

LIST OF SYMBOLS (Continued)

$v$	dipole velocity (Appendix B, C)
$v_i$	induced velocity at element along dipole longitudinal axis
$w$	dipole density
$W$	dipole weight
$x, y, z$	coordinate axes moving with dipole (Figure B-1)
$\Delta x, \Delta y, \Delta z$	displacement of dipole geometric and mass centroids
$X, Y, Z$	coordinate axes of inertial reference system
$X_0, Y_0$	coordinate axes referenced to center of spiral (Appendix B)
$\bar{X}, \bar{Y}$	coordinates of center of spiral (Appendix B)
$X_w$	mean wind velocity in direction of $X$ inertial axis
$\alpha$	angle of attack
$\hat{\alpha}$	total angle of attack
$\alpha_T$	trim angle of attack
$\alpha_R$	reference angle of attack (Appendix C)
$\alpha_l$	dipole image attitude on film (Appendix A)
$\beta$	time scaling ratio, $\tau_L/\tau_E$ (Appendix D)
$\gamma$	flight path descent angle (from horizontal), Euler's constant
$\bar{\gamma}$	flight path descent angle (from vertical)
$\delta$	deflection parameter for asymmetric surfaces
$\delta$	center of mass offset of dipole with longitudinal bend
$\epsilon$	dipole twist
$\zeta_1$	parameter for photogrammetric analysis (Appendix A)
$n_1$	parameter for photogrammetric analysis (Appendix A)
$\theta$	Euler orientation angle; elevation
$\theta$	angular displacement parameter for dipole with longitudinal bend (Appendix C)
$\Theta$	drag parameter (Figure C-2)
$\theta_o$	camera alignment angle (Appendix A)

## LIST OF SYMBOLS (Continued)

$\mu$	viscosity of air
$\nu$	kinematic viscosity
$\nu$	angular position parameter for polar coordinates (Equation B-1)
$\xi$	angle of attack plane orientation parameter (Figure B-3)
$\rho$	air density
$\rho$	linear separation distance (Appendix D)
$\sigma$	standard deviation of turbulent wind (Appendix D, E)
$\tau$	time constant (Appendix D)
$\tau_L$	Langrangian-integral-scale length of turbulence (Appendix D)
$\phi$	dipole Euler angle for photogrammetric data reduction
$\bar{\phi}$	angle of attack plane parameter (Figure B-5)
$\dot{\phi}$	dipole aerodynamic roll angle (Figure C-3)
$\Phi$	power spectral density (Appendix D)
$\psi$	Euler orientation angle, azimuth (Figure B-1)
$\Psi$	flight heading angle; azimuth
$\omega$	dipole autorotation velocity about longitudinal axis
$\omega$	wave frequency (Appendix D)
$\Omega$	spiralling rate during dipole descent
$\Omega$	spacial wave frequency (Appendix D)

### Subscripts and Superscripts

$(\ )_{ss}$	steady-state
$(^*)$	time derivative
$(\ )_{\pi/2}$	evaluated at $\dot{\alpha} = \pi/2$
$(\ )'$	denotes variable related to turbulent components (Appendix D)
$(\overline{\ })$	stochastic average (Appendix D)
$(\ )_l$	longitudinal component (Appendix D)

**LIST OF SYMBOLS (Concluded)**

( ) <sub>L</sub>	Lagrangian (Appendix D)
( ) <sub>E</sub>	Eulerian (Appendix D)
( ) <sub>o</sub>	reference or nondimensional (Appendix D, E)
( ) <sub>w</sub>	wind value

## SECTION I

### INTRODUCTION

Chaff, as a broad band passive electromagnetic countermeasure, has found extensive use since World War II. Apart from slip coating to help separation and strip coating to assure different orientations under free-fall, no systematic effort has been made to improve the performance of atmospheric chaff clouds taking into account the unique flight performance characteristics of the elements themselves. Before chaff improvements can be initiated in a logical and orderly manner, the dynamic behavior of the chaff dipoles must be fully understood and the means for predicting the dipole trajectory and angular motion during both short and long time spans must also be available.

Chaff dipoles, because of their extremely small cross-sectional dimensions and great slenderness, possess unusual flight characteristics. The flight Reynolds number, which is of the order of unity, approaches the Stokes flow regime at the lowest Reynolds number, and the transitional regime where fluid vortices are formed at the largest flight Reynolds numbers. The extremely slow descent rate of chaff elements (which is of the order of 1 FPS) makes them highly sensitive to small air currents and turbulence.

The present effort was undertaken for the purpose of 1) detailed measurement of the motion and aerodynamic coefficients of individual chaff dipoles provided by the Air Force Avionics Laboratory, 2) determining the effect of dipole configuration on the characteristic aerodynamic parameters, and 3) for development of a 6-DOF (six-degrees-of-freedom) trajectory simulation model for prediction of dipole motion in the presence of realistic winds and turbulence.

A prior study of chaff cloud dynamics, as affected by the dipole aerodynamic characteristics, is described in Reference 1. Although Reference 1 reports on the aerodynamic properties of a single representative foil-type dipole, insufficient aerodynamic coefficient data were determined to permit 6-DOF type motion simulations.

---

<sup>1</sup> Avrin, J. S. & M. V. McCafferty, The KMS Technology Center, "Chaff Cloud Dynamics," Air Force Avionics Laboratory, Wright-Patterson AFB, Ohio, Report No. AFAL-TR-73-286, September 1973.

The experimental measurement of dipole aerodynamic characteristics presents several problems both as a result of the small dipole size (minimum diameter of 0.001 inches) and the sensitivity of the dipole motion to small air currents. Because of these factors it was concluded at the outset of the program that special test facilities, test procedures, and photographic techniques would be required to accurately measure the chaff motion and the associated aerodynamic forces and moments. As a result, a unique fully-enclosed drop test chamber was fabricated, with an integral lighting and photographic documentation system.

To document the dipole motion, three orthogonally aligned still cameras, each equipped with a specially designed synchronous rotating shutter, was provided in three cells attached to the main drop chamber. This method of multi-image photography, using single film negatives, was preferred over conventional motion pictures because of the greater flexibility, simplified data processing, and improved accuracy.

Satisfactory illumination of the dipoles in flight was a significant problem and required considerable development effort with regard to lighting, baffling, exposure control, and film selection and processing.

A total of 262 separate documentary tests were accomplished in the aerodynamic test chamber, using 13 dipole configurations differing in construction, cross-section, and length.

Aerodynamic data reduction and analysis were accomplished in two phases. In the first phase the dipole trajectory and attitude was determined as a function of time. In the second phase the motion parameters, including all velocity and acceleration components, were obtained by moving polynomial-arc smoothing and differentiation formulas, and subsequently the total aerodynamic force and moment coefficients were computed from the solution of the applicable equations of motion. The aerodynamic coefficient dependence upon angle-of-attack and Reynolds number was determined by data correlation techniques.

To complement the experimental aerodynamic analysis a comprehensive theoretical analysis of chaff dipole aerodynamics was undertaken. These analyses provided a means for estimating the effects of dipole roll orientation, configurational asymmetry and aerodynamic damping, which could not be determined experimentally.

A significant part of the present effort was devoted to the development of a 6-DOF computer program and simulation capability. This was accomplished by adaptation of an existing comprehensive 6-DOF program

incorporating a Monte Carlo option for selection of the initial conditions and body physical parameters. The principal additions to the existing program were 1) a stochastic atmospheric turbulence model, and 2) provision for aerodynamic coefficient Reynolds number dependency.

Preliminary 6-DOF motion simulations were accomplished for representative dipole configurations to illustrate dipole motion characteristics in both quiet and turbulent atmospheres.

## SECTION II

### TEST FACILITIES

#### 1. Enclosed Test Chamber

All instrumented drop tests of chaff dipoles were accomplished in a special aerodynamic test chamber as depicted in Figure 1. The test chamber provides an isolated atmospheric environment (at approximately sea level atmospheric pressure), free of air currents in the surrounding laboratory, and is constructed in such a manner as to enhance the illumination and photographic documentation of single dipoles in free descent.

The primary viewing chamber is approximately a 4-ft cube, which is fully illuminated by twelve 500-W photoflood bulbs in 12-inch aluminized reflectors placed around the periphery as indicated by Figure 1. Contiguous to the primary chamber are three cells for mounting of three fixed motion-recording cameras and two auxiliary chambers, which extend the background viewed by the two horizontally aligned cameras. The background extensions prevent light from being reflected off the chamber surfaces and onto the camera lenses, such that a high contrast is maintained between the illuminated dipoles and the background. To further improve the contrast all of the interior surfaces of the test chamber are painted flat black and the background walls in view of the cameras are draped with black velour. In addition, a series of primary and secondary baffles are provided to further control the background illumination.

The cell directly above the test chamber contains the chaff release mechanisms as well as the downward viewing camera. The overall height of the chamber is 10 ft., thus permitting dipole free-fall of up to six feet prior to entry of the viewing section. The overall length and width of the test chamber is 16 ft. by 16 ft.

The size of the primary viewing chamber was dictated by three considerations. First, the internal volume and dimensions had to be adequate to eliminate wall effects on the chaff aerodynamics. Secondly, the chamber air mass had to be sufficiently small that it would damp out air movements rapidly. Third, the chamber size had to be small enough to allow a very high level of dipole illumination, since light intensity decreases with distance squared.

The 10-ft. maximum drop height is quite ample for investigation of dipole steady-state descent. The approximate distance to reach terminal

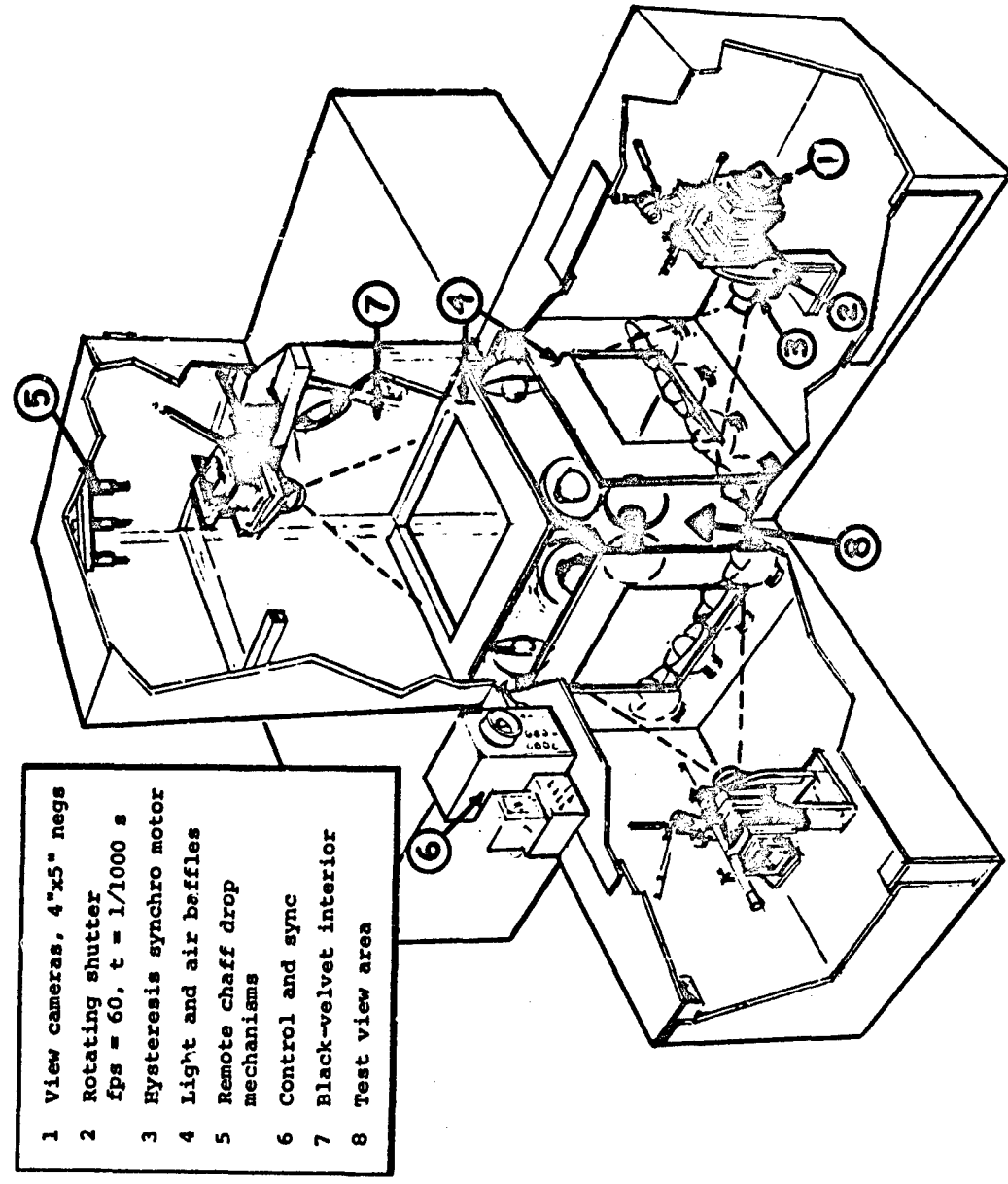


Figure 1. Chaff Aerodynamic Test Chamber

descent velocity when a dipole is released with no initial velocity is

$$s = \frac{V_{ss}}{g} \ln \left[ \frac{1}{2} \left( 1 + e^{-\frac{2gt}{V_{ss}}} \right) \right] - V_{ss} t \quad (1)$$

where  $t = \frac{V_{ss}}{2g} \ln \frac{(1+a)}{(1-a)}$

$V_{ss}$  = steady-state velocity

$t$  = time

$a \approx 0.99$  (i.e., time to achieve  $0.99 V_{ss}$ ).

Using the fastest terminal descent velocity observed in preliminary tests ( $V_{ss} \approx 3$  ft/sec), Equation (1) results in a transient descent distance of 0.55 ft., which occurs in only 0.25 second.

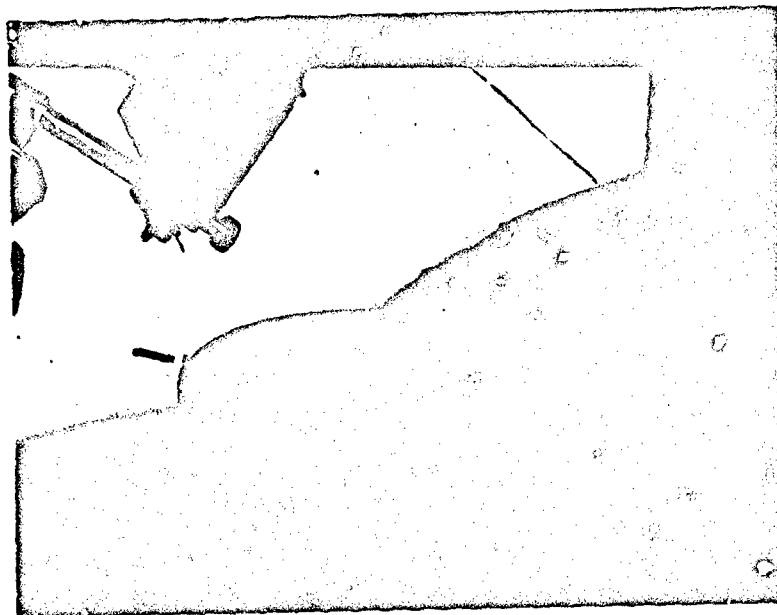
## 2. Instrumentation and Equipment

Cameras Three Calumet 4 in. x 5 in. view cameras with 210 mm f/6.3 Caltar lenses are used to record the dipole motion. The cameras are fixed in position and alignment. Each camera station is provided with an independently-supported special rotating-shutter system to "strobe" the dipole images. The integral shutter in each lens assembly is also retained for initiating and terminating the motion sequences. Both shutters are electrically powered, synchronized, and remotely operable. Figure 2 depicts a camera and rotating shutter installation.

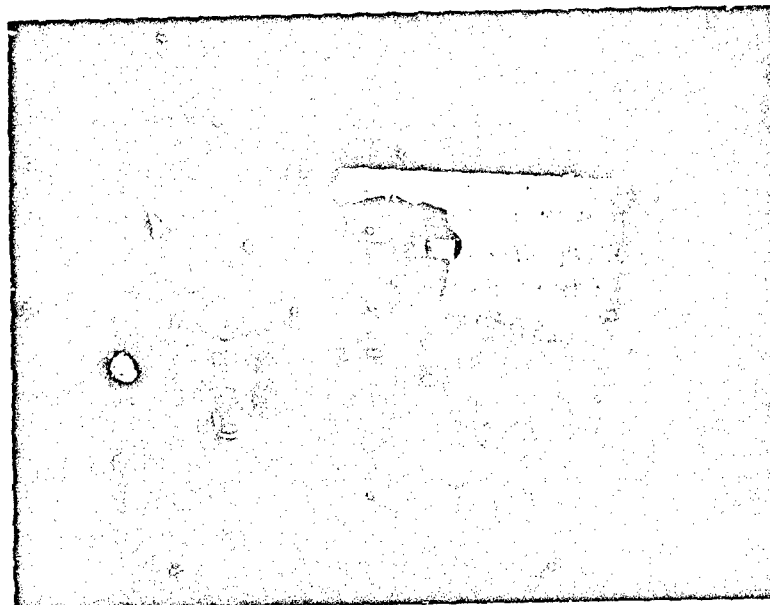
The cameras are positioned and aligned such that the lens axes of cameras 1 and 2 are both horizontal and orthogonal. Camera - 3 is positioned above the viewing chamber and the lens axis is inclined 16.6 degrees from vertical, such that the dipole images during vertical descent are separated. Cameras 1 and 3 constitute a second orthogonal pair.

Rotating Shutter System Each camera station is equipped with a secondary rotating-disk shutter providing intermittent strobing at a rate of 60 images/sec (or optionally, 120 images/sec with two slot openings)

Reproduced from  
best available copy.



b) Rotating disk with single slit aligned with camera view hole



a) View of camera mounted on ceiling; rotating shutter on floor

Figure 2. Camera System and Rotating Shutter

and an exposure duration of 1/1000 second. These shutters were specially designed for the chaff aerodynamic test program.

Each shutter is comprised of a 12-inch diameter, 0.030-inch thick aluminum disk, driven by a 1/50 horsepower 3600 rpm hysteresis synchronous motor. An AC generator is attached to each motor to determine mechanical phase orientation and to facilitate synchronization. The disk and motor assembly are installed in a close fitting housing, which acts as a light baffle and as a means for reducing both the aerodynamic frictional torque on the disk and induced air currents within the test chamber.

Figure 3 shows a schematic of the rotating shutter system. The three rotating shutters are synchronized at the beginning of each testing period by mechanically varying the disk phase position. The phase can be maintained for long periods of time and in normal operation the shutters are aligned each morning and left running continually throughout the day.

Chaff Release Mechanism The device used to hold and release the individual chaff dipoles is depicted in Figure 4. The holder is remotely operable and can be pre-positioned to the desired dipole release orientation.

Pairs of 0.008-inch stainless-steel wires with a tweezer action holds the dipole until a solenoid actuated rod displaces the dipole from the holder. The solenoid has a nominal stroke of 0.1 inch with 0.1 oz. of force at this displacement. An initial velocity (slightly less than the terminal velocity) is usually imparted by the release mechanism; however, the release velocity can be varied by changing the applied voltage to the solenoid.

A holder assembly with a cluster of six identical release mechanisms is shown in the photographs, Figure 5. The complete holder assembly and wiring harness are attached to a strut which spans the test chamber. This strut can be positioned vertically at any desired height within the chamber.

### 3. MCAS Drop Facility

Test drops of chaff clusters (to determine dispersive characteristics at drop heights up to 150 ft.) are accomplished in the Marine Corps Air Station (MCAS) airship hangar at Santa Ana, Calif. This

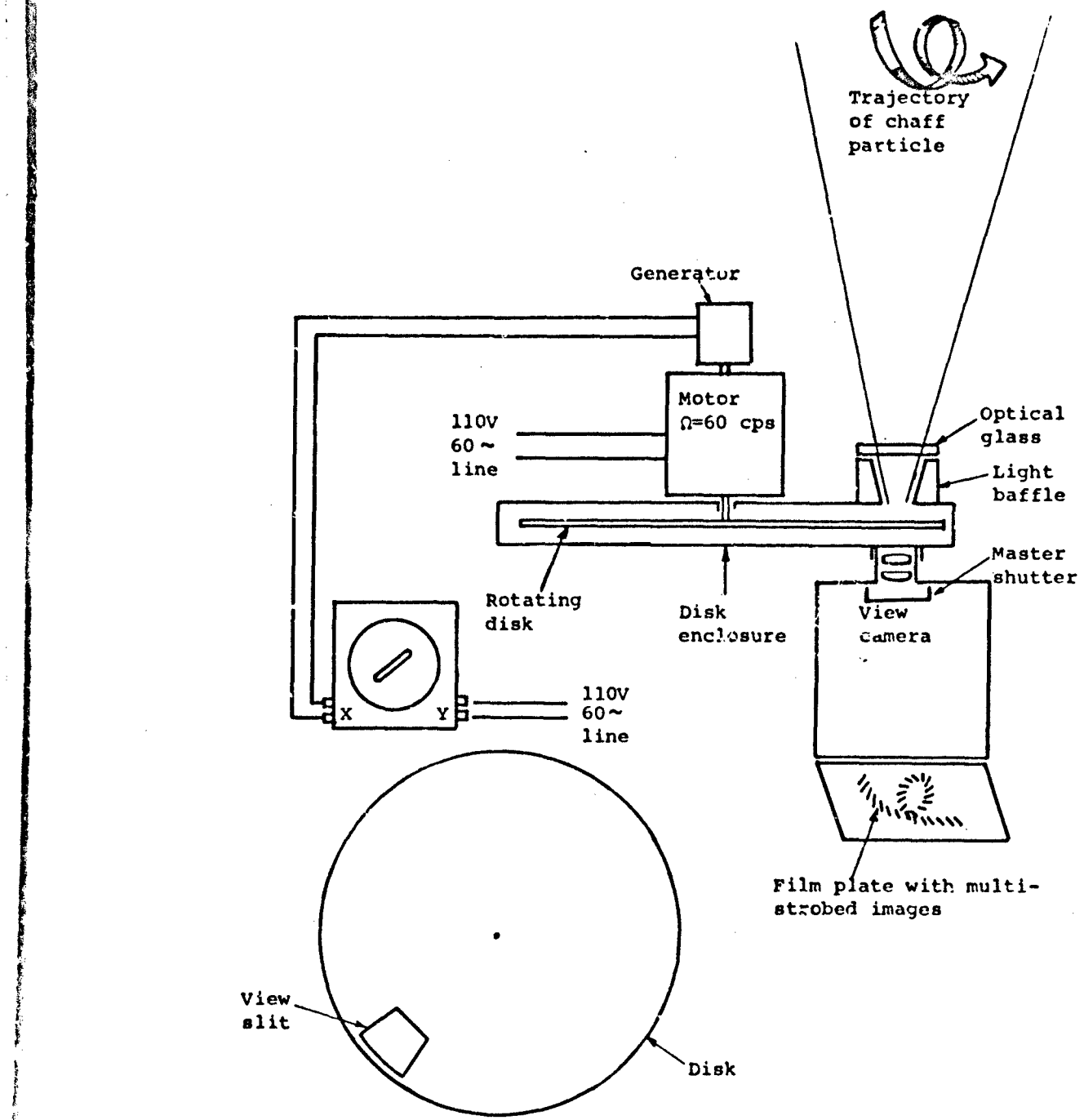
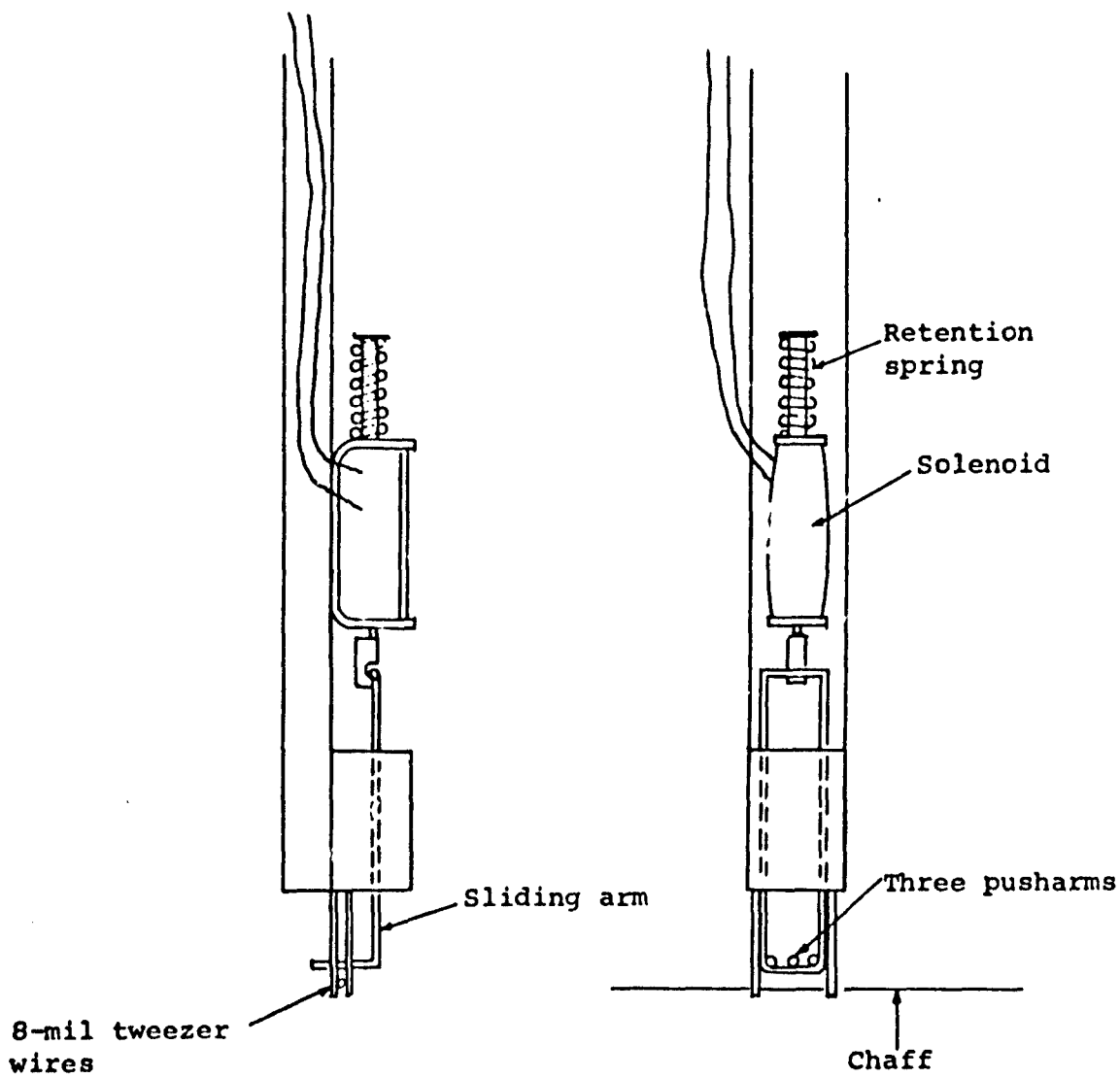


Figure 3. Schematic of Rotating Shutter System

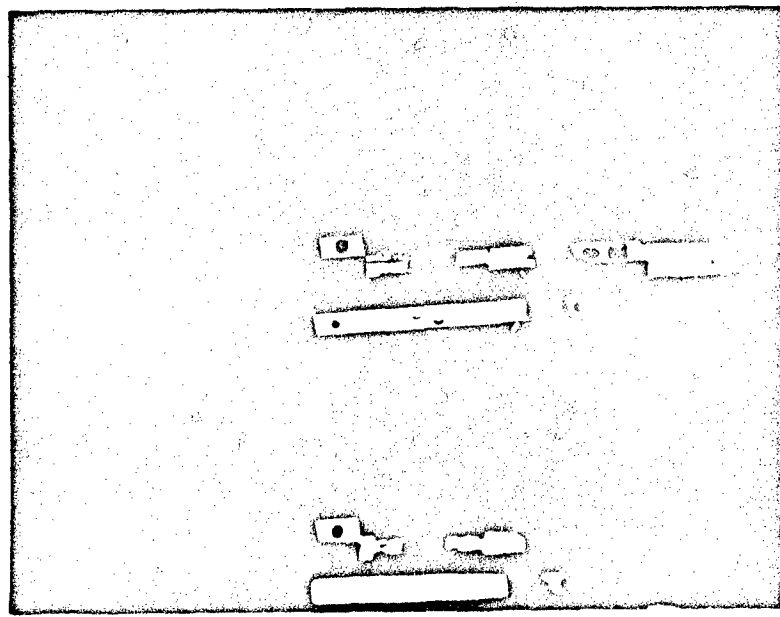
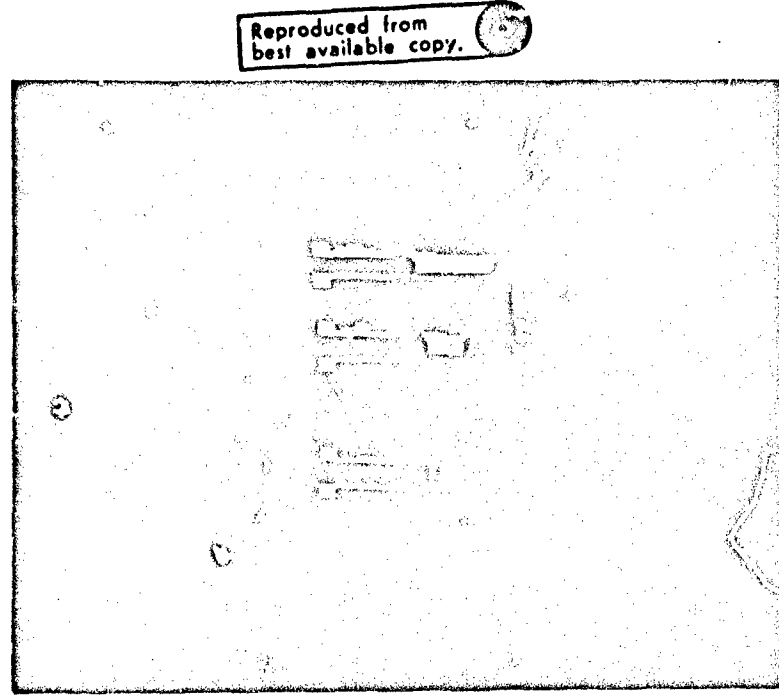


Scale: Illustration is  
twice real size

Figure 4. Filament Holder/Release Mechanism

Figure 5. Chaff Filament Holder Assembly

- a) Single filament in holder  
b) Multiple holder assembly



hangar has a height of 155 ft. and floor space of 300 ft. x 1100 ft. The facility provides a relatively quiescent atmospheric environment during the night when all of the hangar doors and entrances are closed.

Chaff cluster drops are accomplished by use of a trap-door type holder suspended from the hangar ceiling and positioned by a variable length tether. The surface of the trap door is teflon coated to prevent the dipoles from sticking.

### SECTION III

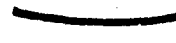
#### TEST ARTICLES

Test dipoles were selected from four basic types of chaff supplied by the Air Force project monitor. Table 1 summarizes the chaff type specifications and designates the dipole sizes selected for the aerodynamic test program. Articles 1 through 11 are those originally selected for the test program, while articles 12 and 13 were included for the purpose of extending the scope of the aerodynamic investigations.

Representative dipoles have been examined in great detail. It was noted that the aluminum coated glass dipoles exhibit considerable surface roughness. Likewise, the edges of the foil chaff exhibit small irregularities. The nominal width (or diameter) of each dipole type was approximately verified by using a microscope in conjunction with an optical comparator.

Several dipole configurations incorporate a longitudinal V-bend for increased stiffness (see Table 1). The V-bend shape varies with chaff type, and is qualitatively described by the following sketch.

Type RR-141/AL



Type RR-149/AL



Type RR-39A/AL



#### V-Bend Configurations

The nominal chaff dimensions are depicted by the following sketch.

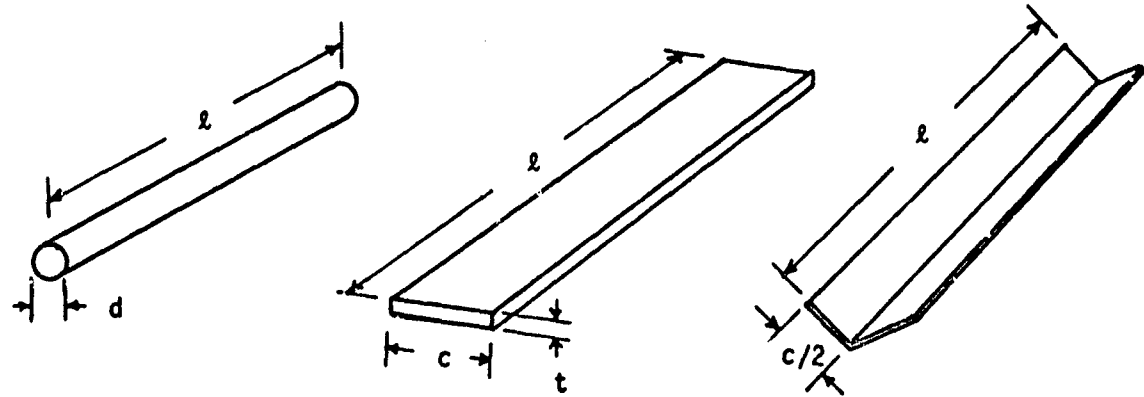


Table 1. DESIGNATION OF CHAFF TYPES

Test Article Designation	Specification/AF Type	Nominal Size	Remarks
1	glass - aluminum	2 mil x 2	special
2	" "	1 mil x 2	Lundy
3	" "	1 mil x 1	Lundy
4	" "	1 mil x 7/16	Lundy
5	RR-141/AL; aluminum foil #1	.008 x .00035 x 2.16	V-bend
6	" "	#6	.008 x .00035 x 1.125
7	" "	#8	.004 x .00035 x 0.6
8	" "	#12	.004 x .00035 x 0.38 no V-bend
9	RR-149/AL; aluminum foil	.006 x .00045 x 1.78	V-bend
10	" "	.006 x .00045 x 1.62	V-bend
11	" "	.006 x .00045 x 0.36	V-bend
12	RR-39A/AL; aluminum foil	.040 x .00045 x 1.12	V-bend; strip coated
13	" "	.040 x .00045 x 0.55	V-bend; strip coated

Note: 1) All items slip coated.  
 2) All dimensions in inches.

in the case of dipoles with V-bend the nominal width corresponds to the equivalent flat strip.

Using the above nominal dimensions, the weight and inertia of each type dipole was computed based on the following material densities.

<u>Material</u>	<u>Density</u>
fiberglass	0.075 lb/in <sup>3</sup>
aluminum foil or coating	0.0975 lb/in <sup>3</sup>
slip coating	0.05 oz/1000 in <sup>2</sup>

The computed dipole weights are summarized in Table 2. To verify the calculated weights, actual average weights for several representative dipole types were determined with a microbalance. Although actual weights varied from sample to sample, relatively good agreement with the calculated weights was achieved for all of the designated chaff types except the 2 mil x 2 inch dipole, which was found to have an actual average weight of only  $3.76 \times 10^{-7}$  lbs, about 60 percent of the nominal calculated value.

Measured weight data were also determined for the RR-39A/AL specification chaff, because these dipoles have an additional lead strip coating which is used to vary the center-of-mass. For example, the weight of the .040 x .00045 x 1.12 dipole varies from about  $2.07 - 2.39 \times 10^{-6}$  lbs. depending upon the amount of strip coating. Average weights for test articles 13 and 14 are  $2.22 \times 10^{-6}$  and  $0.960 \times 10^{-6}$  lbs, respectively.

Table 2. CHAFF DIPOLE WEIGHT AND INERTIA SUMMARY

Test Article Designation	Nominal Size	Total Weight $W \times 10^7$ lbs	$I_x \times 10^{17}$ slug-ft $^2$	$I_y, I_z \times 10^{11}$ slug-ft $^2$
1	2 mil x 2	6.31 (3.76)	6.81 (4.06)	4.54 (2.71)
2	1 mil x 2	1.98	0.534	1.425
3	1 mil x 1	0.99	0.267	0.178
4	1 mil x 7/16	0.43	0.117	0.0149
5	.008 x .00035 x 2.16	7.02	81.0	5.89
6	.008 x .00035 x 1.125	3.66	42.2	0.833
7	.004 x .00035 x 0.6	0.98	2.85	0.0636
8	.004 x .00035 x 0.38	0.62	1.80	0.0161
9	.006 x .00045 x 1.78	5.40	19.0	3.08
10	.006 x .00045 x 1.62	4.92	17.3	2.32
11	.006 x .00045 x .36	1.09	3.85	0.0255
12	.040 x .00045 x 1.12	(22.2)	(6402.0)	(5.02)
13	.040 x .00045 x 0.55	(9.60)	(2763.0)	(0.522)

Note: All weight and inertia data are based on nominal dimensions and densities except where indicated by ( ).

## SECTION IV

### TEST CONDITIONS AND PROCEDURES

The test program utilizing the special test chamber was divided into the following major phases:

- 1) photogrammetric calibration
- 2) development of photographic procedure
- 3) investigation of test chamber turbulence and air currents
- 4) chaff dipole steady-state descent tests
- 5) chaff dipole transient motion tests
- 6) special investigations of chaff dynamics.

A total of 423 tests were accomplished of which 161 were for development and calibration of the photogrammetric system and 262 for documentation of chaff dipole flight.

#### 1. Photogrammetric Calibration

The photogrammetric calibration procedures are described in Appendix A. The final reference system for measurement of dipole position and attitude consisted of a single plumb wire with three bead-type reference marks, each 12 inches apart. The plumb line and beads are clearly visible in the photographs taken from each of the three cameras, but are so located that the dipole motion is never obscured.

#### 2. Development of Photographic Procedure

Special photographic procedures were required in order to obtain distinguishable chaff images on film. At all times there was a compromise between high lens f stops to realize depth of field and lower f stops to improve exposure.

The exposure time of 0.001 sec. (provided by the slot geometry of rotating shutter) was chosen because it results in an image size which can be resolved on film. The relationship between image size and resolution is shown in Figure 7. The various sizes shown in Figure 7 relate to negative film resolution in such a way that one unit corresponds to 100 line parts per millimeter (Lppmm). The nominal filament diameter is shown to be significantly smaller than the resolving capability of the film,

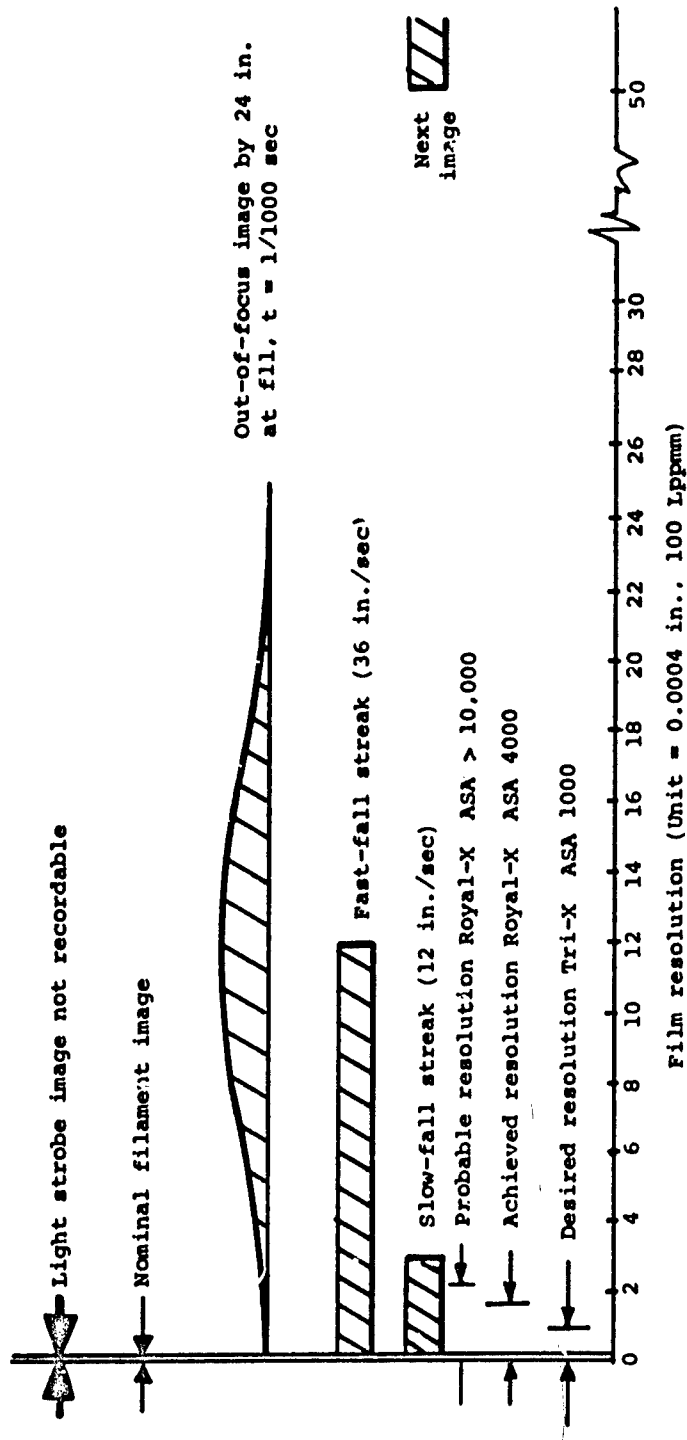


Figure 6. Relationship Between Dipole Image Size and Film Resolution

but with the streaking provided by the rotating shutter the image size is significantly larger than the resolution. Also, the 24-inch out-of-focus image width of approximately 25 resolutions is readable on the negatives and prints because the circle of confusion is 0.01 inches. Thus, with adequate illumination a 48-inch depth of field (corresponding to the test chamber dimensions) is achievable.

The film finally selected for the documentary tests was Kodak Royal-X pan film, Type 4166, in 4 in. x 5 in. Estar sheets. It has a rated ASA index of 4000, which is the highest commercially available speed with standard processing. Further improvement in photographic image quality was achieved by pre-exposing each negative to a density of 0.35 to 0.45 (4-percent opaque) and by extended film development (15 minutes) with Kodak D-19 developer. The pre-exposure was necessary to force the emulsion above its threshold value, and resulted in an effective speed higher by several f stops.

The photographic system was also required to produce up to 180 dipole images per film negative without background over-illumination. This number of images represents three seconds of flight when the rotating shutter is operating at 60 images/second. The directly illuminated dipoles have a probable reflection index of 0.98, therefore, if a factor of 10 difference in background reflectance is necessary to adequately perceive an image, the allowable background reflectance is approximately

$$\frac{0.98}{10 \times 180} = 0.005$$

This low level of reflection was achieved by use of background materials having a reflectance of less than 0.02 and by locating the background cells and baffles such that all visible background light rays were doubly reflected.

Image correlation between the three camera negatives was accomplished in one of four ways.

- 1) dipole initial separation from the holder.
- 2) first image at photoflood turn on
- 3) last image at photoflood turn off
- 4) vertical position correlation.

### 3. Investigation of Test Chamber Air Currents

The large quantity of energy placed into the test cell by the photoflood lamps was found to produce a noticeable convective movement of air. The onset of this convective movement was investigated by injection of a white talc cloud prior to lamp turn-on. Observations of the talc-cloud showed that the air mass in the main 4-ft. cube begins a vertical rise closest to the lights, commencing about 5 seconds after turn-on, and extends into the center of the test chamber after 10 to 15 seconds. Therefore, in the aerodynamic tests, the photoflood lamps are turned on either at the instant of chaff release or at the approximate time of chaff entry into the viewing chamber.

The atmospheric temperature rise during each test was estimated to be about  $0.06^{\circ}$  F, due primarily to water vapor absorption. In addition, a significant increase in wall temperature was observed. To maintain thermal equilibrium and to provide for damping of all convective air currents, a minimum of 10 minutes was allowed between all drop tests.

### 4. Dipole Steady-State Descent Tests

Aerodynamic tests to determine the dipole steady-state descent characteristics were accomplished with the release-holder mechanism positioned from two to four feet above the photographic viewing chamber, thus permitting the dipoles to attain terminal velocity prior to entering the viewing chamber. One dipole (or in some instances two dipoles of widely different length) were released and followed visually until they reached the top of the photographic viewing chamber and at this time the photoflood lights were activated. All steady-state tests were accomplished with the release holder mechanism in the horizontal orientation.

Test Numbers 162 - 270 and 388 - 390 were for the purpose of documenting chaff steady-state flight behavior. These tests were performed using all of the test articles designated in Table 2 (test articles 1 through 13). Each dipole type was dropped several times to insure adequate photographic coverage.

### 5. Dipole Transient Motion Tests

Tests to determine the dipole transient motion were accomplished with the release-holder mechanism positioned at the top of the 4-ft. cube test chamber, in view of all three cameras. The chaff dipole motion was

recorded from the instant of release. Four different orientations of the release mechanism were used to obtain initial chaff dipole attitudes of

- 1) horizontal
- 2) 45-degrees from horizontal
- 3) 60-degrees from horizontal
- 4) vertical.

Test Numbers 271 - 387 were for the purpose of recording the dipole initial transient motion and for determining the effect of the initial release conditions on the steady-state behavior. All of the dipole types (test articles 1 through 13) were utilized for these tests.

#### 6. Special Investigations of Chaff Dynamics

Test Numbers 400 - 404 were accomplished with a wire-mesh disturber grid placed horizontally across the test chamber. The grid spacing was selected such that there would be a high probability of a dipole striking the grid and receiving an angular impulse. The purpose of this test series was to assess the dipole aerodynamic damping moment. These tests were performed with test article No. 1.

Test Numbers 404 - 415 were for the purpose of investigating the effect of longitudinal center of gravity offset on the flight characteristics of a cylindrical dipole. The 2 mil x 2 inch dipoles were used for these tests and were weighted at one end by dipping them in lacquer to a depth of either 5 or 20 diameters.

Test Numbers 416 - 421 were for the purpose of evaluating the effect of geometric and mass asymmetry on the flight behavior of test articles 12 and 13. The dipole asymmetries evaluated included twists, kinks, diagonal end cuts, and various combinations of lead strip coating.

Test Numbers 422 and 423 were cluster drops of test articles 12 and 13 for the purpose of photographically documenting the chaff initial dispersal characteristics.

## SECTION V

### DATA REDUCTION

#### 1. Photographic Data Processing

Approximately 600 4 in. x 5 in. film negatives were processed from drop tests of individual chaff dipoles in the special aerodynamic facility. These negatives were reviewed for image quality and from them 175 larger size 11 in. x 14 in. prints were produced for photogrammetric analysis of dipole position and attitude. In excess of 2400 separate image measurements were taken from these prints and recorded on computer cards. Print reading was accomplished manually with the aid of an optical magnifier. Dipole position was read with a metal scale to an accuracy of approximately .005 inches. Dipole orientation was read by use of a drafting machine head, with an estimated reading accuracy of 0.5 degrees.

Figures 8 and 9 depict typical chaff dipole multi-image photographs for a cylindrical glass-type dipole and an aluminum foil-type dipole, respectively. Figure 10 shows multi-image photographs of a 0.040-inch width foil-type dipole taken from camera positions 1 and 3. Autorotation of the dipole about its longitudinal axis is clearly visible in the latter photographs.

#### 2. Dipole Trajectory and Motion Data

A total of 81 dipole flight trajectories were converted into numerical time-position-attitude histories. This was accomplished using the photogrammetric procedures and data reduction computer program described in Appendix A.

#### 3. Aerodynamic Data Reduction

For each dipole trajectory the following variables were determined from numerical data processing of the time-position-attitude histories:

$$\begin{array}{c} \dot{x} \\ \dot{y} \\ \dot{z} \end{array} \quad \left. \right\} \text{velocity with respect to inertial reference system}$$

Preceding page blank

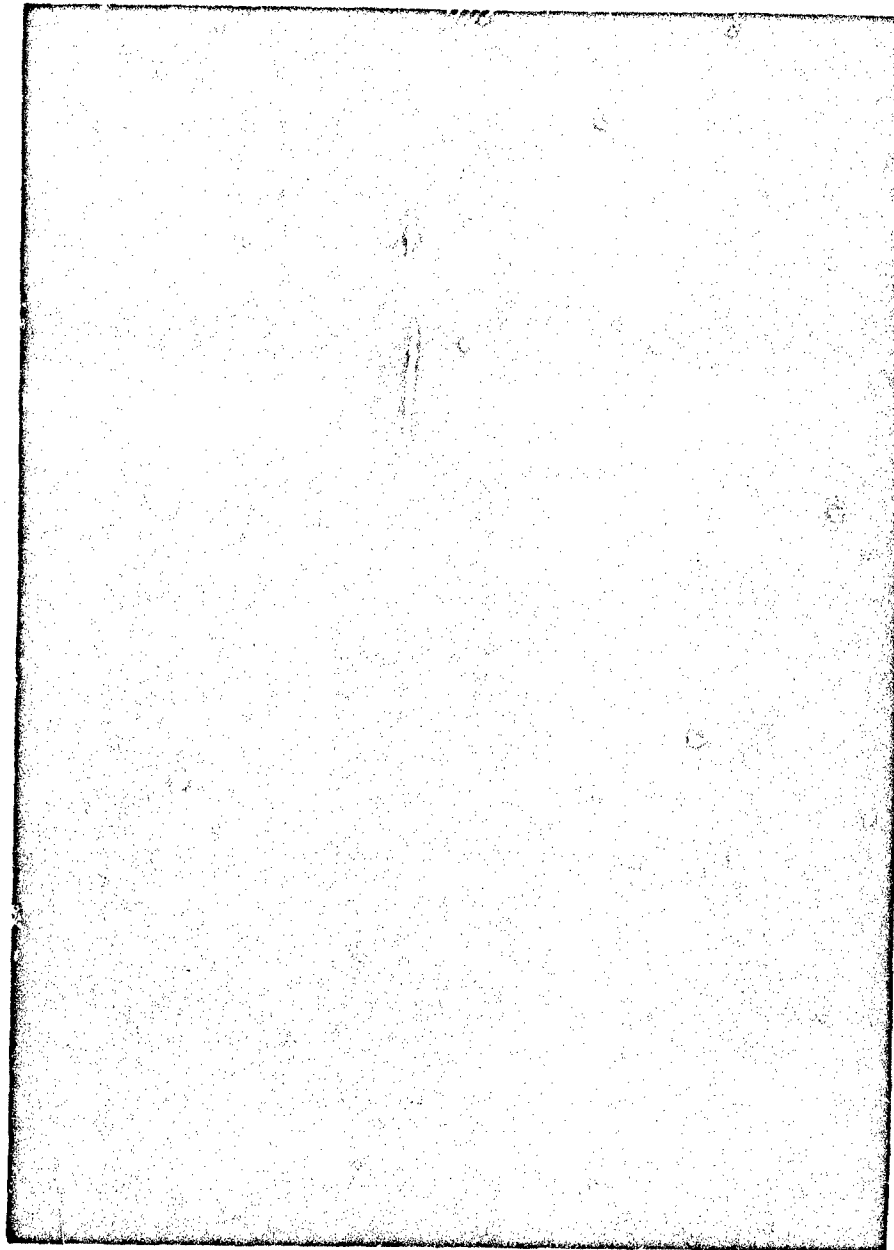


**Figure 7. Multi-Image Photography of 2 mil x 2-inch Dipole**

Reproduced from  
best available copy.

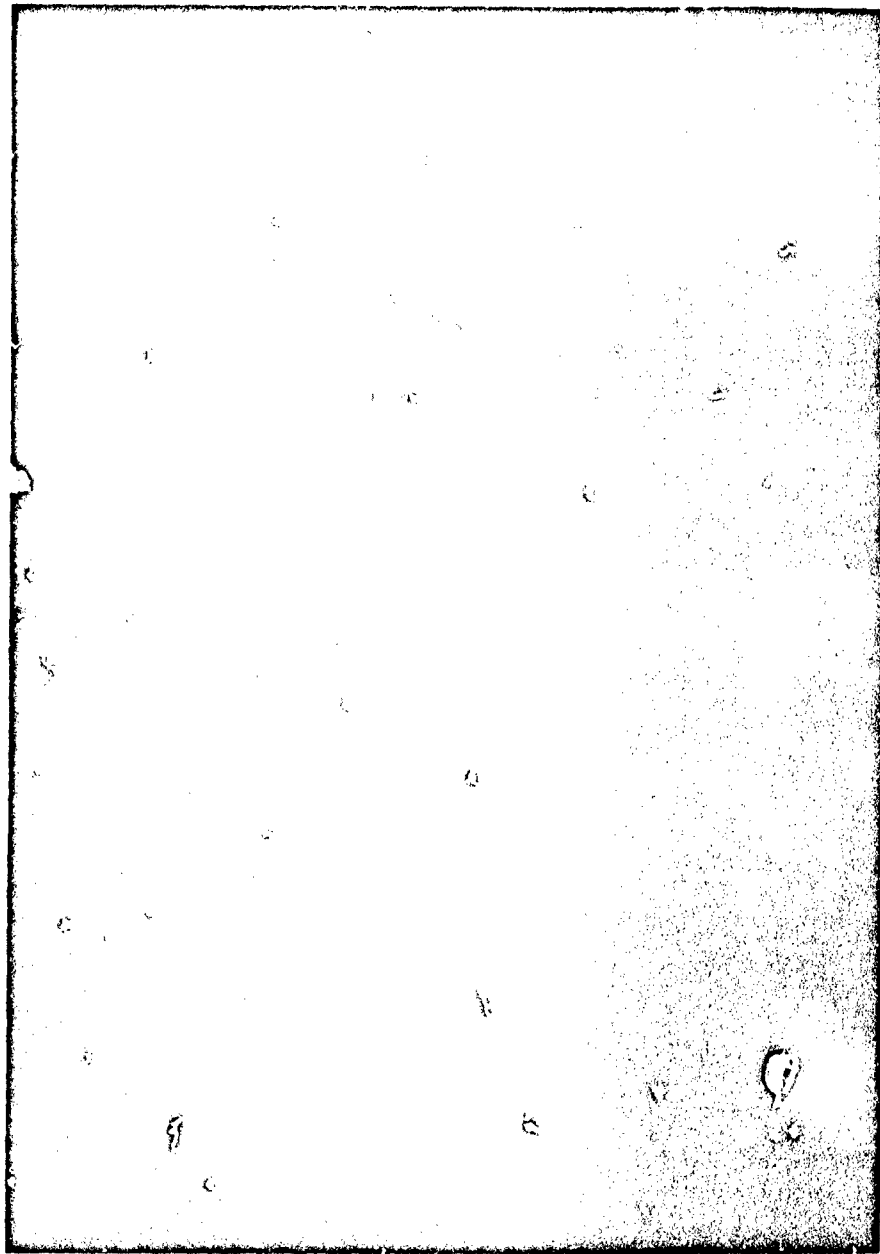
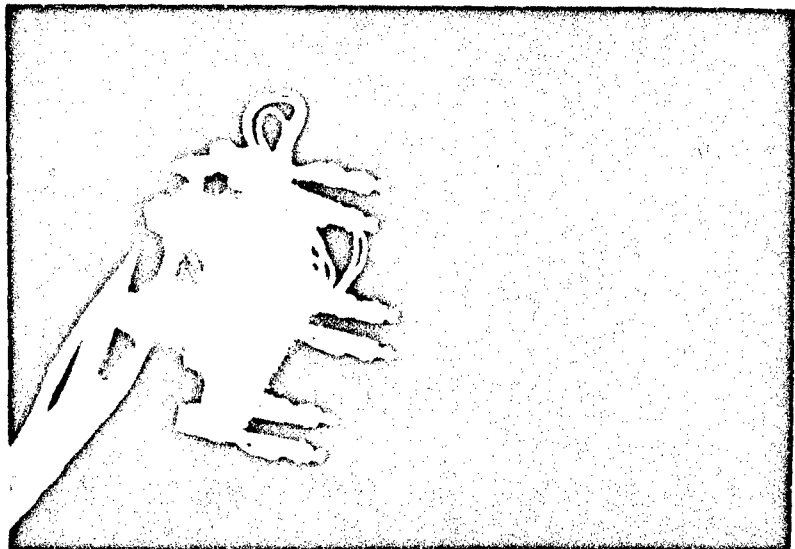
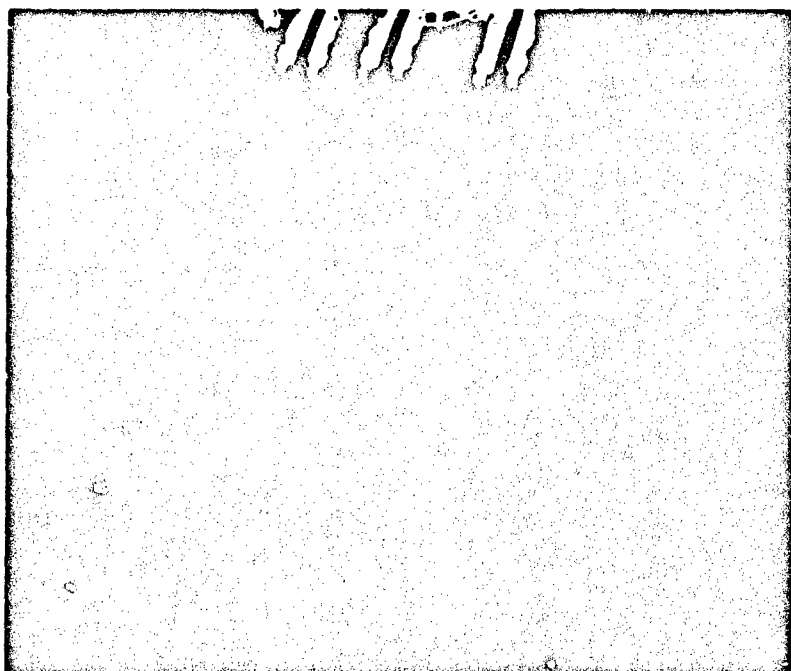


**Figure 8. Multi-Image Photography of  
.006 x .00045 x .36-inch Dipole**



**Camera Position 3**



**Camera Position 1**

**Figure 9. Multi-Image Photography of .040-Inch Width Dipole from Camera Positions 1 and 3**

$p$	dipole angular velocity referenced to dipole moving (fixed-plane) axes
$q$	
$r$	
$\dot{p}$	
$\dot{q}$	dipole angular acceleration
$\dot{r}$	
$C_A$	dipole axial force coefficient
$C_N$	dipole normal force coefficient
$C_{SF}$	dipole side force coefficient
$C_M$	dipole pitching normal coefficient
$C_{SM}$	dipole side moment coefficient
$C_L$	dipole rolling moment coefficient
$\alpha$	total angle of attack
$\xi, \bar{\phi}$	angle of attack plane angular rotation parameters
$\psi$	flight heading angle
$\gamma$	flight path descent angle
$U$	total velocity

Aerodynamic data reduction was accomplished using the relationships described in Appendix B, and a Fortran computer program adapted to a CDC 6600 data processing machine.

All velocities and accelerations were determined by numerical moving polynomial smoothing and differentiation formulas. The number of data points for each fitted arc could be selected by the analyst; either a five or seven point fit was employed in all cases. The aerodynamic coefficients were determined by direct solution of the equations of motion at the midpoint of each fitted arc.

## SECTION VI

### RESULTS

#### 1. A Qualitative View of Chaff Dipole Dynamics

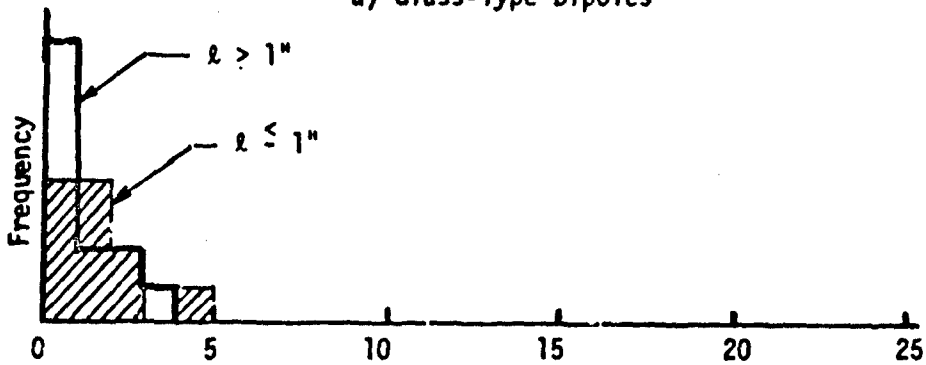
Both the multi-image photographs and the motion parameters computed from the aerodynamic data reduction program (see Section IV-3 and Appendix B) provided a qualitative view of chaff dipole flight dynamics.

The flight characteristics of a chaff dipole were found to be significantly affected by the cross-sectional dimensions of the element.

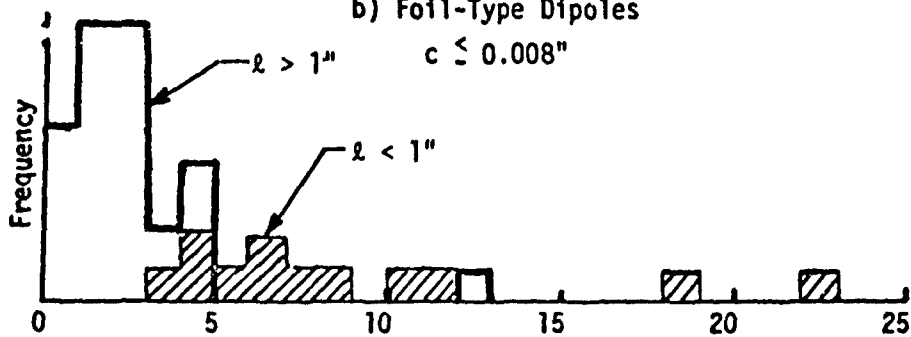
Slender Dipoles Dipoles with a diameter or width of 0.008 inches or less (i. e., test articles 1 through 11) exhibit a single characteristic motion in all cases. This motion can be characterized as a quasi-steady-state spiral, where the spiral angular rate,  $\Omega$ , and the dipole azimuthal angular rate,  $\psi$ , are nearly identical and either constant or slowly varying. The rate of spiral for dipole test configurations 1 through 11 varied from near zero to about 22 rad/sec. The spiral rate is observed to increase with either a decrease in dipole length or an increase in dipole width (or diameter). Figure 11 shows frequency histograms of spiral rate for various dipole classifications.

The spiral is also characterized by the rate of descent and glide angle,  $\gamma$ , as depicted in the following sketch.

a) Glass-Type Dipoles



b) Foil-Type Dipoles



c) Foil-Type Dipoles

$c = 0.040"$

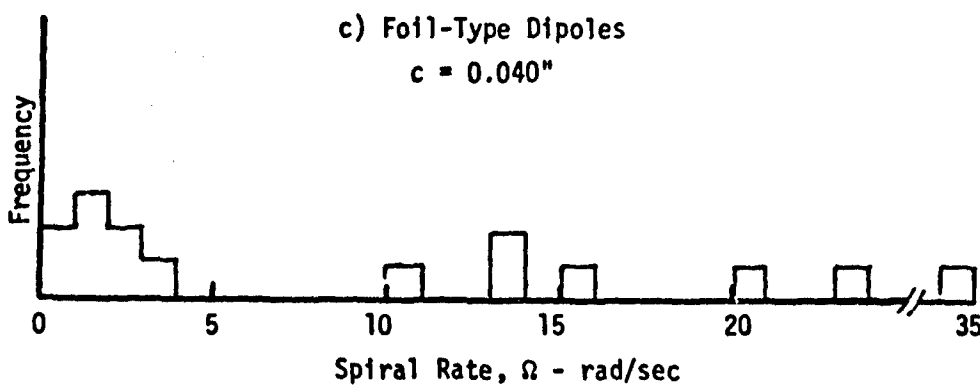
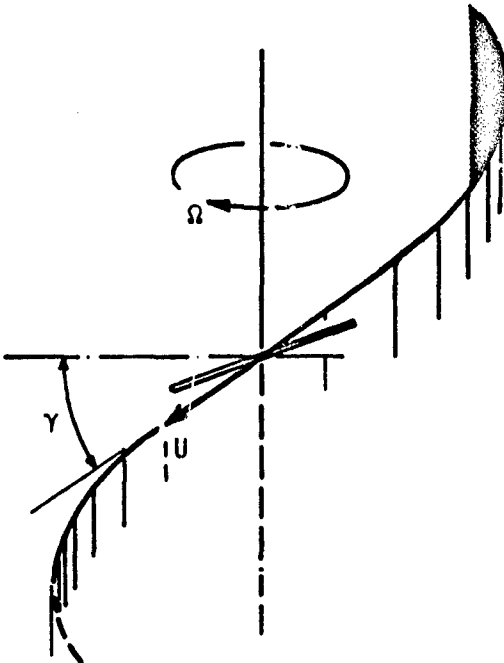
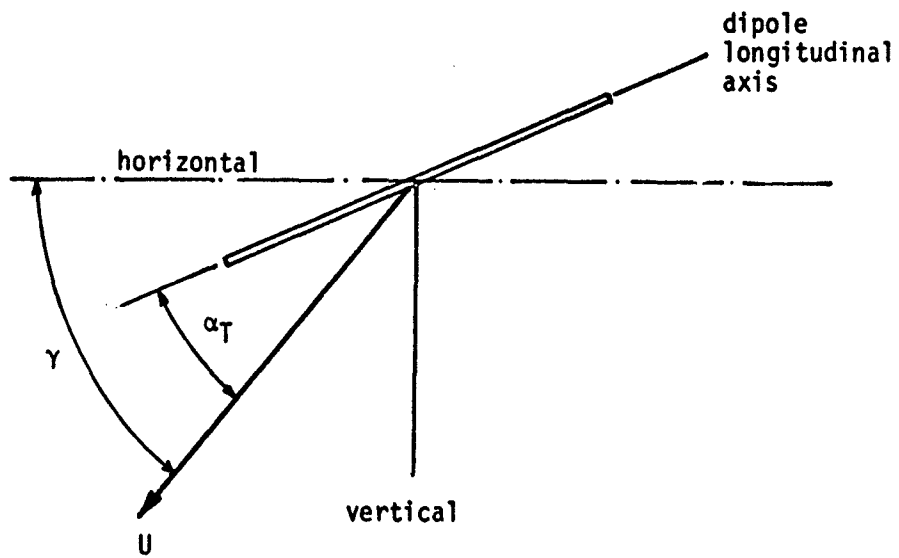


Figure 10. Spiral Rate Statistics



**Characterization of Chaff Dipole Spiral**

The flight path angle is closely related to the trim angle of attack, as defined in the sketch below.



While the trim angle of attack varies from near zero to ninety degrees, the flight path angle has a maximum value of the order of 20 degrees. Both the spiral rate and trim angle of attack are the result of configurational asymmetries, as described and discussed in Appendix C.

The final distinguishing characteristic of the spiral motion (for dipoles with  $c \leq 0.008$  inches) is that the plane constituted by the dipole longitudinal axis and its velocity vector is always close to vertical. Thus if the spiral were to be compared to that of a diving aircraft in a highly banked turn, the orientation of the dipole longitudinal axis would correspond to the aircraft fuselage. In other words, the dipole does not exhibit a "bank angle" per se but has the appearance in flight of a gliding spear (see Figure 8).

Wide Dipoles Dipoles with a width,  $c$ , of 0.040 inches (test articles 12 and 13) are dynamically more active than the slender dipoles. This is apparently due to the presence of a different flow regime, (associated with the larger cross-flow Reynolds number) wherein vortices can be shed from the edges of the dipole. (A detailed discussion of this phenomenon is presented in Appendix C). In addition to the spiral, the wide dipoles can exhibit independently three types of autorotative motion: 1) a large angle of attack magnus-rotor-type motion with autorotation about the dipole longitudinal axis, 2) a flat spin (or coning motion) with autorotation about a transverse axis, and 3) a projectile-like motion with spin about the longitudinal axis. The first of these three autorotative motions is shown in Figure 10, while motions 2) and 3) are depicted in the photographs of Figure 12, following.

The autorotation rates of those dipoles which experienced magnus rotor type motions were determined by a graphical motion fitting process. In all cases the angular velocity was found to be in the range of 40 - 60 radians per second. These rates correspond to values of the nondimensional frequency parameter  $wc/2V$  between 0.03 and 0.04.

## 2. Quantitative Analysis of Dipole Dynamics

Figures 13 - 15 present typical trajectory and motion history data as determined from the aerodynamic data reduction program. Plots such as these were prepared for each of the 81 dipole trajectories which were processed.

Figure 13 illustrates the horizontal projection (X-Y coordinates) of a typical spiral. Figures 14 and 15 show the time histories of the motion parameters and also the variation of the aerodynamic force and

Reproduced from  
best available copy.

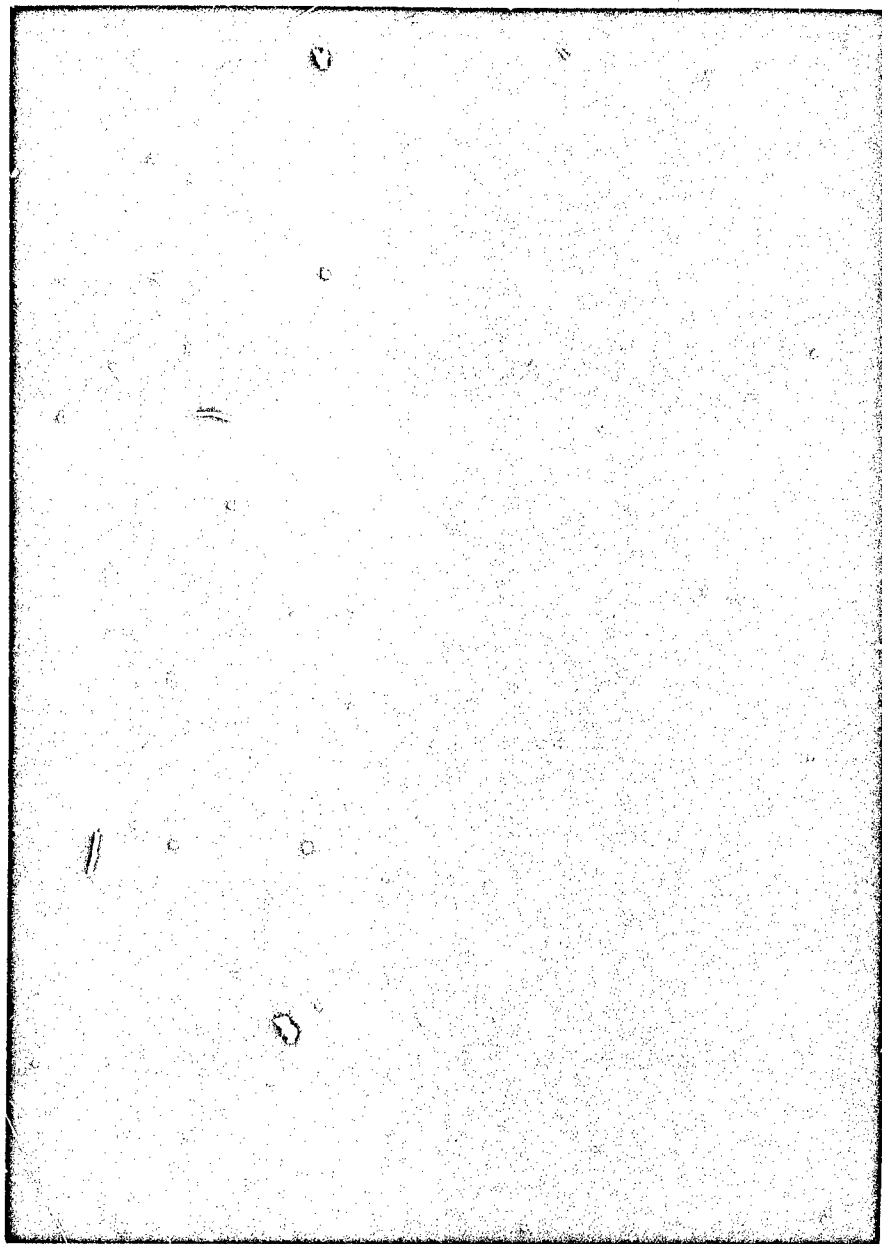


**Figure 11. Multi-Image Photography of .040-Inch Width Dipoles in Autorotative Motion**

data for test article No. 5  
(flight No. 315)

$t = 0.02 \text{ sec}$

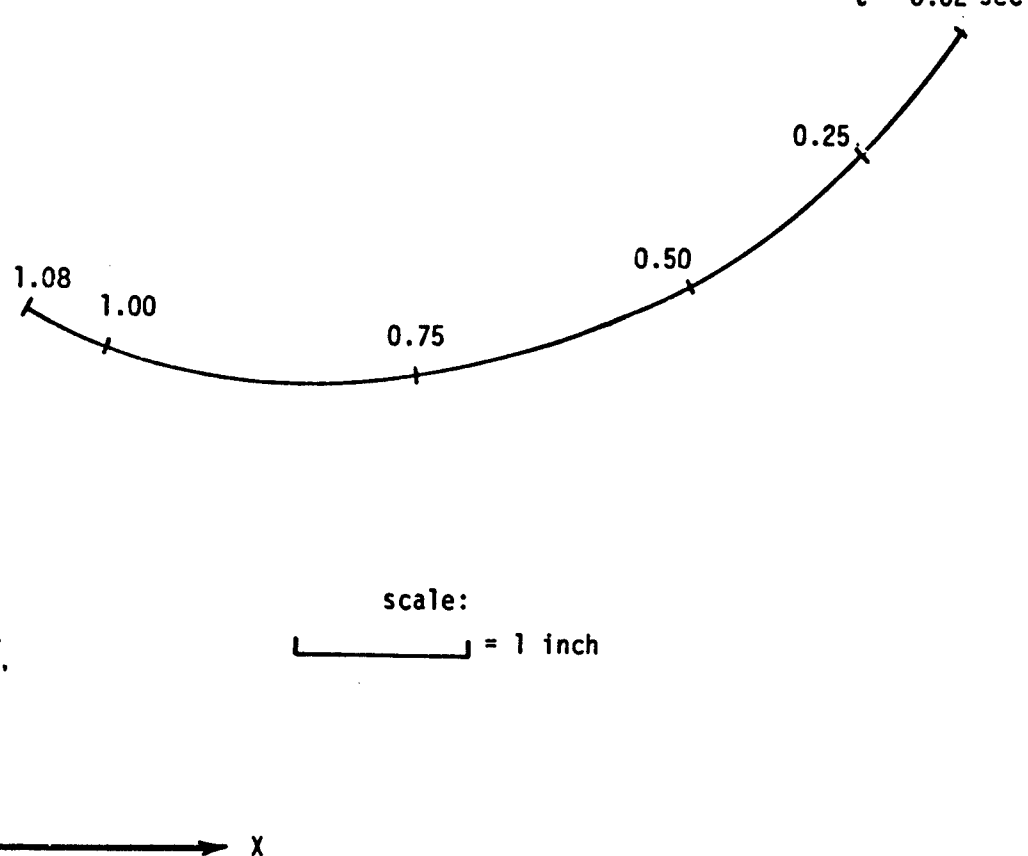


Figure 12. Vertical View of Typical Dipole Trajectory

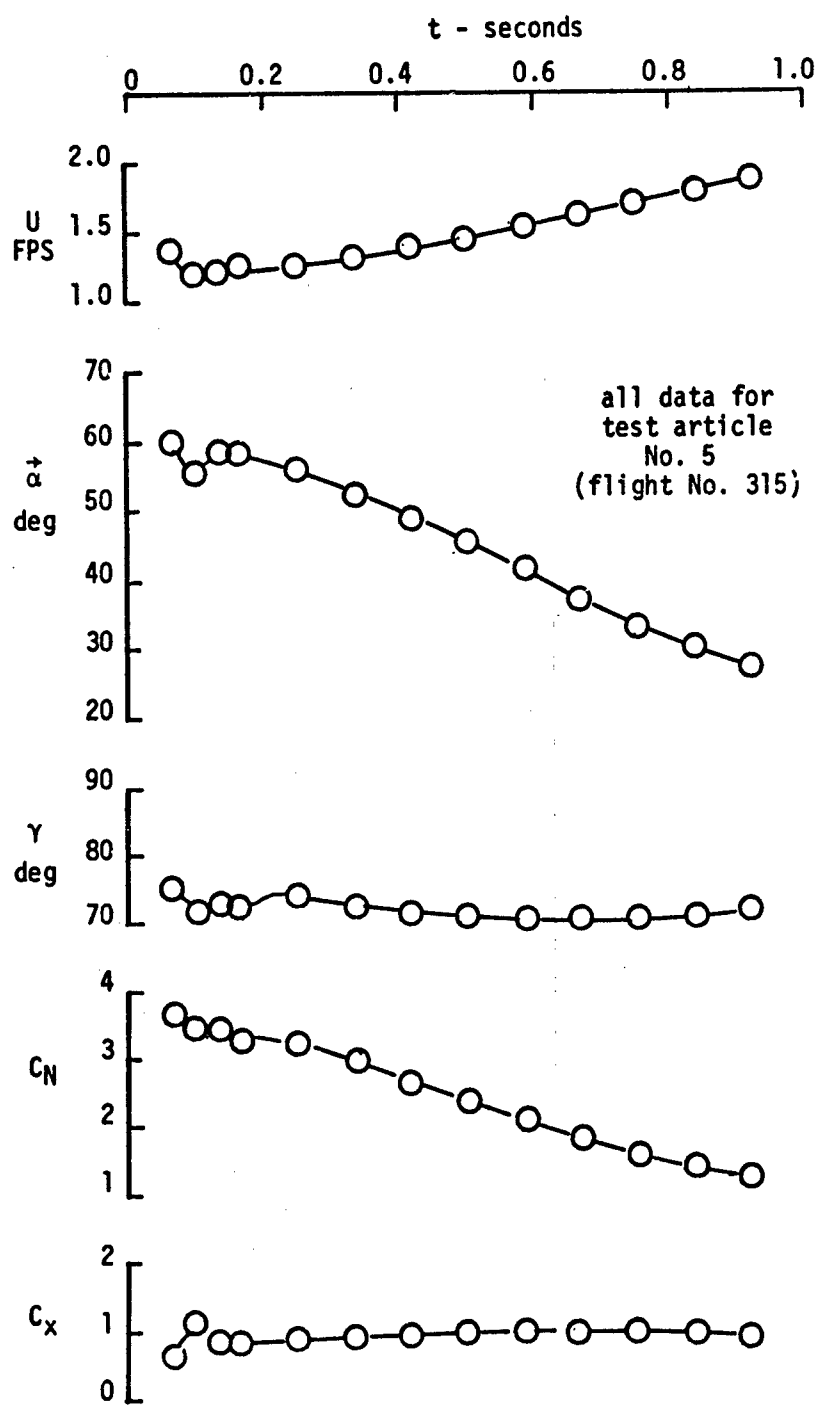


Figure 13. Time Histories of Motion Parameters and Aerodynamic Normal Force and Axial Force Coefficients for a Typical Dipole

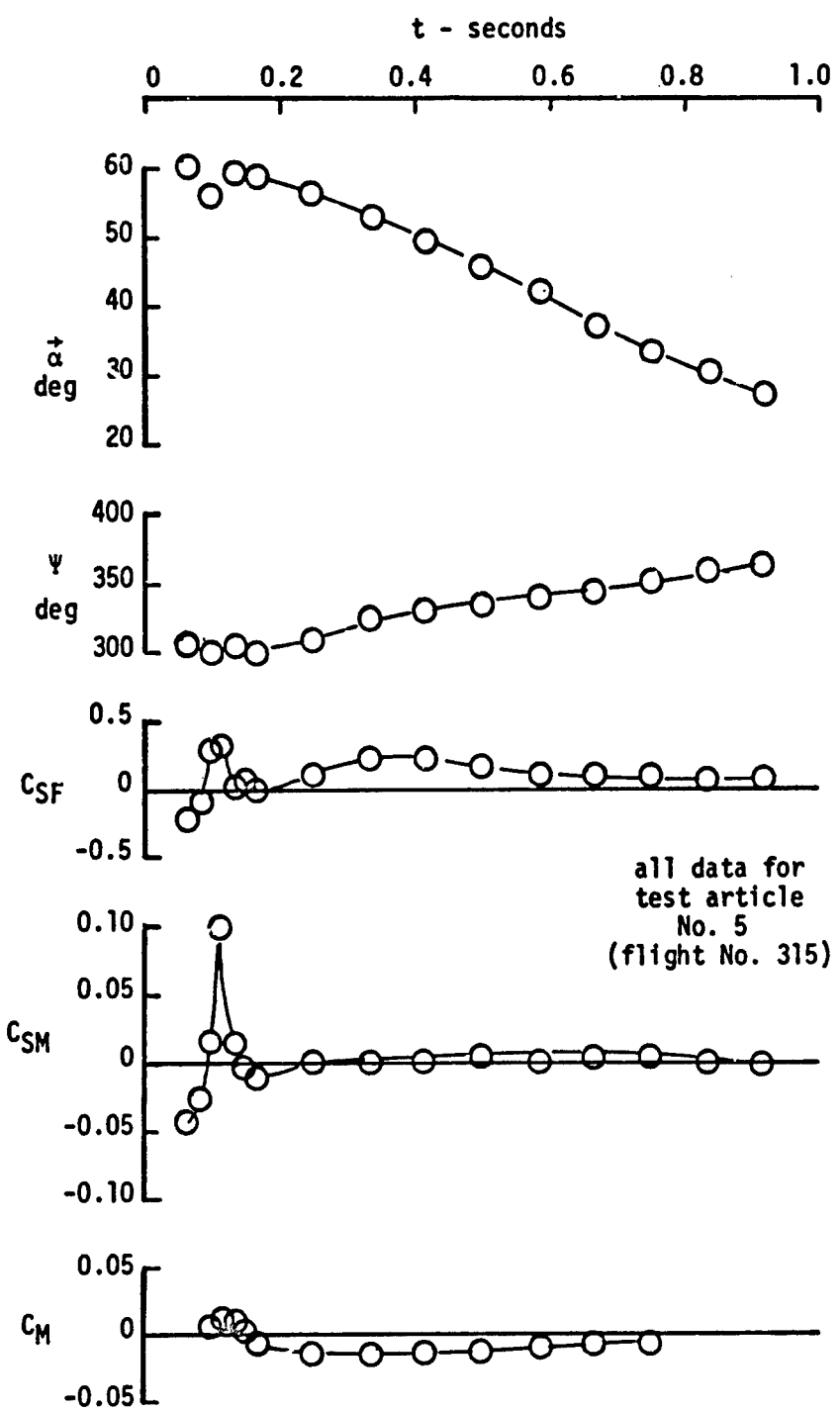


Figure 14. Time Histories of Motion Parameters, Aerodynamic Side Force Coefficient, and Aerodynamic Moment Coefficients for a Typical Dipole

moment coefficients. Zero time represents the initial image used in the data reduction and is not the time of release. In this example the motion parameters are slowly varying, but the motion does not represent the initial transient because the total velocity,  $U_T$ , is quasi-steady at the beginning of the motion record. The correlation between the motion parameters and also between the motion parameters and the aerodynamic force coefficients is seen to be very good. For example, as the angle-of-attack decreases there is a corresponding increase in the velocity and a reduction in the normal force.

While the data for most dipole descents displayed only a small change in the motion parameters, the data which have been used for illustration show that a single test can provide usable conditions over a range of values of the motion parameters.

Correlation of Descent Angle and Angle of Attack One of the most significant motion parameter correlations is that between the dipole total angle of attack,  $\hat{\alpha}$ , and the glide angle,  $\gamma$ . The results are shown in Figure 16, and include data from each of the 81 dipole flights which were analyzed. The experimental results are compared with the theoretical solution for the descent path of a needle-like body in creeping flow (Equation (C-10) of Appendix C). It is seen that the experimental data closely agree with the theory both in magnitude and trend. The only exception is where magnus-rotor-type motions were observed. Particularly good agreement is noted between the theory and the experimental results for the cylindrical glass-type dipoles, both of which show a maximum glide angle of 70 degrees from horizontal at an angle of attack of 35 degrees.

More shallow glide angles (i. e., greater deflections from vertical) occur with the foil-type dipoles, because these have a larger lifting force due to their greater projected surface area, but at most the glide capability of the foil-type dipole is only 50 percent greater than that of the cylindrical dipole.

The above results show that the dispersion characteristics of chaff dipoles are essentially independent of the dipole length and depend only to a moderate extent upon the dipole cross section.

### 3. Aerodynamic Coefficient Correlations

The chaff aerodynamic force and moment coefficients are defined in Figure 17. The coefficients are related to a right hand xyz body-fixed non-rolling coordinate system which has its origin at the dipole

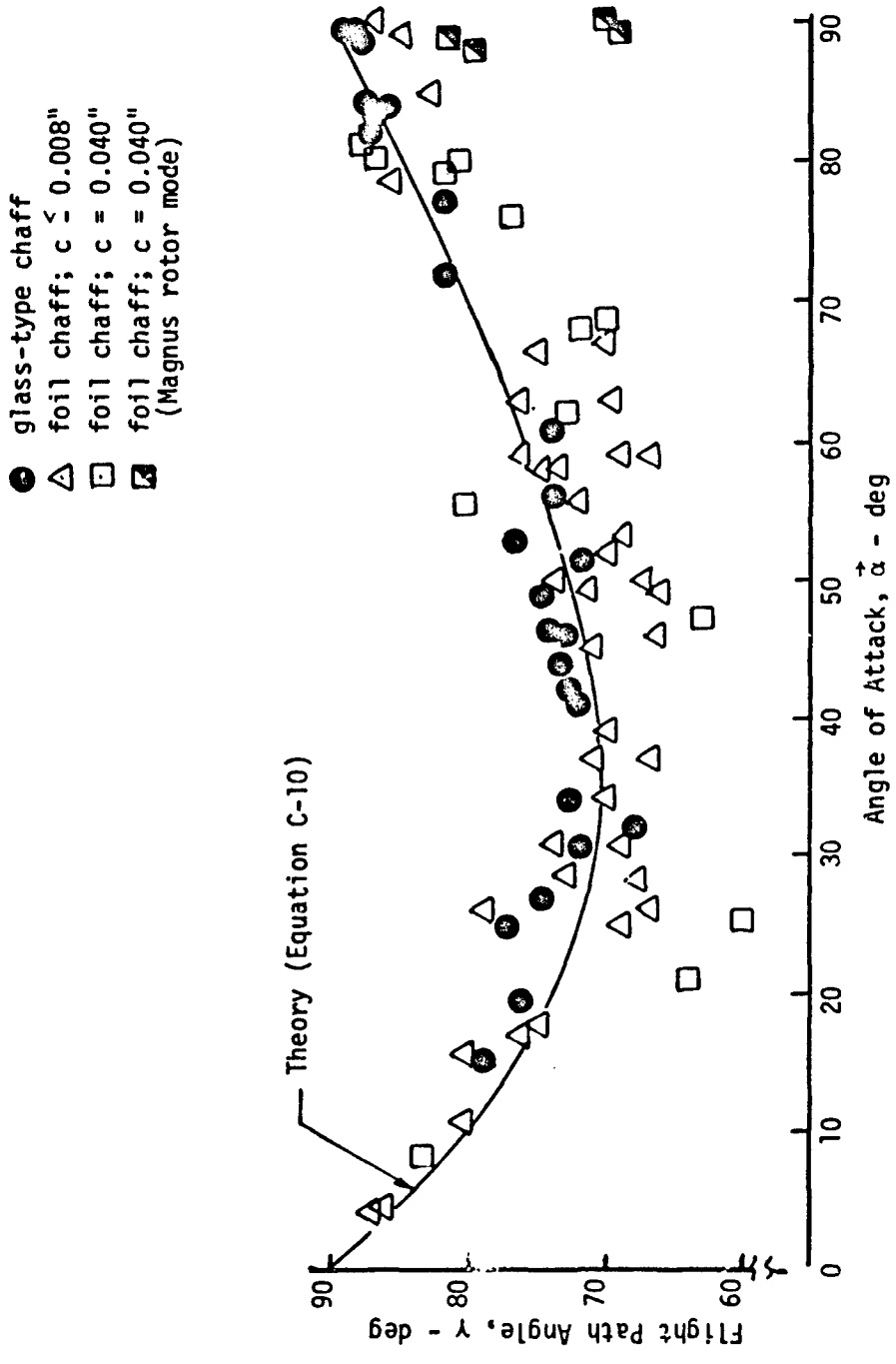
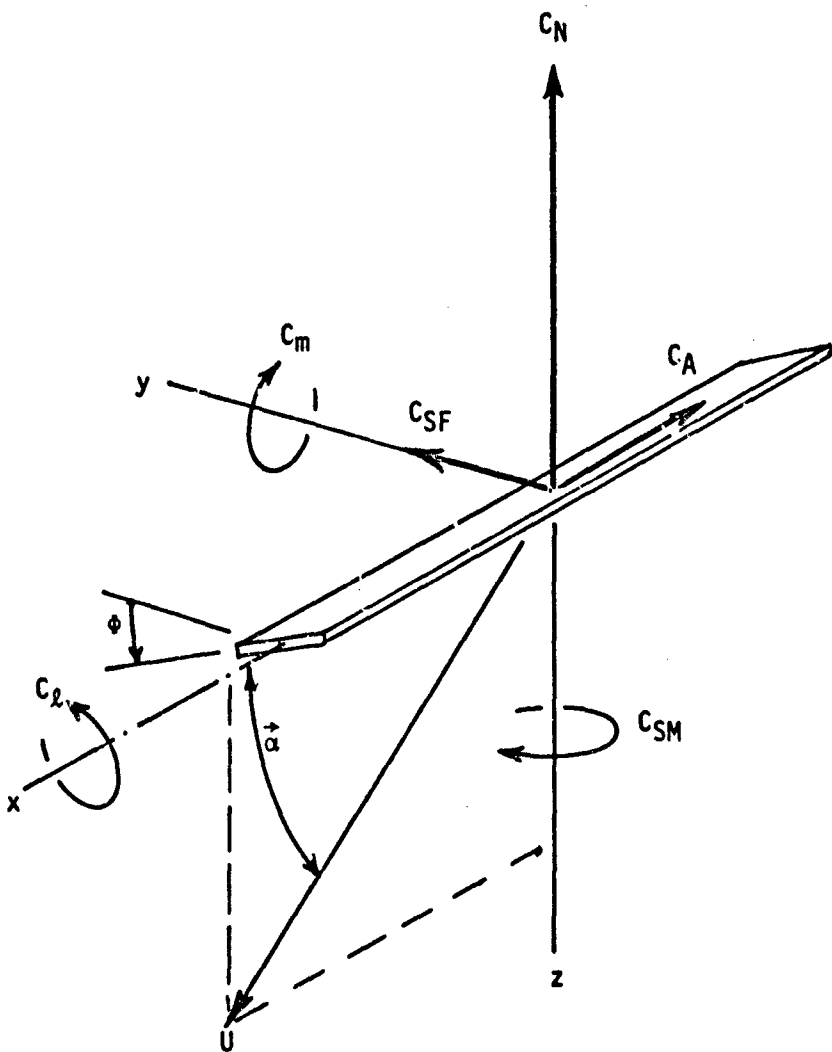


Figure 15. Correlation of Descent Angle,  $\gamma$ , with Angle of Attack,  $\hat{\alpha}$



**cylindrical dipole**

aerodynamic reference area =  $\ell \times d$   
 aerodynamic reference length =  $\ell$

**foil dipole**

aerodynamic reference area =  $\ell \times c$   
 aerodynamic reference length =  $\ell$

Figure 16. Aerodynamic Force and Moment Coefficient Definitions

centroid and where the  $x$  axis coincides with the dipole longitudinal axis, the  $z$  axis is oriented such that  $xz$  plane always contains the total aerodynamic velocity vector, and the  $y$  axis completes the triad. The normal force coefficient,  $C_N$ , is perpendicular to the dipole axis and always in the angle of attack plane, while the side force coefficient,  $C_{SF}$ , is always perpendicular to the angle of attack plane. Similarly, the overturning (or pitching) moment coefficient,  $C_M$ , corresponds to a rotation in the angle of attack plane, while the side moment coefficient,  $C_{SM}$ , relates to rotations perpendicular to the angle of attack plane. The dependence of the aerodynamic coefficients on the dipole angular orientation about its longitudinal axis, which is denoted by the angle,  $\Phi$ , is not considered directly in the aerodynamic data reduction, because this angle cannot be determined from the photographic images. However, the effect of  $\Phi$  is determined indirectly by the magnitude of  $C_{SF}$ , since this coefficient is zero for  $\Phi = 0$ , and should have a nearly linear dependence on  $\Phi$  for  $\Phi < 20$  degrees. The theoretical effect of  $\Phi$  on the aerodynamic coefficient is discussed in Appendix C, and is shown to be diminishingly small as the dipole width decreases.

Drag Coefficient The relationship between the drag coefficient and the previously defined normal and axial force coefficients is:

$$C_D = C_A \cos \vec{\alpha} + C_N \sin \vec{\alpha} \quad (2)$$

Therefore, for large angles of attack (dipole approximately perpendicular to the direction of flight)

$$C_D \approx C_N ; \quad \vec{\alpha} \rightarrow 90 \text{ degrees} \quad (3)$$

Values of  $C_N$  corresponding to  $\vec{\alpha} \geq 80$  degrees are plotted in Figure 18 as a function of a nondimensional Reynolds number parameter

$$R_N = \frac{\rho C U}{\mu} \quad (4)$$

where

$\rho$  = air density

$\mu$  = viscosity

$U$  = velocity

$c$  = characteristic dipole width  
( $d$  if cylinder;  $c$  if strip)

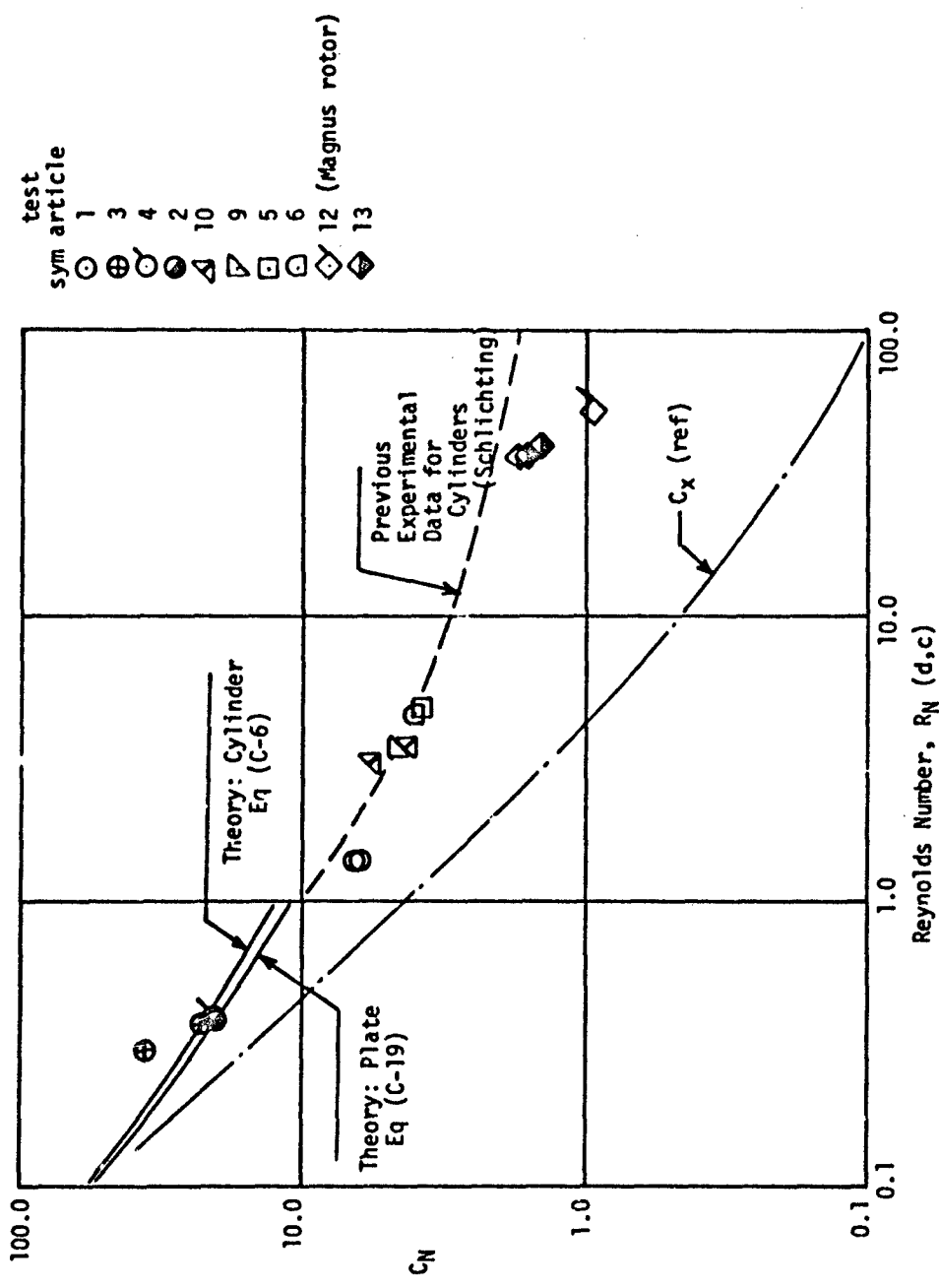


**Figure 17.** Correlation of Normal Force Coefficient with Reynolds Number for Large Angle of Attack Motion ( $\alpha > 80$  deg)

Inspection of Figure 18 shows that  $C_N$  correlates extremely well with  $R_N$  for the complete range of test Reynolds numbers, extending from  $R_N \approx 0.3$  to  $R_N \approx 50$ . The drag coefficient increases rapidly with decreasing Reynolds number, and for the 1-mil glass chaff a maximum drag coefficient of 36 is indicated. The Reynolds number correlation is essentially independent of both the dipole length and cross-sectional shape.

For comparison, theoretical low-speed drag coefficients for a cylinder and plate, based on Oseens approximations (Equations (C-6) and (C-19) of Appendix C) are also shown in Figure 18, along with a previous correlation of experimental drag coefficients for cylinders. Unfortunately no experimental data for flat plates could be located in the literature. The agreement between the dipole data and these data are quite good. The only exception is where the dipole is indicated to be in autorotation.

At small angles of attack, where the dipole longitudinal axis is approximately aligned with the flow, the drag coefficient and axial force coefficients are approximately equal.

$$C_D \approx C_A ; \vec{\alpha} \rightarrow 0 \quad (5)$$

Values of  $C_A$  corresponding to  $\vec{\alpha} \leq 30$  degrees are correlated with Reynolds number in Figure 19. For this correlation the characteristic length for foil-type dipoles is assumed to be

$$d_{eq} = \frac{2c}{\pi} \quad (6)$$

Again dipole length and width have practically no affect on the correlation. For comparison, the axial drag coefficient was computed from the theory of Glauert and Lighthill, as described in Appendix C. These results, which are also shown in Figure 19, are in good agreement with the dipole drag data.

The present dipole aerodynamic data apparently represent the first experimental drag measurements for a slender body in axial flow at very low Reynolds numbers.

As a means of comparing the drag coefficients for axial and normal type flow, the approximate fit to the experimental data in Figure 19 is re-plotted in Figure 18. It is informative that as the Reynolds number decreases the drag coefficient is less sensitive to the dipole

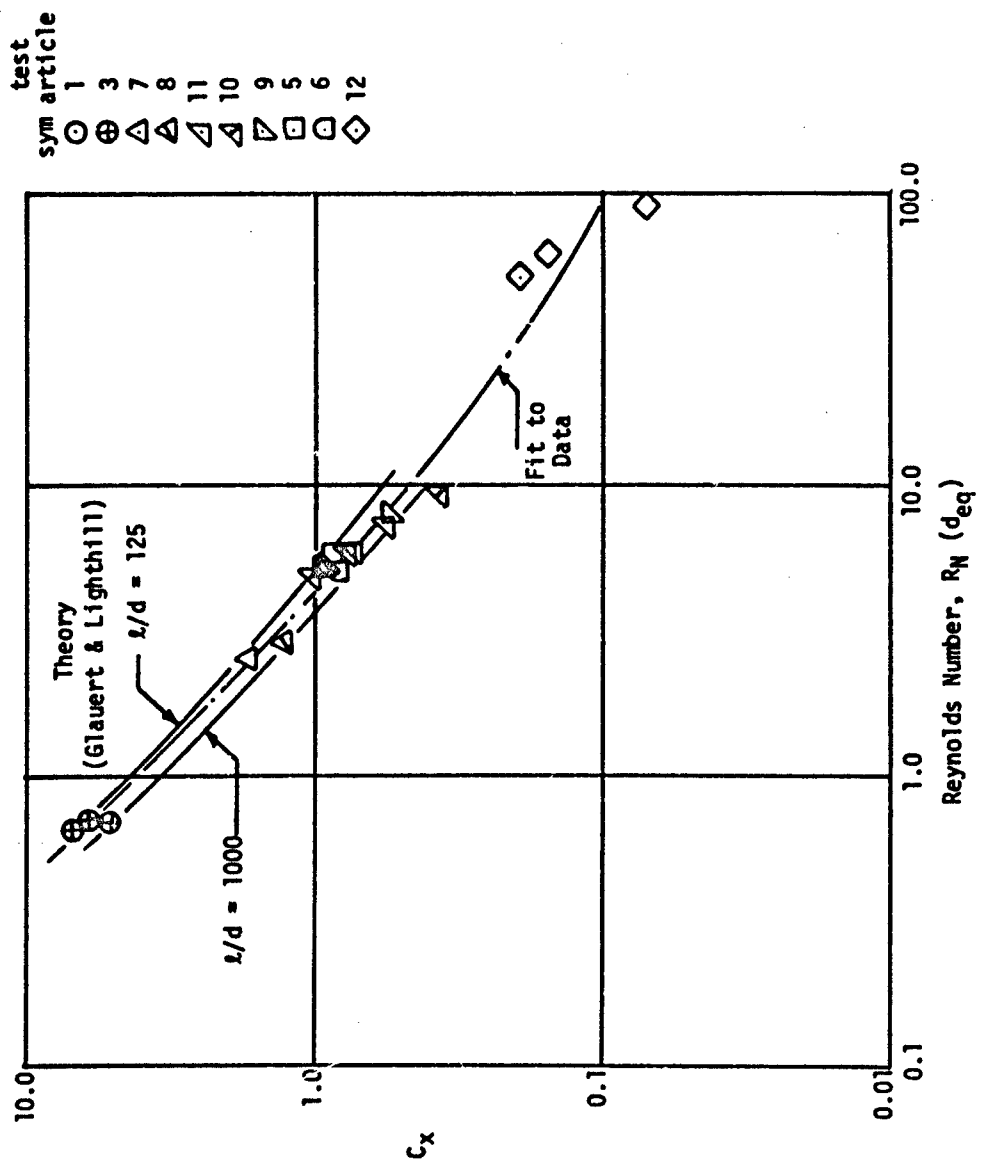


Figure 18. Correlation of Axial Force Coefficient with Reynolds Number for Small Angle of Attack Motions ( $\alpha < 30^\circ$ )

orientation and at  $R_N \approx 0.1$  the drag coefficients for axial and normal flow are nearly equal. On the other hand, at  $R_N \approx 100$ , the drag coefficients for axial and normal flow differ by more than an order of magnitude.

Normal Force Coefficient at a Function of  $\vec{\alpha}$  The correlation of the normal force and axial force coefficients with angle of attack is more difficult, because of the very large influence of Reynolds number. For example, two dipoles of identical configuration at the same angle of attack can be expected to have different values of  $C_N$  if their Reynolds numbers differ. To circumvent this problem use is made of the results from Stokes flow theory that the aerodynamic forces are approximately proportional to  $U$  instead of  $U^2$ . Thus, we might expect for a given value of  $\alpha$

$$C_N \frac{1}{2} \rho U^2 S \propto \text{const} \cdot U \quad (7)$$

or  $C_N \cdot U = \text{constant}$

This is equivalent to saying that the normal force coefficient correlates as the inverse of the Reynolds number. If the values of  $C_N \cdot U$  for each dipole cross-section configuration are correlated separately with angle of attack, the corresponding variation in cross-flow Reynolds number for each dipole is small and the possible error due to the Stokes approximation is also small.

Figures 20 and 21 show the  $C_N \cdot U$  vs  $\alpha$  correlations for the cylindrical glass-type dipoles and foil-type dipoles, respectively. A surprisingly good correlation of  $C_N \cdot U$  with  $\alpha$  is achieved for each characteristic dipole diameter or width, and the correlations are again independent of the dipole length. Two separate correlations are used for the 0.040-inch width dipoles, corresponding to whether autorotation about the longitudinal axis existed or did not exist. Through each set of  $C_N \cdot U$  values a curve proportional to  $\sin \alpha$  has been drawn and this relationship is seen to provide a good fit.

The correlation of  $C_N \cdot U$  with  $\sin \alpha$  constitutes a validation of cross-flow theory for slender dipoles, since this is precisely the result which is obtained when the cross force is equated to the cross flow Reynolds number  $\frac{\rho d U \sin \alpha}{\mu}$  and the local normal force coefficient is assumed to be inversely proportional to the cross flow Reynolds number.

Axial and Side Force Coefficients Following the previous approach, a unique correlation of  $C_A \cdot U$  with  $\alpha$  was also sought.

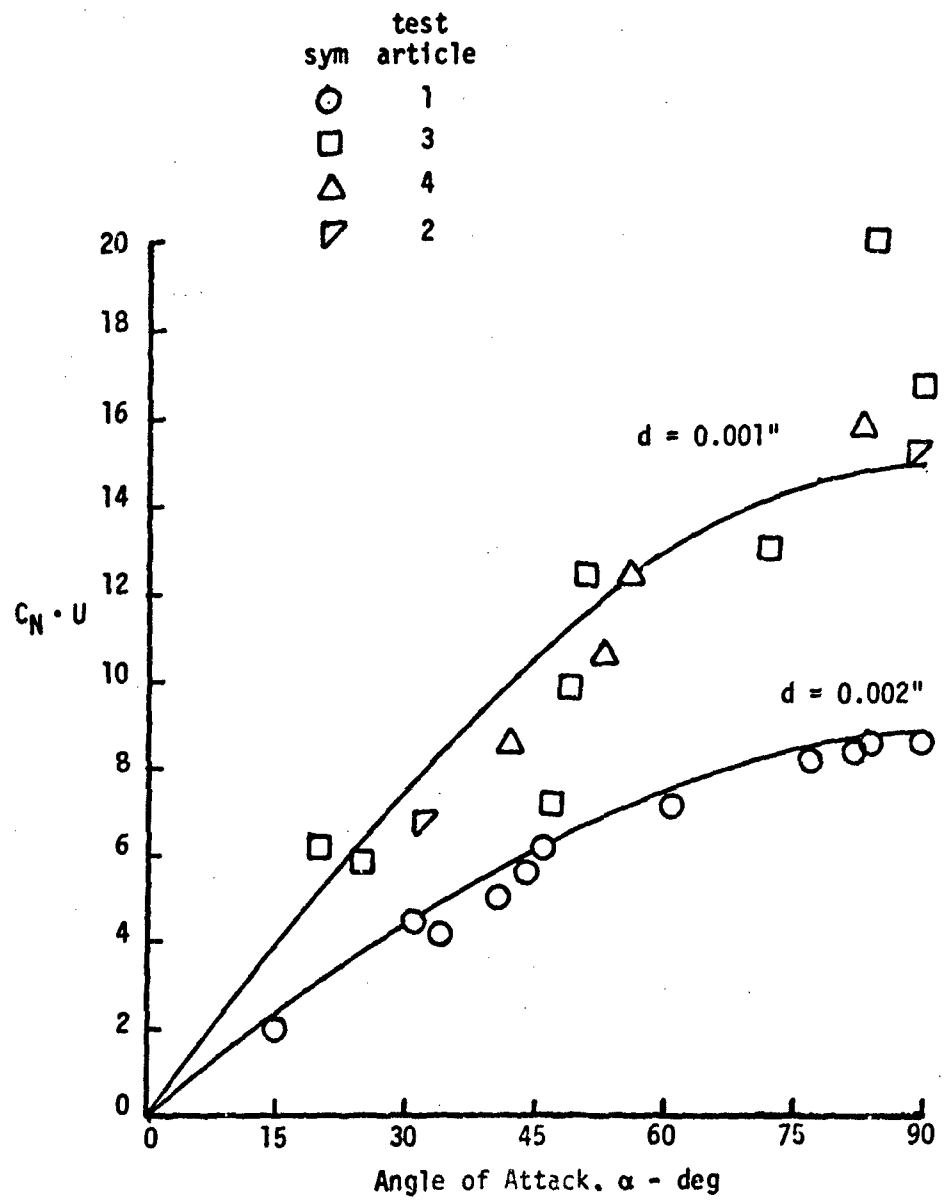


Figure 19. Correlation of Normal Force Coefficient Parameter  $C_N \cdot U$  with Angle of Attack for Class-Type Dipoles

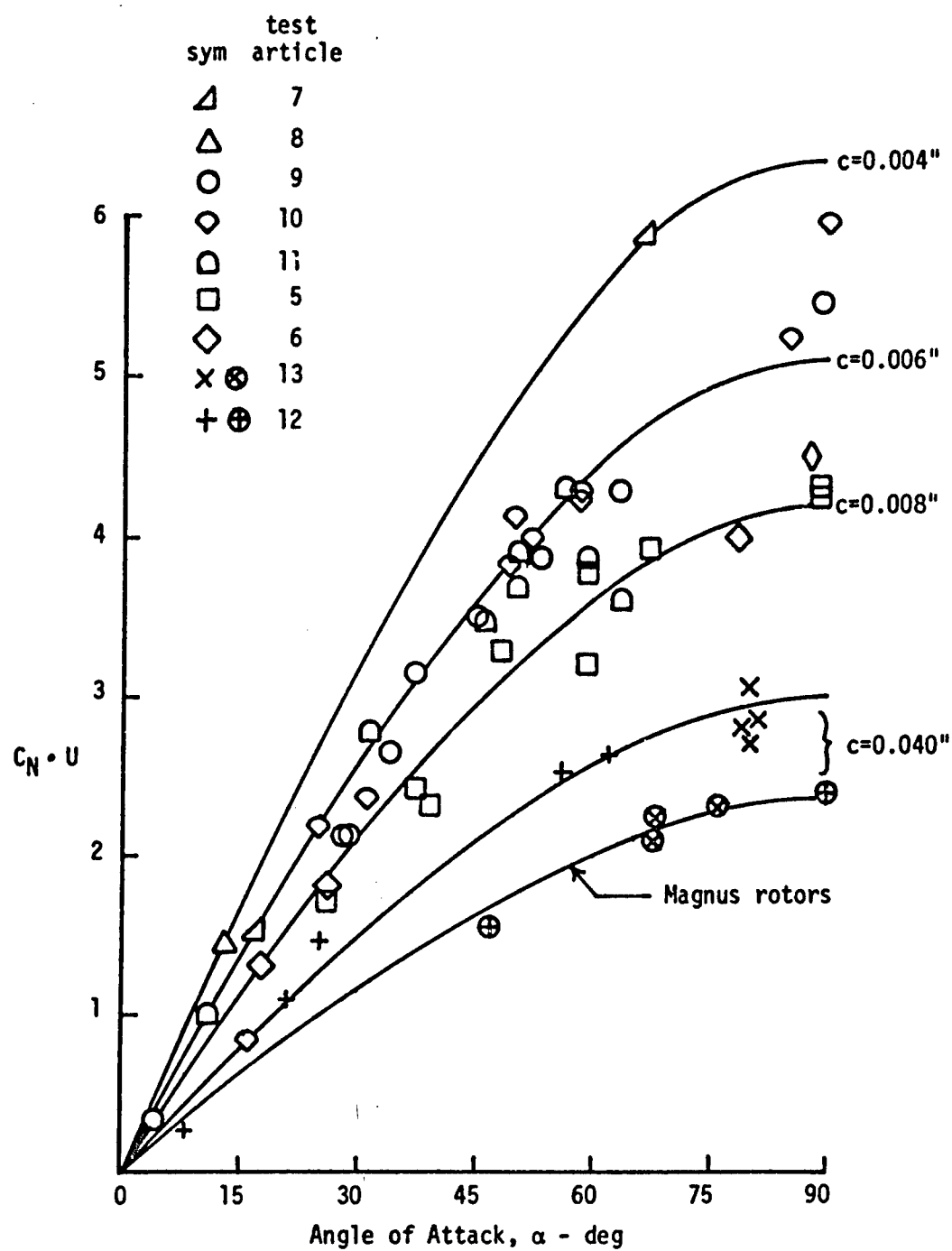


Figure 20. Correlation of Normal Force Coefficient Parameter  $C_N \cdot U$  with Angle of Attack (Foil-Type Dipoles)

Results for test articles 9 and 10 are shown in Figure 22. The data display a functional relation to  $\cos \alpha$ , which is again consistent with cross-flow theory.

The side force coefficient,  $C_{SF}$ , is present only when the dipole angular orientation,  $\Phi$ , is unsymmetric with respect to the cross flow, i.e.,  $\Phi \neq 0, \pi/2, \pi, \dots$ . For unsymmetric orientations the side force and normal force coefficients are related, theoretically. Using equations C-20 and C-21 of Appendix C it can be shown that

$$\frac{C_N}{C_{SF}} = \frac{\frac{16\pi}{R_N} \left( \frac{2\bar{S} - 1}{4\bar{S}^2} \right) + \frac{16\pi}{R_N} \left( \frac{1}{4\bar{S}^2} \right) \cos 2\Phi}{\left( \frac{16\pi}{R_N} \right) \left( \frac{1}{4\bar{S}^2} \right) \sin 2\Phi} \quad (8)$$

where the notation is that of Appendix C.

In Figure 23 Equation (8) is compared with experimental values of  $C_{SF}$  and  $C_N$  for three representative foil-type dipoles of identical cross-section (test articles 9, 10, and 11). Inspection shows that a majority of the experimental measurements correspond to values of  $\Phi$  less than 20 degrees and that nearly all of the experimental values are less than the theoretical boundary curve for  $\Phi = 45$  degrees. The result that  $\Phi$  is always less than 45 degrees appears reasonable in view of the stability theory for ellipsoids in an ideal fluid, which states that the body is stable only if the motion is in the direction of the least axis (for further discussion see Appendix C).

The side force coefficient has a different interpretation for those dipoles which experience autorotation about the longitudinal axis and fly at large angles of attack (Magnus rotor motion). In such cases, the side force coefficient corresponds to the classical magnus force, in accordance with the following sketch.

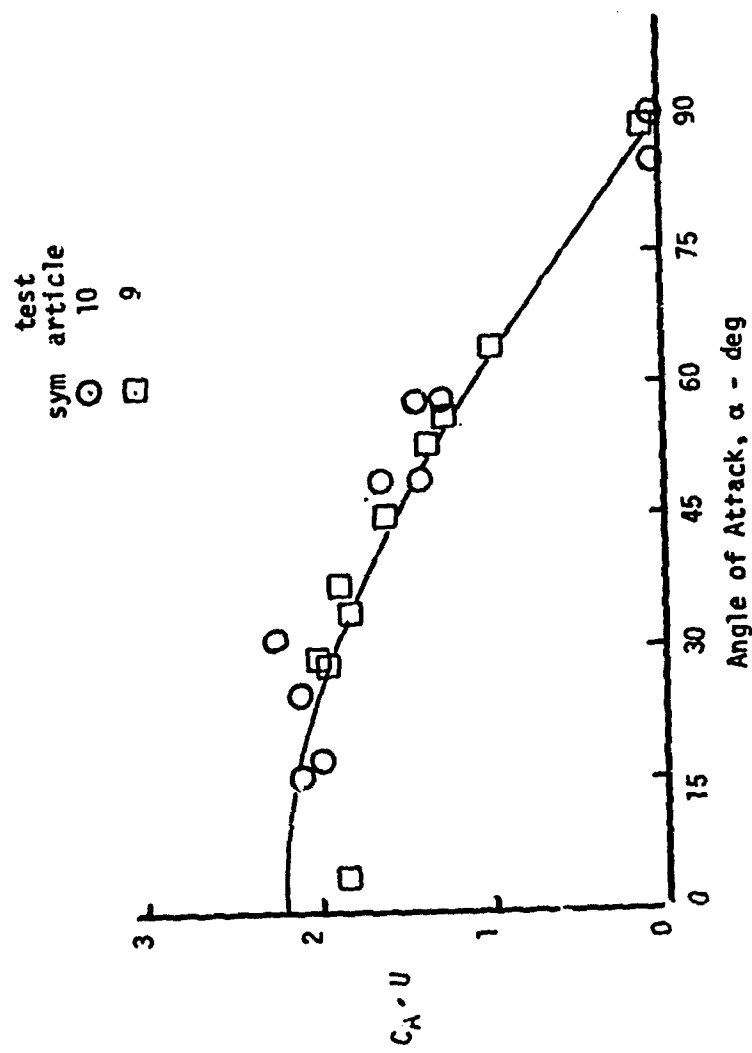


Figure 21. Correlation of Axial Force Coefficient Parameter  $C_A \cdot U$  with Angle of Attack (Foil-Type Dipoles)

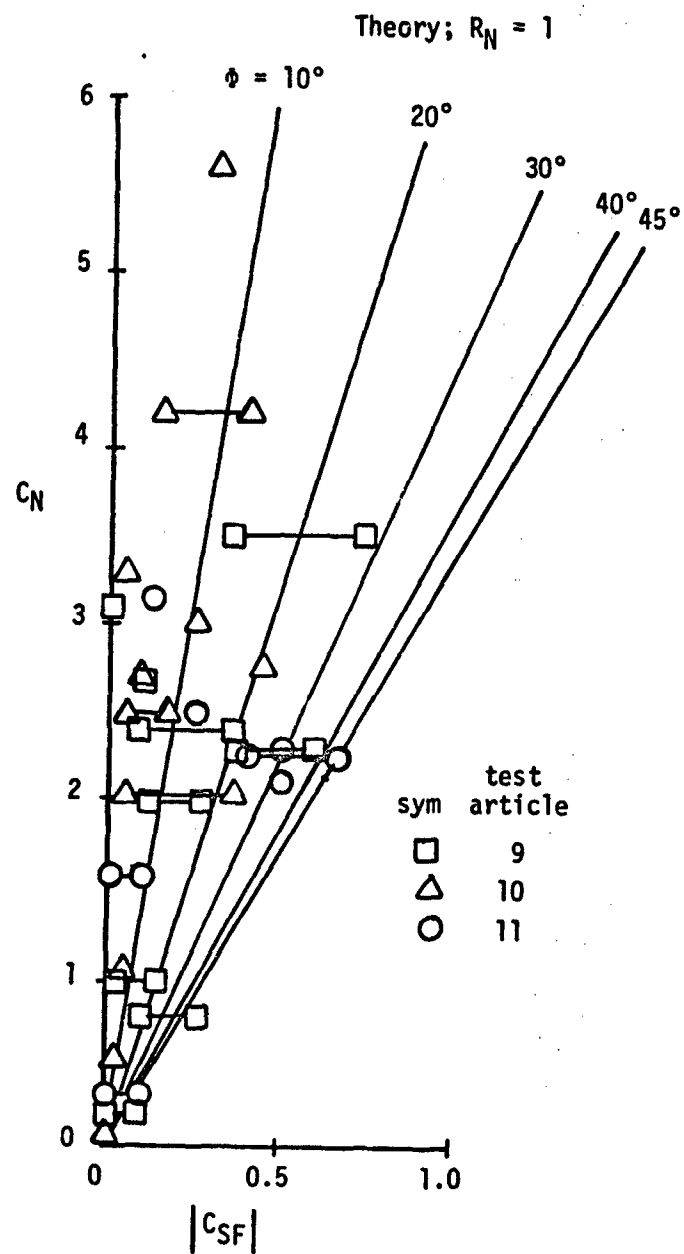
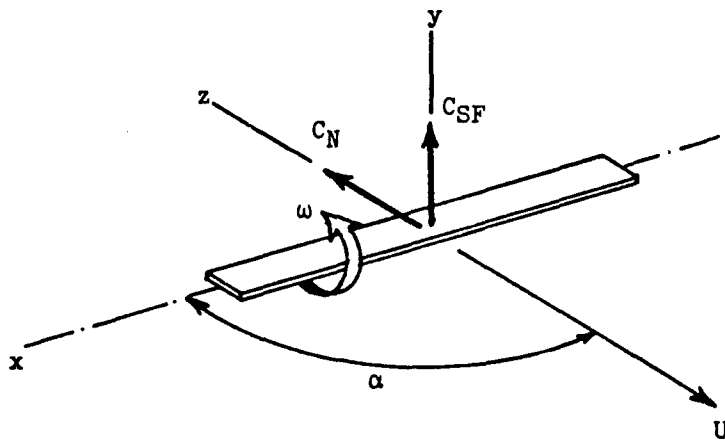


Figure 22. Correlation of Side Force Coefficient with Normal Force Coefficient for Foil-Type Dipoles



For all of those dipole flights which experienced magnus rotor motions the side force coefficient had a magnitude of about 0.25. Defining the magnus force coefficient as

$$C_{N_p} = \frac{\partial C_{SF}}{\partial \frac{\omega c}{2U}} \quad (9)$$

values of \$C\_{N\_p}\$ from about 6.0 to 9.0 were computed. No explanation can be given for these large values of \$C\_{N\_p}\$, which exceed in magnitude experimental measurements for rotating cylinders.

Aerodynamic Moment Coefficients At very low Reynolds numbers theory indicates that the moment due to fluid pressure vanish if the body has three mutually perpendicular planes of symmetry. Direct measurements of the dipole moment coefficients \$C\_M\$ and \$C\_{SM}\$ confirm the extremely small magnitude of the aerodynamic moments (see Figures 14 and 15). However, two significant sources of aerodynamic moment remain; 1) the moments due to configurational asymmetries, i.e., bending, twist, etc., and 2) the viscous moments caused by dipole angular motion. Since the measured moment coefficients reflect all three moment contributions, a separate determination of each moment contribution is, in general, impossible. Consequently, indirect methods of assessing the probable magnitude of the aerodynamic moment contributions were employed. The basic approach involved calculation of the viscous damping moment, and then inference of the static moment contributions of the symmetric and asymmetric dipole. The method of estimating the viscous damping is described in Appendix C for dipole

rotations about either the  $y$  or  $z$  axes of Figure 17. Using estimated damping moments the dipole equations of motion were then re-evaluated and the remaining static moment coefficients determined. Figure 24 illustrates the values of  $C_M$  and  $C_{SM}$  determined in this fashion, using motion data for a large selection of dipole configurations.

The following tentative conclusions are drawn from this data:

- 1) The static moment coefficient,  $C_M$ , for a symmetric dipole is extremely small and probably not larger than 0.005 for glass-type dipoles or larger than 0.015 for foil-type dipoles.
- 2) The side moment coefficient  $C_{SM}$  is significantly larger than the overturning moment coefficient  $C_M$ .
- 3) For foil-type dipoles both  $C_M$  and  $C_{SM}$  attain maximum values at an intermediate angle of attack in the neighborhood of  $\dot{\alpha} = 45^\circ$ , but for glass-type dipoles  $C_{SM}$  is maximum at small angles of attack.

The larger magnitude of  $C_{SM}$  compared to  $C_M$  for the foil type dipoles, is probably due to the presence of twist, which has a large contribution to  $C_{SM}$  but only a small contribution to  $C_M$ .

As a further means of investigating the magnitude of the static overturning moment, several drop tests of test article 1 were accomplished with intentional center-of-mass offset. The smallest offset tested ( $\Delta x \approx 0.01 \text{ ft}$ ) was sufficient to trim the dipole to an angle of attack approaching zero. From this it was inferred that the maximum static moment of the symmetric dipole could not have exceeded 0.03, thus confirming the test data shown in Figure 24.

Finally, a special experiment was conducted to provide a direct evaluation of the aerodynamic damping moment in pitch (see Section IV-6) for comparison with Equation (C-34) of Appendix C. By direct measurement it was found that  $M = -4.7 \times 10^{-9} \text{ ft-lb}$  and from Equation (C-34) a value of  $M = -2.4 \times 10^{-9} \text{ ft-lb}$  was obtained. Thus, the damping moment predictions are believed to be accurate within a factor of two, which is reasonable considering the extremely small magnitude of the moments.

A more extensive discussion of the moments due to configurational asymmetry can be found in Appendix C.

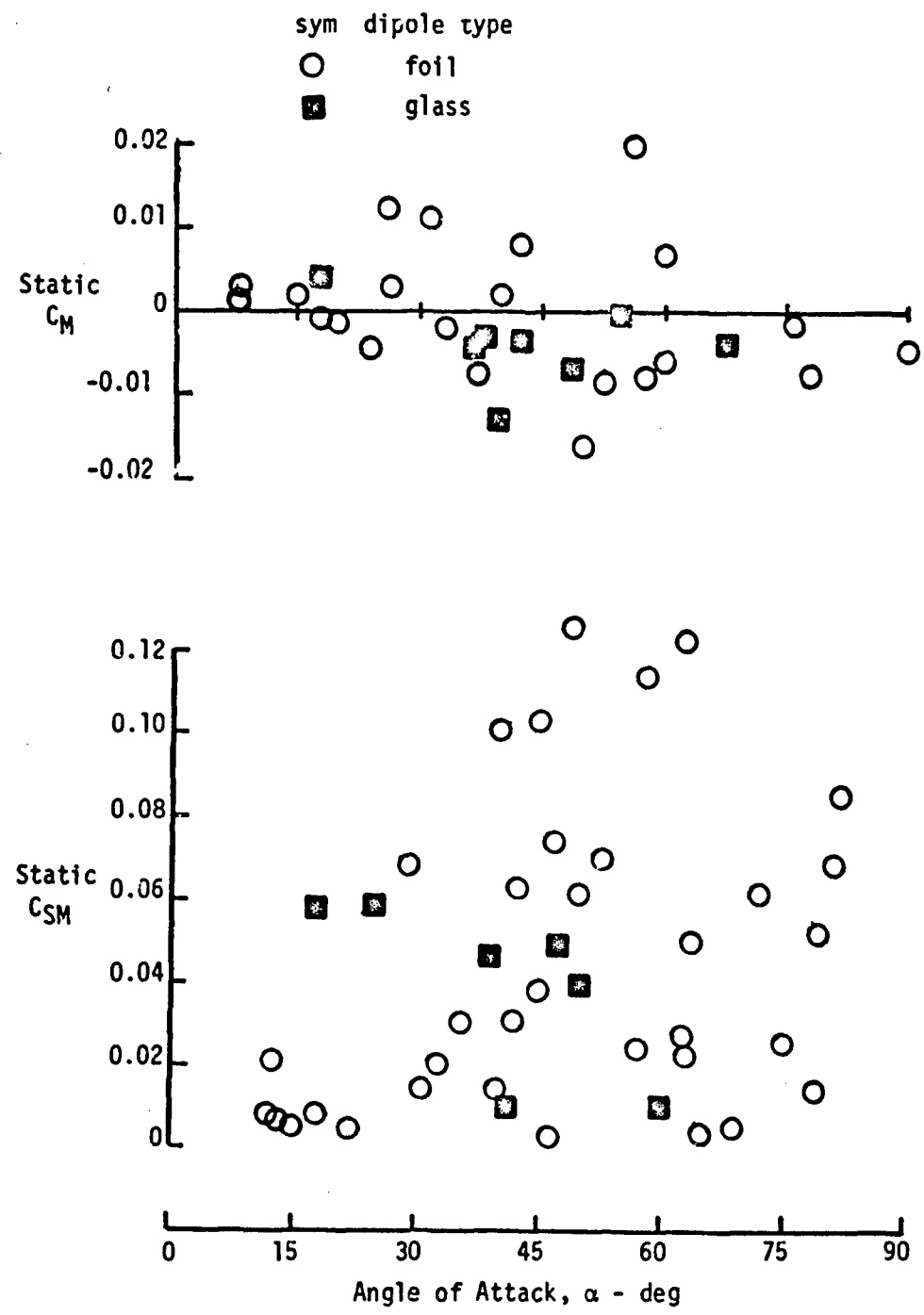


Figure 23. Correlation of Static Overturning Moment Coefficient and Static Side Moment Coefficient with Angle of Attack

#### **4. Chaff Cluster Dispersion Tests**

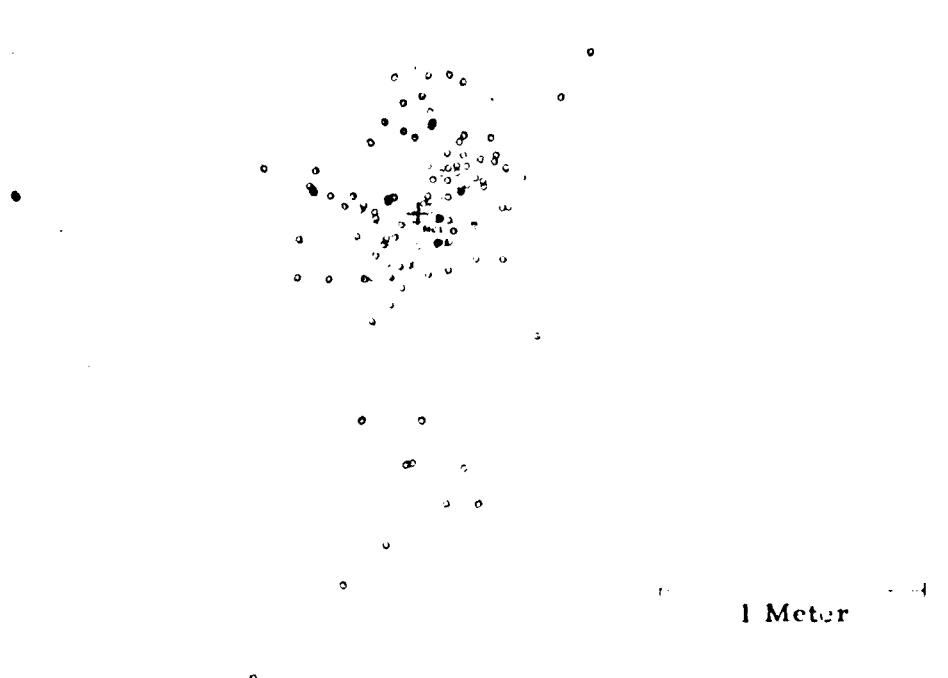
An experimental investigation of chaff cluster dispersion was accomplished as an adjunct to the basic aerodynamic test program. The purpose of the cluster drops was, 1) to assess the effect of dipole spiraling over a time span encompassing many cycles, 2) to determine the relative dispersion contributions of the transient and steady-state descent phases, and 3) to examine the possible contribution of atmospheric turbulence to chaff dispersion in an airship hangar environment. The tests were accomplished using chaff cluster of either 100 or 200 dipoles. All drops from 25 ft. height and above were accomplished in the MCAS airship hangar at Santa Ana, Calif. To minimize air circulation the tests were made between 3 - 6 A.M. with all the hangar doors closed.

Dispersion Patterns Ground level dispersion patterns for a representative small chord foil-type dipole (test article No. 9), as recorded from cluster releases at 25, 50, and 100 ft. above ground level are shown in Figure 25. Similar data were obtained for test article No. 12. The recovery factor for these drops varied from 100 percent at the lowest drop height to about 90 - 95 percent for the 100 ft. drop height. An attempt to measure the dispersion of the glass-type dipoles was unsuccessful because the recovery was less than 50 percent for the minimum drop height.

Statistical analysis of the impact patterns was accomplished using the cumulative frequency distribution for the radial deflection from the mean center of impact. The radial deflection statistics were found to closely match the two-dimensional normal distribution for cumulative frequencies up to about 80 percent, but for large dispersions the data showed non-Gaussian trends. Values of the probable dispersion (50th percentile) are shown as a function of release height in Figure 26 for both wide and narrow types of foil chaff.

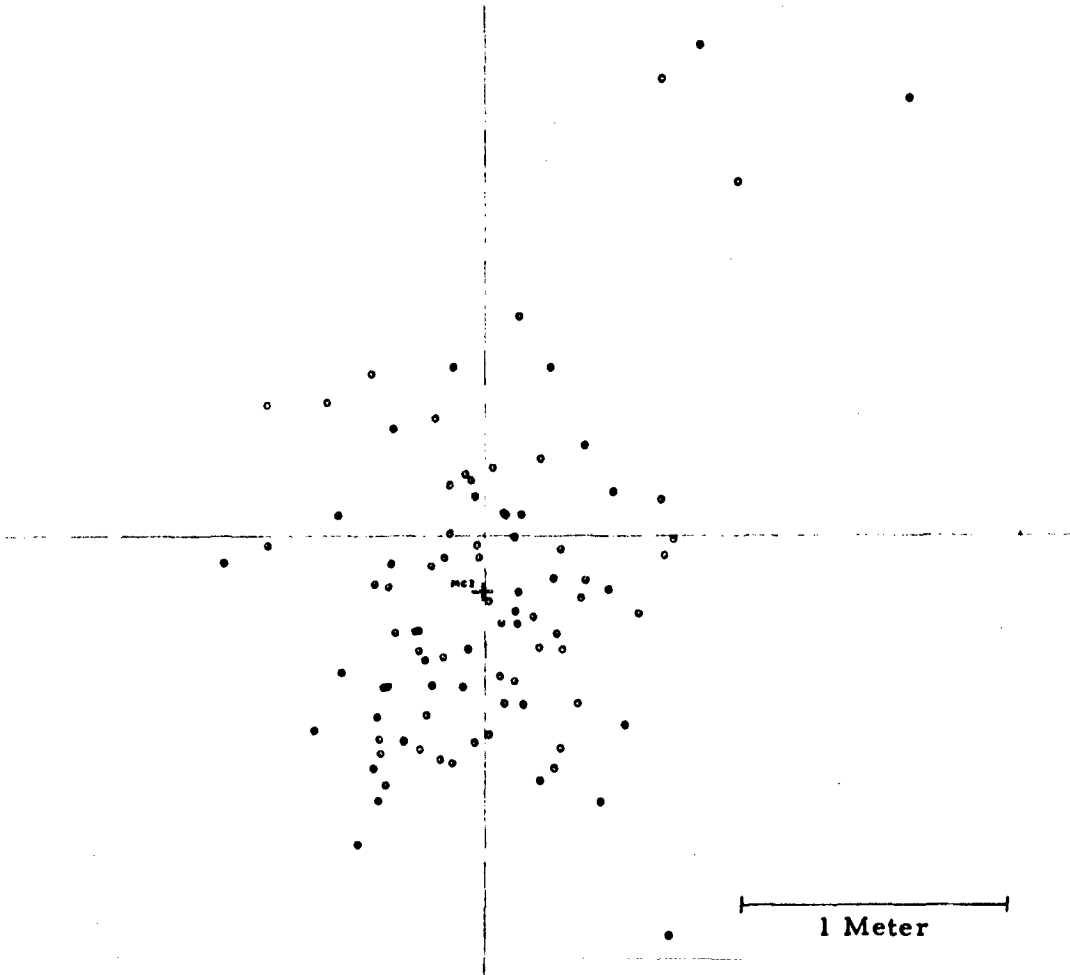
The test results indicate that for release heights above approximately 25 ft. the dipole dispersion is essentially constant, if the drops are accomplished in a protected environment. Below 25 ft., the dispersion increases rapidly with increasing release height. For a drop height of 100 ft. there is no significant difference in dispersion between the two dipole configurations tested.

Spiral Analysis Using probable values of spiral rate, descent velocity and flight path angle (as determined from the instrumented drop tests), the probable values of turning radius,  $R$ , and probable dispersion,



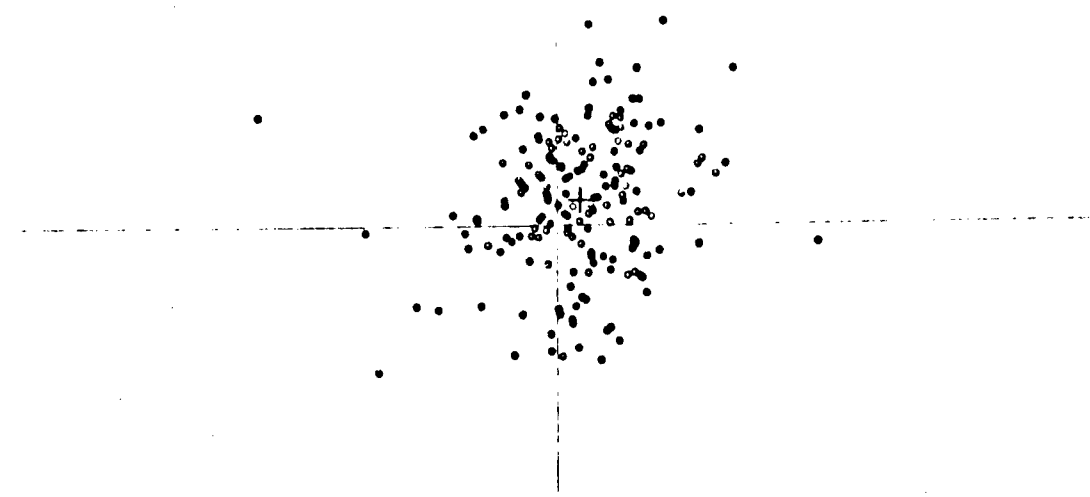
a) Release Height = 25 Feet

Figure 24. Ground-Level Dispersion Patterns  
for Small Chord Foil-Type Dipole  
as a Function of Release Height

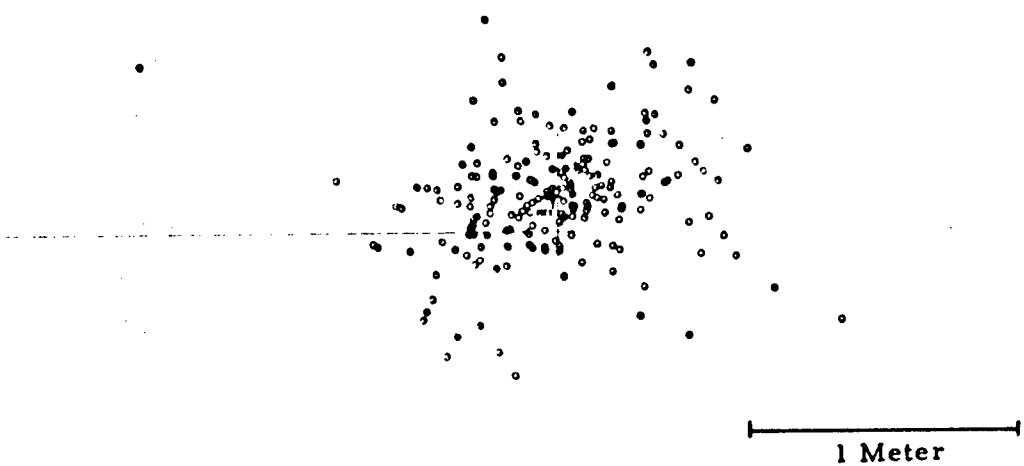


b) Release Height = 50 Feet

Figure 24. (Continued)



c) Release Height = 100 Feet

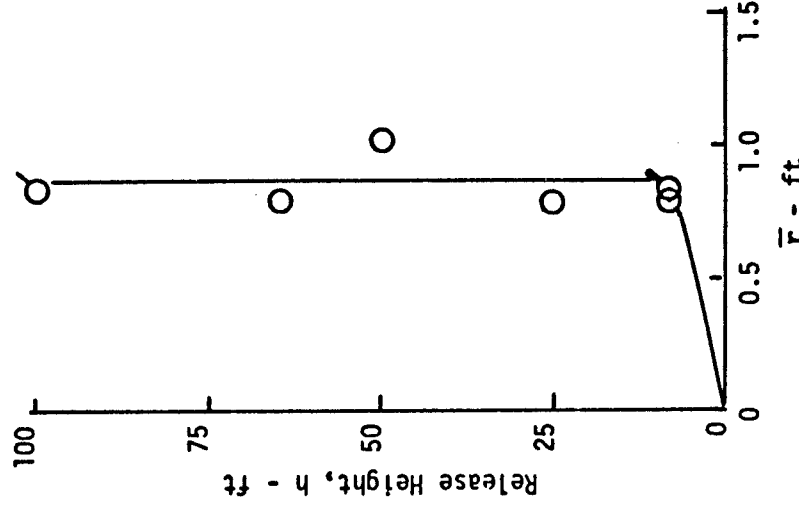


d) Release Height = 100 Feet (Repeat)

Figure 24. (Continued)

Large-Chord Foil Dipoles

- $\circ$  100 element cluster
- $\curvearrowleft$  200 element cluster



Small-Chord Foil Dipoles

- $\square$  100 element cluster
- $\curvearrowleft$  200 element cluster

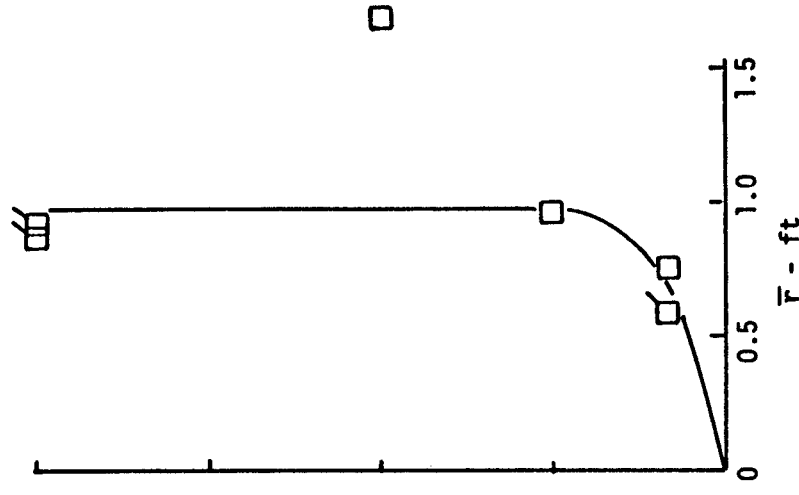


Figure 25. Probable Radial Dispersion from Mean Center of Impact as a Function of Cluster Release Height (Foil-Type Dipoles)

$\bar{r}$ , for a steady-state spiral were computed from Equations (C-42) and (C-47) of Appendix C. The results are given below:

Test Article	Dipole Dimensions inches	R ft.	$\bar{r}$ ft.
9	.006 x .00045 x 1.78	0.21	0.27
12	.040 x .00045 x 1.12	0.32	0.41

The probable dispersion due to steady-state spiralling as given by the table above is seen to be significantly less than the observed dispersion data shown in Figure 25. It can therefore be concluded that under quiescent atmosphere conditions the release transient is the primary source of dipole dispersion for descent distances of the order of 100 feet.

## SECTION VII

### SIX-DEGREES-OF-FREEDOM MOTION SIMULATION

#### 1. 6-DOF Computer Program

A specially modified 6-DOF computer program was prepared for simulation of the complete motion of single or multiple dipoles.

The basic computer program from which the final program was derived is the Alpha Research "Extended Capability Magnus Rotor and Ballistic Body 6-DOF Trajectory Program" which is documented in References 2, 3, and 4. The basic program has such features as

- all attitude motion prediction
- self-adjusting integration schemes
- option for either body-fixed or fixed-plane axes
- three parameter aerodynamic coefficient tables plus aerodynamic dependency upon roll orientation
- provision for aerodynamic, geometric, and inertial asymmetries
- Monte Carlo operation, i. e., random selection of initial motion parameters and asymmetries
- provision for modeling of an initial cluster break-up
- versatile input format in NAMELIST notation.

---

<sup>2</sup> Alpha Research, Inc., "User's Manual: Extended Capability Magnus Rotor and Ballistic Body 6-DOF Trajectory Program," Report No. AFATL-TR-70-40, May 1970.

<sup>3</sup> Alpha Research, Inc., "Amended User's Manual: Extended Capability Magnus Rotor and Ballistic Body 6-DOF Trajectory Program," Alpha Research Report No. 71-2, 26 March 1971.

<sup>4</sup> Alpha Research, Inc., "6-DOF Monte Carlo Trajectory Program", Alpha Research Report No. 72-0089-10, 29 September 1972.

For chaff simulation the following additional features were provided:

- atmospheric wind and turbulence model
- aerodynamic coefficient dependence upon Reynolds number
- special output format
- improved integration controls.

The atmospheric wind model has options for either steady winds of arbitrary direction, or an arbitrary vertical wind shear (of fixed directional heading) with superimposed isotropic stochastic turbulence. The turbulence model incorporates both Eulerian and Lagrangian scales, i.e., both spacial and time dependency. The correlation functions are tailored to chaff descent conditions.

A complete description of the turbulence modeling is presented in Appendix D. Selection of the turbulence option in the 6-DOF trajectory program requires only four additional parameters, which are input as table functions of altitude. Recommended values of the turbulence parameters, as well as a discussion of atmospheric turbulence measurements, may be found in Appendix E.

## 2. Aerodynamic Coefficient Data

Complete 6-DOF aerodynamic data packages have been prepared for two representative dipole configurations: the 1 mil x 1-inch glass-type dipole and .006 x .00045 x 1.78-inch foil-type dipole.

The aerodynamic coefficients for the 1 mil x 1-inch dipole are presented in Table 3 as a function of both angle of attack and Reynolds number,  $R_N(\ell)^*$ . The aerodynamic coefficient notation is consistent with Figure 17. The force coefficients,  $C_x$  and  $C_N$ , as well as the damping derivatives,  $C_{m_q}$  and  $C_{n_r}$ , are based on data of Figures 18 and 19, and the following relationships:

---

\* The 6-DOF trajectory program accommodates only one characteristic length and the dipole length,  $\ell$ , has been selected for this parameter.

Table 3. BASIC AEROBALLISTIC COEFFICIENTS FOR CYLINDRICAL GLASS DIPOLE (0.001 x 1.0 INCHES)

Table 3. AERODYNAMIC MOMENT COEFFICIENTS DUE TO BENDING FOR CYLINDRICAL GLASS DIPOLE  
 (0.001 x 1.0 INCHES) (Continued)

Coefficient	Reynolds Number $R_N(\theta)$	Angle of Attack, $\alpha_L$ - Degrees												
		0	15	30	45	60	75	90	105	120	135	150	165	180
$C_{M0} + C_{N0} + C_{Mg}$	125	.247	.230	.214	.175	.123	.064	0	.064	.123	.175	.214	.230	.247
	250	.309	.298	.268	.218	.154	.080	0	.080	.154	.218	.268	.298	.3C9
	500	.261	.252	.226	.185	.130	.067	0	.067	.130	.185	.226	.252	.261
	1000	.201	.194	.174	.142	.100	.052	0	.052	.100	.142	.174	.194	.201
	2000	.120	.116	.104	.085	.060	.031	0	.031	.060	.085	.104	.116	.120

$$C_x = (C_x)_{\alpha=0} \cos \alpha \quad (10)$$

$$C_N = (C_N)_{\alpha=\pi/2} \sin \alpha \quad (11)$$

$$C_{m_q} = - \frac{(C_N)_{\pi/2} \sin^2 \alpha}{6} \quad (12)$$

$$C_{n_r} = - \frac{(C_N)_{\pi/2}}{6} \quad (13)$$

The latter two formulas correspond to Equations (C-35) and (C-38) of Appendix C. The maximum value of the overturning moment coefficient was taken to be 0.005 based on the data of Figure 24. This value was assumed to be appropriate for the nominal descent Reynolds number. The moment coefficient was further assumed to decrease with decreasing Reynolds number in direct proportion to the change in Reynolds number. The roll damping coefficient,  $C_{\ell_p}$ , was estimated using the following relationship, which is similar to that for rotating spheres.

$$C_{\ell_p} = \frac{4 \pi}{R_N (\ell)} \frac{d}{\ell} \quad (14)$$

where

$d$  = dipole diameter

$\ell$  = dipole length

$R_N (\ell)$  = length Reynolds number

The body-fixed moment coefficient  $C_{M_\delta}$  is used to represent the effect of random longitudinal bend. The moment coefficient values are normalized such that the standard deviation of bend corresponds to a  $\delta$  value of unity. The corresponding value of the dipole longitudinal bend parameter,  $R/a$  (as described in Appendix C, Section 3) was arbitrarily established as 5.0. The moment coefficient due to longitudinal bend includes both the axial and normal force contributions as given by Equations (C-28) and (C-31), respectively.

The aerodynamic coefficients for the 0.006 x .00045 x 1.78-inch dipole are presented in Table 4. In addition to the functional dependence upon  $\alpha$  and  $R_N$ , the functional dependence upon the roll angle,  $\phi$ , is also incorporated through a set of additional harmonic coefficients defined as follows:

Table 4. BASIC AEROBALLISTIC COEFFICIENTS FOR FOIL DIPOLE (0.006 x .00045 x 1.78 INCHES)

Coefficient	Reynolds Number $R_N(\ell)$	Angle of Attack, $\alpha$ - Degrees											
		0	15	30	45	60	75	90	105	120	135	150	165
$C_X = -C_A$	375	-5.5	-5.3	-4.8	-3.9	-2.8	-1.4	0.0	1.4	2.8	3.9	4.8	5.3
	750	-2.6	-2.5	-2.3	-1.8	-1.3	-0.7	0.0	0.7	1.3	1.8	2.3	2.6
	1500	-1.3	-1.3	-1.1	-0.9	-0.7	-0.3	0.0	0.3	0.7	0.9	1.1	1.3
	3000	-0.7	-0.7	-0.6	-0.5	-0.4	-0.2	0.0	0.2	0.4	0.5	0.6	0.7
	6000	-0.4	-0.4	-0.3	-0.3	-0.2	-0.1	0.0	0.1	0.2	0.3	0.3	0.4
$C_N = C_N$	375	0.0	2.0	4.0	5.6	6.8	7.6	7.9	7.6	6.8	5.6	4.0	2.0
	750	0.0	1.1	2.2	3.1	3.8	4.3	4.4	4.3	3.8	3.1	2.2	1.1
	1500	0.0	0.8	1.5	2.1	2.6	2.9	3.0	2.9	2.6	2.1	1.5	0.8
	3000	0.0	0.6	1.1	1.6	1.9	2.1	2.2	2.1	1.9	1.6	1.1	0.6
	6000	0.0	0.4	0.9	1.2	1.5	1.6	1.7	1.6	1.5	1.2	0.9	0.4
$C_M = C_m$	375	.0000	.0006	.0011	.0013	.0011	.0006	.0000	-.0006	-.0011	-.0013	-.0011	-.0006
	750	.0000	.0013	.0022	.0025	.0022	.0013	.0000	-.0013	-.0022	-.0025	-.0022	-.0013
	1500	.0000	.0025	.0043	.0050	.0043	.0025	.0000	-.0025	-.0043	-.0050	-.0043	-.0025
	3000	.0000	.0050	.0087	.0100	.0087	.0050	.0000	-.0050	-.0087	-.0100	-.0087	-.0050
	6000	.0000	.0100	.0173	.0200	.0173	.0100	.0000	-.0100	-.0173	-.0200	-.0173	-.0100
$C_{Mq} = C_{mq}$	375	0.0	-0.1	-0.4	-0.8	-1.2	-1.5	-1.6	-1.5	-1.2	-0.8	-0.4	-0.1
	750	0.0	-0.1	-0.2	-0.5	-0.7	-0.9	-0.9	-0.9	-0.7	-0.5	-0.2	0.0
	1500	0.0	0.0	-0.2	-0.3	-0.5	-0.6	-0.7	-0.6	-0.5	-0.3	-0.2	0.0
	3000	0.0	0.0	-0.1	-0.3	-0.4	-0.5	-0.5	-0.5	-0.4	-0.3	-0.1	0.0
	6000	0.0	0.0	-0.1	-0.2	-0.3	-0.4	-0.4	-0.4	-0.3	-0.2	-0.1	0.0
$C_{NR} = C_{n_r}$	375	-1.6	-1.6	-1.6	-1.6	-1.6	-1.6	-1.6	-1.6	-1.6	-1.6	-1.6	-1.6
	750	-0.9	-0.9	-0.9	-0.9	-0.9	-0.9	-0.9	-0.9	-0.9	-0.9	-0.9	-0.9
	1500	-0.7	-0.7	-0.7	-0.7	-0.7	-0.7	-0.7	-0.7	-0.7	-0.7	-0.7	-0.7
	3000	-0.5	-0.5	-0.5	-0.5	-0.5	-0.5	-0.5	-0.5	-0.5	-0.5	-0.5	-0.5
	6000	-0.4	-0.4	-0.4	-0.4	-0.4	-0.4	-0.4	-0.4	-0.4	-0.4	-0.4	-0.4
$CLP = C_{f_p}$	375	$-1.13 \times 10^{-4}$											
	750	$-5.65 \times 10^{-5}$											
	1500	$-2.82 \times 10^{-5}$											
	3000	$-1.41 \times 10^{-5}$											
	6000	$-0.71 \times 10^{-5}$											
$CL \times 10^{-5}$ ( $CL = C_{f_g}$ )	375	.3	.3	.3	.2	.2	.1	0	-.1	-.2	-.2	-.3	-.3
	750	.7	.7	.6	.5	.4	.2	0	-.2	-.4	-.5	-.6	-.7
	1500	1.4	1.4	1.2	1.0	.7	.4	0	-.4	-.7	-1.0	-1.2	-1.4
	3000	2.7	2.6	2.3	1.9	1.4	.7	0	-.7	-1.4	-1.9	-2.3	-2.6
	6000	5.4	5.2	4.7	3.8	2.7	1.4	0	-.14	-2.7	-3.8	-4.7	-5.2

Note:  $C_{NPA} = C_{MPA} = 0$

Table 4. ADDITIONAL BODY-FIXED AERODYNAMIC COEFFICIENTS FOR FOIL DIPOLE  
(0.006 x .00045 x 1.78 INCHES) (Continued)

Coefficient	Reynolds Number $R_N(l)$	Angle of Attack, $\alpha_l$ - Degrees												
		0	15	30	45	60	75	90	105	120	135	150	165	180
$CM_0 = CN_0 = CM_S$	375	-.144	-.139	-.125	-.102	-.072	-.037	0	.037	.072	.102	.125	.139	.144
	750	-.102	-.099	-.088	-.072	-.051	-.026	0	.026	.051	.072	.088	.099	.102
	1500	-.092	-.089	-.080	-.065	-.046	-.024	0	.024	.046	.065	.080	.089	.092
	3000	-.078	-.075	-.068	-.055	-.039	-.026	0	.020	.039	.055	.068	.075	.078
	6000	-.071	-.069	-.061	-.050	-.036	-.018	0	.018	.036	.050	.061	.069	.071
CSF1	375	0	.47	.90	1.27	1.56	1.74	1.80	1.74	1.56	1.27	.90	.47	0
	750	0	.31	.60	.85	1.04	1.16	1.20	1.16	1.04	.85	.60	.31	0
	1500	0	.26	.50	.71	.87	.97	1.00	.97	.87	.71	.50	.26	0
	3000	0	.21	.40	.56	.69	.77	.80	.77	.69	.56	.40	.21	0
	6000	0	.21	.40	.56	.69	.77	.80	.77	.69	.56	.40	.21	0
CN1	375	0	.47	.90	1.27	1.56	1.74	1.80	1.74	1.56	1.27	.90	.47	0
	750	0	.31	.60	.85	1.04	1.16	1.20	1.16	1.04	.85	.60	.31	0
	1500	0	.26	.50	.71	.87	.97	1.00	.97	.87	.71	.50	.26	0
	3000	0	.21	.40	.56	.69	.77	.80	.77	.69	.56	.40	.21	0
	6000	0	.21	.40	.56	.69	.77	.80	.77	.69	.56	.40	.21	0
CM1	375	0	.002	.004	.005	.004	.002	0	-.002	-.004	-.005	-.004	-.002	0
	750	0	.005	.009	.010	.009	.005	0	-.005	-.009	-.010	-.009	-.005	0
	1500	0	.010	.015	.020	.015	.010	0	-.010	-.015	-.020	-.015	-.010	0
	3000	0	.020	.035	.040	.035	.020	0	-.020	-.035	-.040	-.035	-.020	0
	6000	0	.040	.069	.080	.069	.040	0	-.040	-.069	-.080	-.069	-.040	0
CSM1	375	0	.002	.004	.005	.004	.002	0	-.002	-.004	-.005	-.004	-.002	0
	750	0	.005	.009	.010	.009	.005	0	-.005	-.009	-.010	-.009	-.005	0
	1500	0	.010	.015	.020	.015	.010	0	-.010	-.015	-.020	-.015	-.010	0
	3000	0	.020	.035	.040	.035	.020	0	-.020	-.035	-.040	-.035	-.020	0
	6000	0	.040	.069	.080	.069	.040	0	-.040	-.069	-.080	-.069	-.040	0
CSM2	375	0	-.010	-.020	-.028	-.034	-.038	-.039	-.038	-.034	-.028	-.020	-.010	0
	750	0	-.007	-.013	-.018	-.023	-.025	-.026	-.025	-.023	-.018	-.013	-.007	0
	1500	0	-.006	-.011	-.016	-.019	-.021	-.022	-.021	-.019	-.016	-.011	-.006	0
	3000	0	-.004	-.009	-.012	-.015	-.016	-.017	-.016	-.015	-.012	-.009	-.004	0
	6000	0	-.004	-.009	-.012	-.015	-.016	-.017	-.016	-.015	-.012	-.009	-.004	0
$CLPHI \times 10^5$	375	0	-.4	-.9	-.1.2	-.1.5	-.1.6	-.1.7	-.1.6	-.1.5	-.1.2	-.9	-.4	0
	750	0	-.9	-1.7	-2.4	-2.9	-3.3	-3.4	-3.3	-2.9	-2.4	-1.7	-.9	0
	1500	0	-1.7	-3.4	-4.7	-5.8	-6.5	-6.8	-6.5	-5.8	-4.7	-3.4	-1.7	0
	3000	0	-3.5	-6.8	-9.5	-11.7	-13.0	-13.0	-13.5	-11.7	-9.5	-6.8	-3.5	0
	6000	0	-7.0	-13.5	-19.1	-23.4	-26.1	-27.0	-26.1	-23.4	-19.3	-13.5	-7.0	0

Note:  $PHSFD = PHMD = PHSM2D = 90.0$ ;  $PHND = PHSMID = PHLID = 0$

$$\Delta C_N = [C_{N1}(\alpha, R_N)] \sin 2\phi \quad (15)$$

$$\Delta C_{SF} = [C_{SF1}(\alpha, R_N)] \sin(2\phi + \pi/2) \quad (16)$$

$$\Delta C_M = [C_{M1}(\alpha, R_N)] \sin(2\phi + \pi/2) \quad (17)$$

$$\Delta C_{SM} = [C_{SM1}(\alpha, R_N)] \sin 2\phi \quad (18)$$

$$+ [C_{SM2}(\alpha, R_N)] \cos 2\phi$$

$$\Delta C_\ell = [C_{\ell\phi_1}(\alpha, R_N)] \sin 2\phi \quad (19)$$

The functional form of the above equations is derived from Appendix C, Section 2, and provides for not only the rotational symmetry of the foil-type dipole, but also for twist and longitudinal bend effects as given by Table C-1. The coefficient contributions from twist are normalized to a standard deviation  $\epsilon = 10$  degrees, while the contributions from longitudinal bending are normalized to a bend ratio  $R/a = 5.0$ .

The determination of the coefficient values, with the effect of  $\phi$  included, requires special attention. Consider, for example,  $C_N$  and  $C_{N1}$ . In accordance with Table C-1

$$C_N(\alpha, R_N) + C_{N1}(\alpha, R_N, \phi) = k_1 \sin \alpha + k_2 \sin \alpha \cos 2\phi$$

Therefore  $C_N(\alpha, R_N) = k_1 \sin \alpha \quad (20)$

$$C_{N1}(\alpha, R_N, \phi) = k_2 \sin \alpha \cos 2\phi \quad (21)$$

or  $C_{N1}(\alpha, R_N) = k_2 \sin \alpha \quad (22)$

However, the experimental data represent the maximum normal force ( $\phi \rightarrow 0$ ) and include both the  $C_N$  and  $C_{N1}$  contributions. Thus, for  $\alpha = \pi/2$

$$(C_N)_{\text{measured}} = (C_N)_{\pi/2} = k_1 + k_2 \quad (23)$$

maximum

To obtain  $k_1$  and  $k_2$ , separately, an additional relationship is required, such as the ratio of the minimum and maximum normal force. At sufficiently low Reynolds number the ratio of  $(C_N)_{\min}/(C_N)_{\max}$  can be obtained with the aid of Equation (C-20). For small Reynolds numbers this ratio is found to have a value of about 0.8. Defining the ratio  $(C_N)_{\min}/(C_N)_{\max}$  as  $C$ , it is easily shown that

$$k_1 = (C_N)_{\pi/2} \frac{1+C}{2} \quad (24)$$

$$k_2 = (C_N)_{\pi/2} \frac{1-C}{2} \quad (25)$$

For convenience, a summary of all the k's and K's used in computing the aerodynamic coefficient tables is given in Table 5. Insufficient data were available to determine  $K_2$ ;  $k_4$  was neglected because of its small contribution.

### 3. Coefficient Tables for Alternate Chaff Lengths

With appropriate adjustment of reference area, reference length, and the Reynolds number argument values, coefficient values in Tables 3 and 4 may be used without further modification for alternate chaff lengths provided that

- a) the dipole slenderness ratio remains large
- b) the longitudinal bend ratio,  $R/a$ , remains constant
- c) the twist angle,  $\epsilon$ , remains constant.

Defining a new chaff length,  $l'$ , the new Reynolds number argument values are

$$R_N(l') = R_N(l) \frac{l'}{l} \quad (26)$$

The aerodynamic reference area is either

$$S = dl' \text{ or } S = cl'$$

(for cylindrical and strip-type dipoles, respectively) and the aerodynamic reference length is  $l'$ .

Table 5. SUMMARY OF AERODYNAMIC CONSTANTS FOR COMPUTING  
COEFFICIENT FUNCTIONAL DEPENDENCE UPON  $\dot{\alpha}$  and  $\phi$

$R_N (\ell)$	$k_0$	$k_1$	$k_2$	$K_0$	$K_1$	$K_3 \times 10^5$	$K_4$	$K_7$ ( $\epsilon = 10^\circ$ )	$K_8 \times 10^5$
375	5.5	7.9	1.8	.0013	.005	- 1.7	-.144	-.039	.3
750	2.6	4.4	1.2	.0025	.01	- 3.4	-.102	-.026	.7
1500	1.3	3.0	1.0	.0050	.02	- 6.7	-.092	-.022	1.4
3000	0.7	2.2	0.8	.0100	.04	-13.5	-.078	-.017	2.7
6000	0.4	1.7	0.8	.0200	.08	-27.0	-.071	-.017	5.4

67

Note: k's and K's are defined in Table C-1.

#### **4. Monte Carlo Simulations**

To illustrate the use of 6-DOF simulation for chaff dipole motion analysis, a Monte Carlo trajectory analysis was accomplished for the .006 x .00045 x 1.78-inch foil-type dipole using the modified computer program described in Section (VI-1). For this series of trajectory simulations, a quiescent atmosphere without wind or turbulence was assumed.

Physical data for the 0.006 x .00045 x 1.78-inch foil-type dipole were taken from Table 2, and aerodynamic coefficient data from Table 4. The dipoles were assumed to be released from a fixed position with a random initial orientation. The dipoles were further assumed to have Gaussian center-of-mass statistics, with the standard deviations of center-of-mass offset corresponding to values of length, width, and thickness of 0.005 $\ell$ , 0.01c, and 0.02t, respectively. The standard deviation of dipole longitudinal bend was taken as  $R/a = 5.0$  (i.e.,  $R = 4.45$  inches) and the standard deviation of element twist was assumed to be 10 degrees.

The 6-DOF motion calculations were performed with the computer program set for the Monte Carlo mode. For this series of simulations the integration time interval was automatically adjusted and was nominally in the range of 0.001 - 0.004 seconds.

Figure 27 depicts the XY coordinates of the ten sample trajectories which were computed for standard sea level conditions. These trajectories represent a flight time of 4.0 seconds. The projected orientation of each dipole at a representative point along its trajectory is illustrated as a means of further portraying the computed motion. The computed descent velocity varied from 1.1 to 1.9 ft/sec, which compare with measured velocities of 1.1 to 3.4 ft/sec for this dipole configuration.

Although no statistical analyses of the computed motions were accomplished, qualitatively the data appear quite similar to that obtained in the aerodynamic test chamber.

#### **5. Simulation of Dipole Flight in a Turbulent Atmosphere**

Several six-degrees-of-freedom simulations of dipole flight under turbulent atmospheric condition were accomplished with the specially modified 6-DOF computer program, using representative low and high

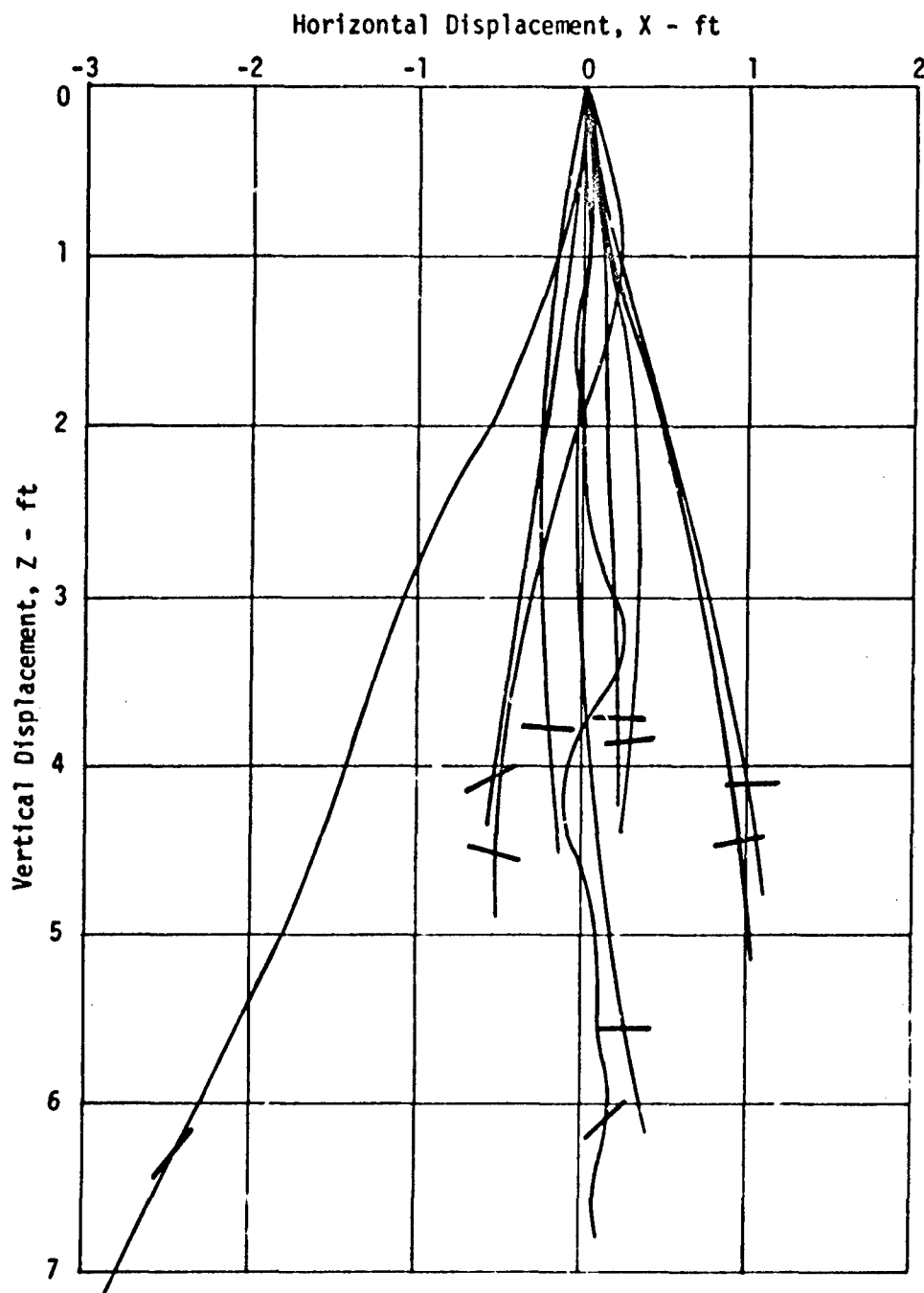


Figure 26. Monte Carlo Trajectory Simulation for  
.006 x .00045 x 1.78-inch Foil-Type Dipole  
(Zero Wind)

altitude turbulence intensities. Motion simulations were accomplished for both the 1 mil x 1-inch and .006 x .00045 x 1.75-inch dipole configurations. As with the Monte Carlo simulations, random initial conditions and configurational asymmetries were introduced.

Figure 28 illustrates typical motion data for the .006 x .00045 x 1.78-inch foil-type dipole in low altitude turbulence starting at an initial height 50 ft. above ground level. The turbulence parameters from Table E-2 were used as input to the computer program for this simulation.

It is seen from Figure 28 that turbulence affects, primarily, the inertial velocity components, such as the vertical descent rate which is shown. The aerodynamic velocity, i.e., the velocity of the element minus the wind velocity, fluctuates only slightly. A very significant result is that the dipole attitude variation (as represented by the Euler angles  $\theta$  and  $\psi$ ) is quite steady, even though the orientation of the flow relative to the dipole varies widely. Thus, the angular motion of the dipole is practically unaffected by turbulence. This is probably due to the aerodynamic damping, which is extremely large in comparison to forcing moments. The translational motion of the dipole with respect to an observer moving with the mean wind, on the other hand, would appear erratic, and might be termed a "jitter" motion.

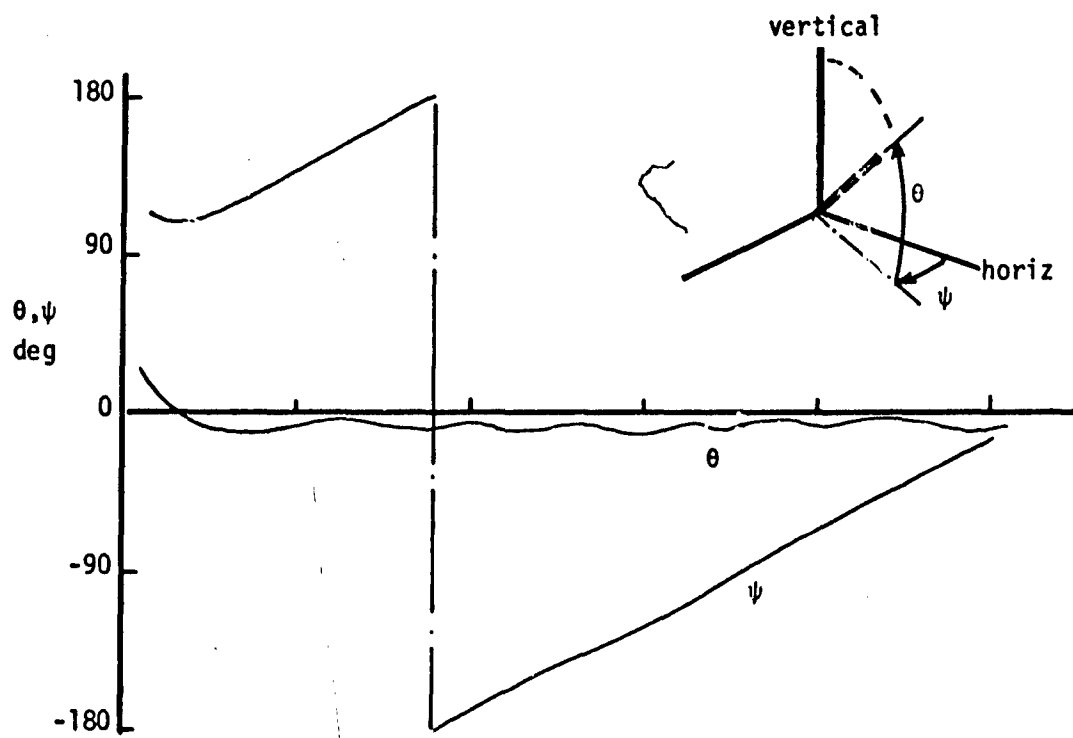
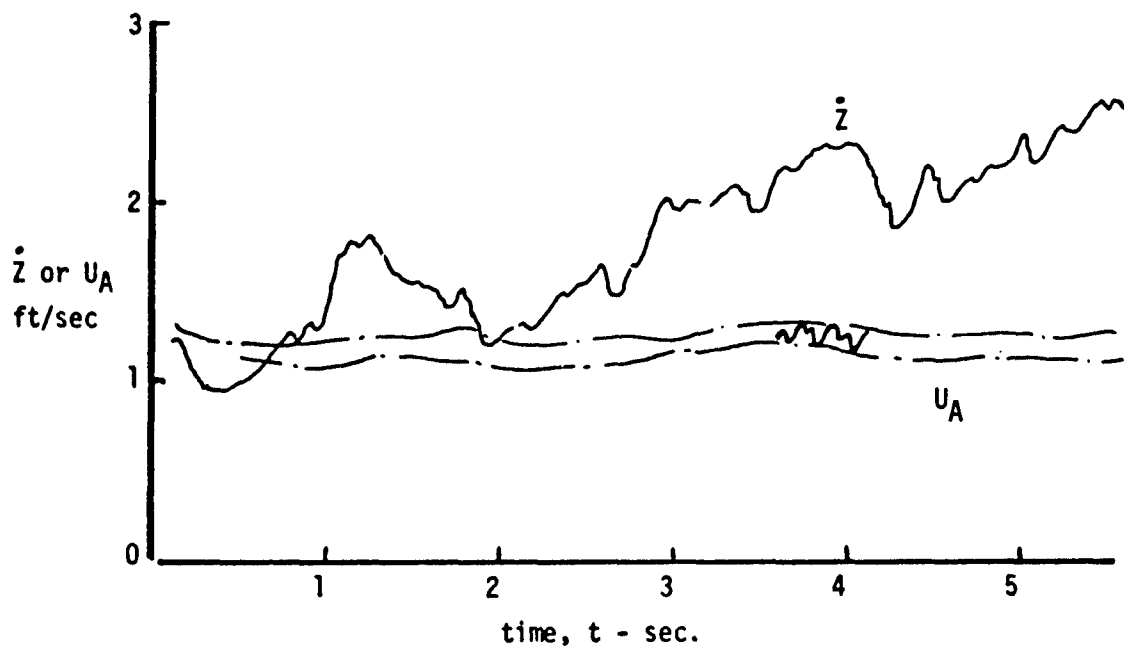


Figure 27. Motion Simulation with Representative Low Altitude Turbulence (.006 x .00045 x 1.78-inch Foil-Type Dipole)

## SECTION VIII

### SUMMARY, CONCLUSIONS, AND RECOMMENDATIONS

The aerodynamic characteristics of thirteen distinct dipole configurations, varying in construction, cross-section, and length, were determined from instrumented drop tests of single elements in an enclosed test chamber. The dipole motion was recorded photographically with three orthogonal still cameras equipped with synchronized rotating shutters.

The dynamic behavior of a chaff dipole was found to depend greatly upon its principal cross-sectional dimension. Dipoles with cross-sectional dimensions equal or less than about 0.008 inches exhibited a singular characteristic spiral motion, even though there were large differences in spiral rate and trim orientation. In all cases the spiral rate and dipole yawing rate were essentially equal. Dipoles with a characteristic cross-sectional dimension of 0.040 inches were dynamically more active and sometimes displayed autorotations about either the longitudinal axis or a transverse axis.

Aerodynamic force coefficients for all of the dipole configurations could be correlated with the cross-Reynolds number. With appropriate choice of parameters both the normal force and axial force coefficients were found to be independent of dipole length and cross-sectional shape, and dependent only upon angle of attack and Reynolds number. Agreement of the dipole drag data with theory and other experimental data on cylinders at low Reynolds number is good. For the smallest dipole diameter, a maximum drag coefficient of 38 was determined.

The static aerodynamic moments acting upon the dipoles with characteristic cross-section dimensions equal or less than 0.008 inches were found to be extremely small and due primarily to configurational asymmetries such as longitudinal bending and twist. Procedures for estimating the forces and moments due to asymmetry, and the angular velocity damping were derived, and these methods were generally substantiated by the test data.

Using both the experimental data and aerodynamic theory, 6-DOF aerodynamic data packages were prepared for two representative dipole configurations. These aerodynamic data packages were used in conjunction with a specially modified 6-DOF computer program to simulate the

dipole motion under both quiescent and stochastic turbulent atmospheric conditions. Both single element and Monte Carlo type simulations, with random initial conditions and dipole configurational asymmetries, were accomplished. The computed dipole trajectories and motion are in qualitative agreement with the experimental motion data. The effect of turbulence on the dipole motion was found to be primarily a translational jitter. The dipole angle motion is relatively insensitive to turbulent wind fluctuations.

The dispersive characteristics of chaff dipole clusters, for drop heights from 8 - 100 ft. above ground level, were determined from drop tests in an aircraft hangar under quiescent atmospheric conditions. For this range of drop heights chaff dispersion is due largely to the dipole initial motion transient and the dispersion is nearly constant for drop heights between 25 and 100 feet.

The present effort has provided a general understanding of chaff dipole aerodynamics and dynamic behavior. It has also provided the means for analytic simulation of chaff dipole motion in the presence of stochastic environments. However, much remains to be done in terms of assessing the relationship between chaff element dynamics and chaff cloud electromagnetic performance. Specific areas of work or studies which should be accomplished include:

- 1) Monte Carlo simulations with large sample size
- 2) more detailed study of the relationship between dipole asymmetry and its motion
- 3) investigation of simplified aerodynamic models as a means of reducing computer time requirements for 6-DOF simulations
- 4) evolution of improved dipole configurations on the basis of analytical simulation of chaff cluster dynamic behavior and electromagnetic performance.

## APPENDIX A

### PHOTOGRAMMETRIC DATA REDUCTION

The descent trajectories of the aerodynamic test dipoles are recorded by three still cameras with rotating shutters (Figure A-1). These cameras are so arranged as to provide orthogonal views of the drop test chamber from each of two camera pairs (cameras 1 and 2 or cameras 1 and 3). The instantaneous position and orientation of the descending dipole is documented by multi-image tracings on each film negative. Through photogrammetric analysis the true pitch and yaw attitudes of the dipole are described in standard Euler spherical angles and the dipole space position is determined in rectangular space coordinates. The photogrammetric data reduction procedure also removes all optical parallax errors.

Because the dipole position and attitude can be determined by either of two camera pairs, the above described motion recording system has a valuable redundancy. This redundancy feature can be exploited when the image quality is poor from one camera station, or when the aspect of one camera is unfavorable for accurate attitude and position determination.

#### 1. Determination of Dipole Position and Attitude (Cameras 1 and 3)

Cameras 1 and 3 comprise one of the orthogonal sets, with the camera-3 axis positioned such that it is  $\theta_0$  degrees off vertical. The camera-1 axis is aligned horizontally. The determination of dipole position and attitude from cameras 1 and 3 is slightly more involved than with cameras 1 and 2.

Let the location of the lens of camera 3 be defined as  $X = b$ ,  $Y = d$ , and  $Z = e$ . The XY plane bisects the center of the 4-ft cube test chamber, and the lens axes of cameras 1 and 2 both lie in this plane. The lens of camera 1 is located at  $X = a$ ,  $Y = b$ , and  $Z = 0$  in accordance with Figure A-1.

Let the chaff dipole be located in the 4-ft-cube drop-test zone at  $X_p$ ,  $Y_p$ ,  $Z_p$ , and let the cameras be located as indicated previously. A line through Camera 1 and the geometric center of the particle has the equation:

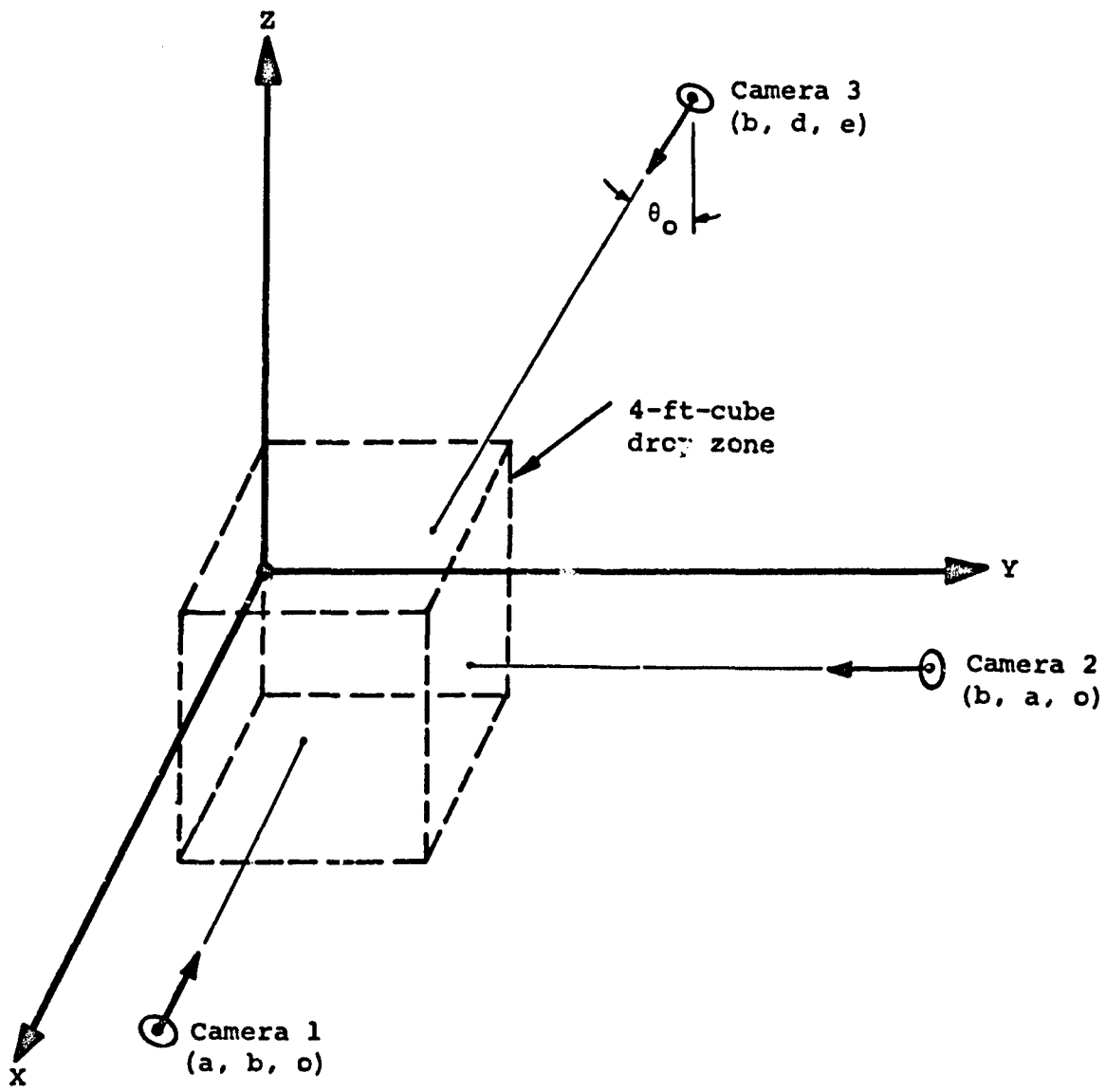


Figure A-1. Coordinate System for Motion Recording Cameras

$$\frac{X-a}{X_p-a} = \frac{Y-b}{Y_p-b} = \frac{Z-0}{Z_p-0} \quad (A-1)$$

The intersection of this line and the YZ plane is at:

$$Y = n_1, Z = \zeta_1, X = 0$$

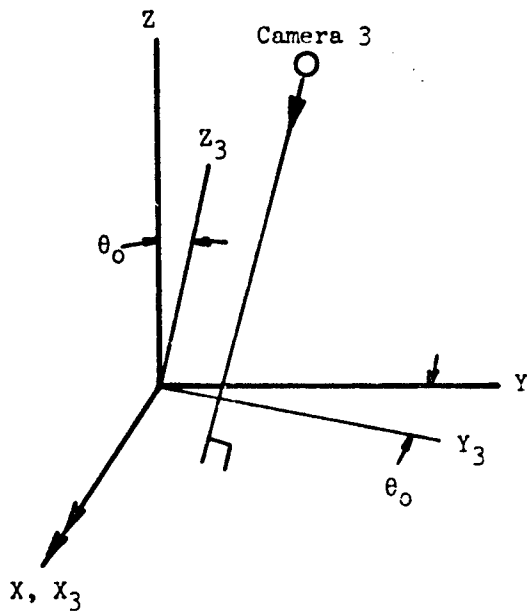
Thus  $n_1 = b-a \left[ \frac{Y_p-b}{X_p-a} \right] \quad (A-2)$

$$\zeta_1 = -a \left[ \frac{Z_p}{X_p-a} \right] \quad (A-3)$$

Consider a line from camera 3 to the particle as having the equation:

$$\frac{X-b}{X_p-b} = \frac{Y-d}{Y_p-d} = \frac{Z-e}{Z_p-e} \quad (A-4)$$

A new coordinate system is now defined in which plane  $X_3Y_3$  is perpendicular to the center-view axis of camera 3.



The transformation matrix is:

$$\begin{bmatrix} X \\ Y \\ Z \end{bmatrix} = \begin{bmatrix} 1 & 0 & 0 \\ 0 & C_{22} & C_{23} \\ 0 & C_{32} & C_{33} \end{bmatrix} \begin{bmatrix} X_3 \\ Y_3 \\ Z_3 \end{bmatrix}$$

Substituting these values into Equation (A-4) results in

$$\frac{X_3 - b}{X_p - b} = \frac{C_{22}Y_3 + C_{23}Z_3 - d}{Y_p - d} = \frac{C_{32}Y_3 + C_{33}Z_3 - e}{Z_p - e} \quad (A-5)$$

The image in the  $X_3Y_3$  plane when looking through camera 3 appears to be at

$$X_3 = \xi_3, Y_3 = \eta_3, Z_3 = 0$$

Substituting these values to Equation (A-5) and combining with Equation (A-2)  $X_p$ ,  $Y_p$ , and  $Z_p$  are determined as follows:

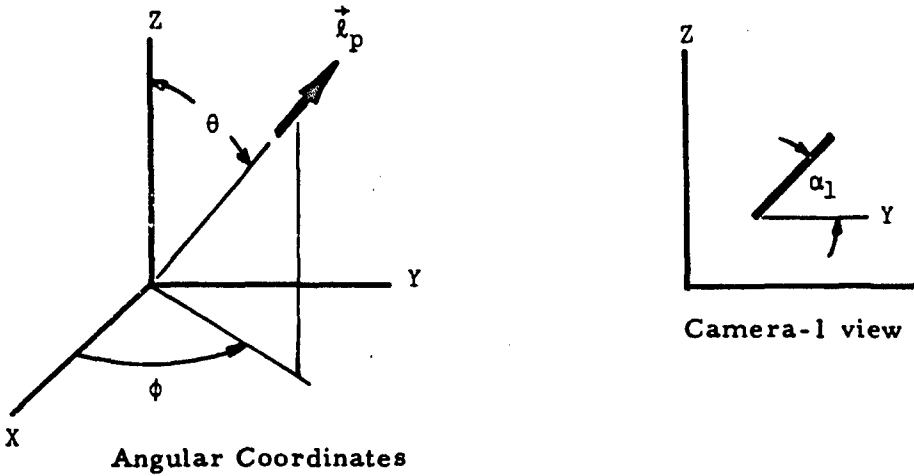
$$X_p = \frac{\eta_1 - d + b/f_3}{\left(1/f_3 + \frac{\eta_1 - b}{a}\right)} \quad (A-6)$$

$$Y_p = b - (X_p - a)(\eta_1 - b)/a \quad (A-7)$$

$$Z_p = -\frac{\zeta_1}{a}(X_p - a) \quad (A-8)$$

Equations (A-6), (A-7), and (A-8) are used to locate the position of the dipole.

Let  $\theta$  and  $\phi$  be the Euler angles describing the attitude of the long axis of the dipole. Also define  $\alpha_1$  as the angle seen effectively between the filament axis and the Y axis in the YZ plane in accordance with the sketches on the following page.



The following direction vectors are now defined:

$\vec{l}_p$  = direction vector through the filament axis

$\vec{l}_p = \sin \theta \cos \phi \vec{i} + \sin \theta \sin \phi \vec{j} + \cos \theta \vec{k}$

$\vec{l}_1$  = direction vector from the particle to camera 1

$\vec{l}_1 = (X_p - a) \vec{i} + (Y_p - b) \vec{j} + Z_p \vec{k}$

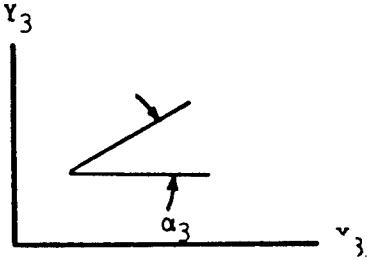
If the coefficients of a normal vector are  $\vec{n} = \vec{l}_1 \times \vec{l}_p$ , then the plane which contains  $\vec{l}_1$  and  $\vec{l}_p$  can be determined. The intersection between this plane and the YZ plane ( $X = 0$ ) is a line with the slope:

$$m = \tan \alpha_1 = \frac{(X_p - a) \cos \theta - Z_p \sin \theta \cos \phi}{(X_p - a) \sin \theta \sin \phi - (Y_p - b) \sin \theta \cos \phi} \quad (A-9)$$

Rearranging,

$$\tan \theta_p = \frac{X_p - a}{[(X_p - a) \tan \alpha_1 \sin \phi - (Y_p - b) \tan \alpha_1 \cos \phi + Z_p \cos \phi]}$$

Now consider the  $X_3Y_3Z_3$  grid space where  $\alpha_3$  is defined as the angle between the dipole axis and the  $X_3$  axis in the  $X_3Y_3$  plane.



In the  $X_3Y_3Z_3$  coordinates, Camera 3 is located at  $(b_3g_3h_3)$ , where:

$$b_3 = b$$

$$g_3 = C_{22}d + C_{32}e$$

$$h_3 = C_{23}d + C_{33}e$$

$\vec{l}_3$  = vector from the particle to Camera 3

$$\vec{l}_3 = (X_p - b_3) \vec{i}_3 + (Y_p - g_3) \vec{j}_3 + (Z_p - h_3) \vec{k}_3$$

The direction vector  $\vec{l}_p$  was given previously, but transformed to  $X_3Y_3Z_3$  coordinates becomes:

$$\begin{aligned} \vec{l}_p = & \sin \theta_p \cos \phi_p \vec{i}_3 + (C_{22} \sin \theta_p \sin \phi_p + C_{32} \cos \theta_p) \vec{j}_3 \\ & + (C_{23} \sin \theta_p \sin \phi_p + C_{33} \cos \theta_p) \vec{k}_3 \end{aligned}$$

Thus, the normal is given by:

$$\vec{n} = \begin{bmatrix} \vec{i}_3 & \vec{j}_3 & \vec{k}_3 \\ X_p - b_3 & Y_p - g_3 & Z_p - h_3 \\ \sin \theta \cos \phi & C_{22} \sin \theta \sin \phi & C_{23} \sin \theta \sin \phi \\ & + C_{32} \cos \theta & + C_{33} \cos \theta \end{bmatrix}$$

By similarly using the coefficients of  $\vec{n}$ , a plane can be defined perpendicular to  $\vec{n}$ . This plane intersects the  $X_3Y_3$  plane at  $Z_3 = 0$ . The slope of that line is:

$$m_3 = \tan \alpha_3 = - \frac{\text{coeff}(\vec{i}_3 \text{ term})}{\text{coeff}(\vec{j}_3 \text{ term})}$$

$$\tan \alpha_3 = \frac{Y_{p_4} (d_2 C_{23} + d_3 C_{33}) - Z_{p_4} (d_2 C_{22} + d_3 C_{32})}{X_{p_4} (d_2 C_{23} + d_3 C_{33}) - Z_{p_4} d_1}$$

where

$$d_1 = \sin \theta \cos \phi$$

$$d_2 = \sin \theta \sin \phi$$

$$d_3 = \cos \theta$$

$$X_{p_4} = X_{p_3} - b_3$$

$$Y_{p_4} = Y_{p_3} - g_3$$

$$Z_{p_4} = Z_{p_3} - h_3$$

Rearranging,

$$\begin{aligned} \cos \phi &= [(X_{p_4} \tan \alpha_3 (d_2 C_{23} + d_3 C_{33}) - Y_{p_4} (d_2 C_{23} + d_3 C_{33})) \\ &\quad + Z_{p_4} (d_2 C_{22} + d_3 C_{32})] / (Z_{p_4} \tan \alpha_3 \sin \theta) \end{aligned} \quad (\text{A-10})$$

Equations (A-9) and (A-10) are combined and the angles  $\phi$  and  $\theta$  are determined explicitly.

$$\phi = \tan^{-1} \frac{Z_{p_4} \tan \alpha_3 + \frac{M_1(Y_p - b)}{(X_p - a)} \tan \alpha_1 - \frac{M_1 Z_p}{X_p - a}}{M_p \tan \alpha_1 + M_2} \quad (\text{A-11})$$

$$\theta = \tan^{-1} \frac{X_p - a}{(X_p - a) \tan \alpha_1 \sin \phi - (Y_p - b) \tan \alpha_1 \cos \phi + Z_p \cos \phi} \quad (\text{A-12})$$

where  $M_1 = -C_{33} Y_{p_4} + C_{32} Z_{p_4} - C_{33} X_{p_4} \tan \alpha_3$

$$M_2 = -C_{23} Y_{p_4} + C_{22} Z_{p_4} + C_{23} X_{p_4} \tan \alpha_3$$

Thus, Equations (A-6), (A-7), (A-8), A-11, and (A-12) form a complete set of formulae for determining positions and angles from Cameras 1 and 3.

2. Determination of Dipole Position and Attitude (Cameras 1 and 2)

The determination of dipole position and attitude from the two horizontally aligned cameras is accomplished in a manner similar to that developed for cameras 1 and 3. The results are described in the following text. From camera 1, the dipole position and attitude are described by

$$Y = \eta_1$$

$$Z = \zeta_1$$

$\alpha_1$  = slope of image to the Y axis in the YZ plane.

Similarly, from camera 2 the dipole position and attitude is given by

$$X = \xi_2$$

$$Z = \zeta_2$$

$\alpha_2$  = slope of image to the X axis in the XZ plane.

The dipole position with respect to the referenced coordinates is

$$x_p = \frac{a[\alpha\xi_2 - \eta_1(\xi_2 - b)]}{a^2 - (\xi_2 - b)(\eta_1 - b)} \quad (A-13)$$

$$y_p = \frac{a[\alpha\eta_1 - \xi_2(\eta_1 - b)]}{a^2 - (\xi_2 - b)(\eta_1 - b)} \quad (A-14)$$

$$z_p = \frac{(a-b)}{2} \frac{[(a+b)(\xi_1 + \zeta_2) - (\xi_2\xi_1 + \eta_1\zeta_2)]}{a^2 - (\xi_2 - b)(\eta_1 - b)} \quad (A-15)$$

The dipole orientation is obtained from

$$\phi = \tan^{-1} \left\{ \frac{\tan \alpha_2 - \frac{\eta_1 - b}{a} \tan \alpha_1 + \zeta_1/a}{\tan \alpha_1 - \frac{\xi_2 - b}{a} \tan \alpha_2 + \zeta_2/a} \right\} \quad A-16$$

$$\theta = \tan^{-1} \left\{ 1 / \left( \cos \phi (\tan \alpha_2 + \frac{\xi_2 - b}{a} \tan \alpha_2 \tan \phi - \frac{\xi_2}{a} \tan \phi) \right) \right\} \quad (A-17)$$

It should be noted that in the data reduction utilizing cameras 1 and 2, poor accuracy of orientation can occur when the chaff dipole is in a nearly horizontal plane (when crossing the  $Z = 0$  plane). If at this time  $\alpha_1$  and  $\alpha_2$  are equal to or nearly zero, then small errors in reading either  $\alpha_1$  or  $\alpha_2$  result in large changes in  $\phi$  and  $\theta$ . The other orthogonal set of cameras 1 and 3 were incorporated into the test facility to circumvent this problem.

### 3. Calibration

The test facility was fabricated originally with a wire grid system in the XZ and YZ planes. The integrated intensity of light on the grid wires during the particle descent was so large that the grid often obscured the position of the chaff filaments. After determining that there were no noticeable optical anomalies in the lenses (except for parallax), the grid wires were removed in favor of a single pendulum wire with three bead reference marks, each 12 inches apart. The center bead located the zero intercept for the XYZ coordinate system. The three cameras were located in the following positions with respect to the pendulum grid:

**Camera 1**       $X = a = 96$  in.  
                        $Y = b = 16$  in.  
                        $Z = 0.0$  in.

**Camera 2**       $X = b = 16$  in.  
                        $Y = a = 96$  in.  
                        $Z = 0.0$  in.

**Camera 3**       $X = b = 16$  in.  
                        $Y = d = 34.4$  in.  
                        $Z = e = 72$  in.  
                        $\theta_0 = 16.6$  deg.

The calibrated pendulum was used as the tare reference in the following planes:

**Camera 1,**      plane YZ , tare 1 = 12 in.  
**Camera 2,**      plane XZ , tare 2 = 12 in.  
**Camera 3,**      plane X<sub>3</sub>Z<sub>3</sub>, tare 3 = 5,003 in.

4. Computer Program.

All chaff dipole test drops are analyzed in detail using a computer program designated ASTRO. This program is written in FORTRAN 4 and is operated on a CDC 6600 system. The program statements and operation are described in Reference 5.

---

<sup>5</sup> Mihora, D. J., Astro Research Corp., "Photogrammetry of Minute Chaff Elements in a Quiescent Test Chamber," Astro Report No. ARC-TM-320, October 3, 1974.

## APPENDIX B

### AERODYNAMIC DATA REDUCTION PROGRAM

Aerodynamic data reduction is accomplished by computer, using as input dipole time-position-attitude histories and dipole physical characteristics data. The time-position-attitude histories are obtained in card format from the ASTRO data reduction program, Appendix A, which converts the photographic imagery to a motion sequence. The principal aerodynamic data reduction operations are described below.

#### 1. Data Input and Smoothing

Step 1 The raw data produced by ASTRO is read-in and transformed to the inertial coordinates X, Y, Z and the Euler angles  $\psi$  and  $\theta$ , as shown in Figure B-1. A time base is established from the rotating shutter sampling frequency.

Step 2 The X and Y horizontal coordinates are translated to inertial coordinates  $X_o$  and  $Y_o$ , with their origin at approximately the center of the dipole descent spiral, by subtracting constant values (X, Y) from each point of the run. The values ( $\bar{X}$ ,  $\bar{Y}$ ) are determined from initial screening of the data.

Step 3 Rectangular position coordinates  $X_o$ ,  $Y_o$  are converted to polar coordinates R and v as shown in Figure B-2, in preparation for determining  $\dot{X}_o$ ,  $\dot{Y}_o$ ,  $\ddot{X}_o$ , and  $\ddot{Y}_o$ .

$$v = \tan^{-1} (Y_o/X_o) \quad (B-1)$$

$$R = X_o / \cos v \quad (B-2)$$

Step 4 The variables R, v, Z,  $\psi$  and  $\theta$  are locally smoothed using a quadratic least-squares routine with time as the independent variable. Optionally, five or seven values are taken for each smoothing interval, with the mid-point being the point desired. For each smoothing operation a quadratic equation which best "fits" the raw data is obtained, and by differentiation of this equation the first and second time derivatives are obtained.

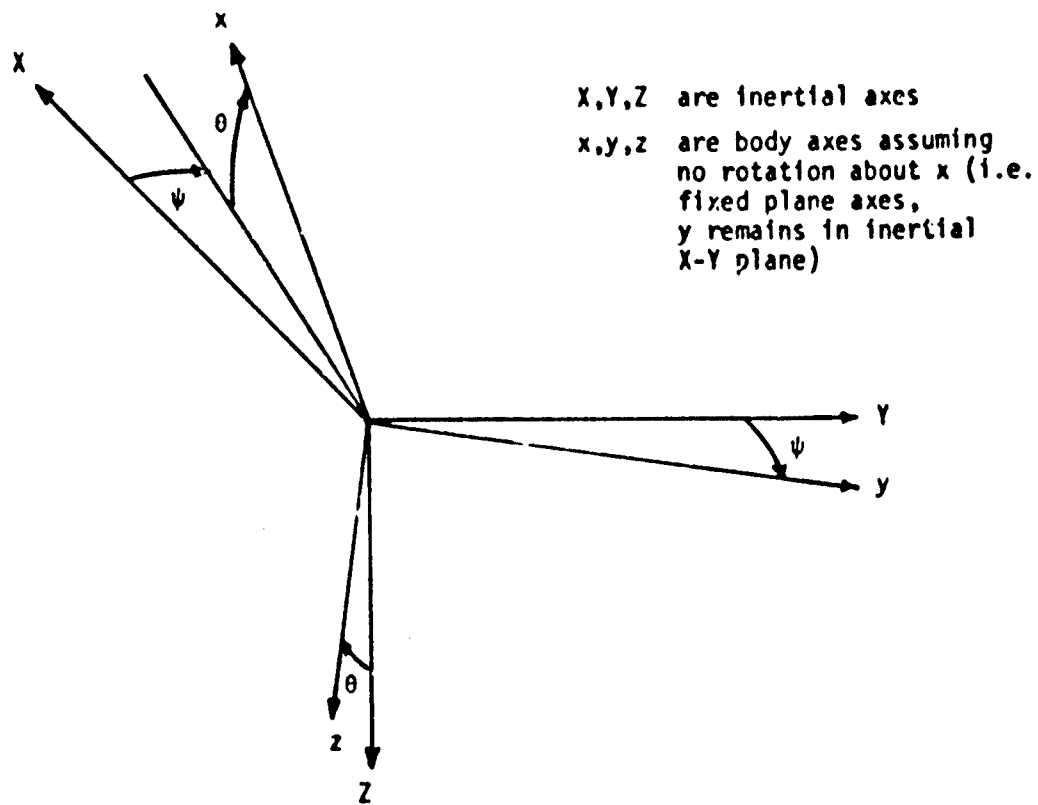


Figure B-1. Euler Angle Notation

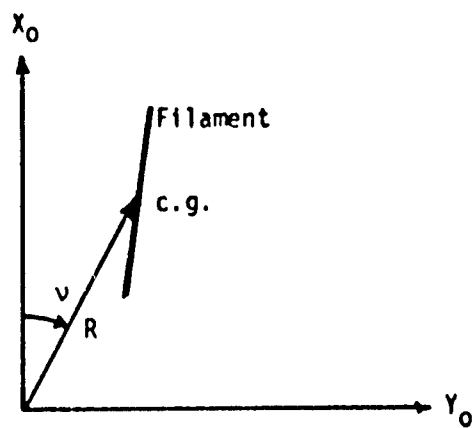


Figure B-2. Polar Coordinates

## 2. Angle of Attack and Flight Path Angles

Step 5 Velocities and accelerations with respect to the Cartesian coordinates ( $\dot{X}_o$ ,  $\dot{Y}_o$ ,  $\ddot{X}_o$ , and  $\ddot{Y}_o$ ) are obtained from the smoothed values of  $R$  and  $v$  and their derivatives, as follows:

$$\dot{X}_o = \dot{R} \cos v - R \dot{v} \sin v \quad (B-3)$$

$$\dot{Y}_o = \dot{R} \sin v - R \dot{v} \cos v \quad (B-4)$$

$$\ddot{X}_o = \ddot{R} \cos v - 2\dot{R} \dot{v} \sin v - R \dot{v}^2 \cos v - R \ddot{v} \sin v \quad (B-5)$$

$$\ddot{Y}_o = \ddot{R} \sin v + 2\dot{R} \dot{v} \cos v - R \dot{v}^2 \sin v + R \ddot{v} \cos v \quad (B-6)$$

Step 6 The inertial velocities and accelerations are transformed to fixed-plane velocities ( $u$ ,  $v$ ,  $w$ ) and accelerations ( $\dot{u}$ ,  $\dot{v}$ ,  $\dot{w}$ ) using the usual Euler transformation matrix (with  $\phi = 0$ ).

$$\begin{bmatrix} u, \dot{u} \\ v, \dot{v} \\ w, \dot{w} \end{bmatrix} = \begin{bmatrix} \cos \psi \cos \theta & \sin \psi \cos \theta & -\sin \theta \\ -\sin \psi & \cos \theta & 0 \\ \cos \psi \sin \theta & \sin \psi \sin \theta & \cos \theta \end{bmatrix} \begin{bmatrix} \dot{X}_o, \ddot{X}_o \\ \dot{Y}_o, \ddot{Y}_o \\ \dot{Z}_o, \ddot{Z}_o \end{bmatrix} \quad (B-7)$$

Step 7 The total angle of attack,  $\hat{\alpha}$ , the angle of attack plane orientation angle,  $\xi$ , the flight heading angle,  $\Psi$ , the descent flight path angle,  $\gamma$ , the orientation angle,  $\bar{\phi}$ , and the total velocity,  $V_T$ , are obtained according to the following equations. The angles are described in Figures B-3 to B-5.

$$\hat{\alpha} = \tan^{-1} \left[ \sqrt{v^2 + w^2} / u \right] \quad (B-8)$$

$$\xi = \tan^{-1} (w/v) \quad (B-9)$$

$$\Psi = \tan^{-1} (\dot{Y}_o / \dot{X}_o) \quad (B-10)$$

$$\gamma = \tan^{-1} \left[ \dot{z} / \sqrt{\dot{X}_o^2 + \dot{Y}_o^2} \right] \quad (B-11)$$

$$\bar{\phi} = \tan^{-1} \left[ (u \cdot w) / (v \cdot V_T) \right] \quad (B-12)$$

$$V_T = \sqrt{u^2 + v^2 + w^2} \quad (B-13)$$

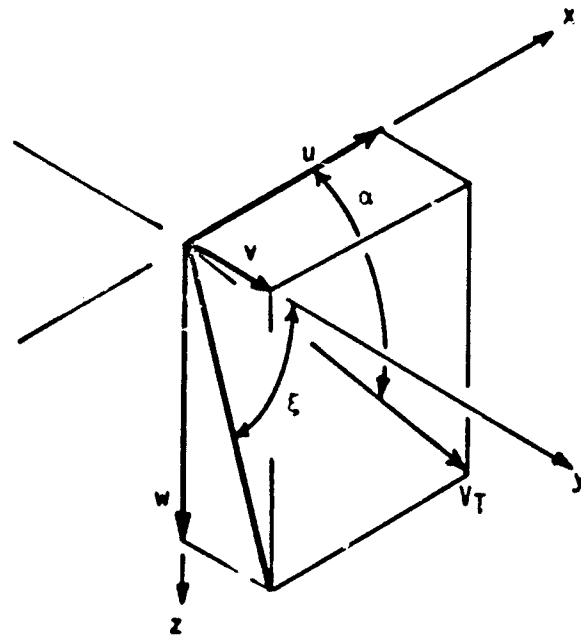


Figure B-3. Angle of Attack Parameters

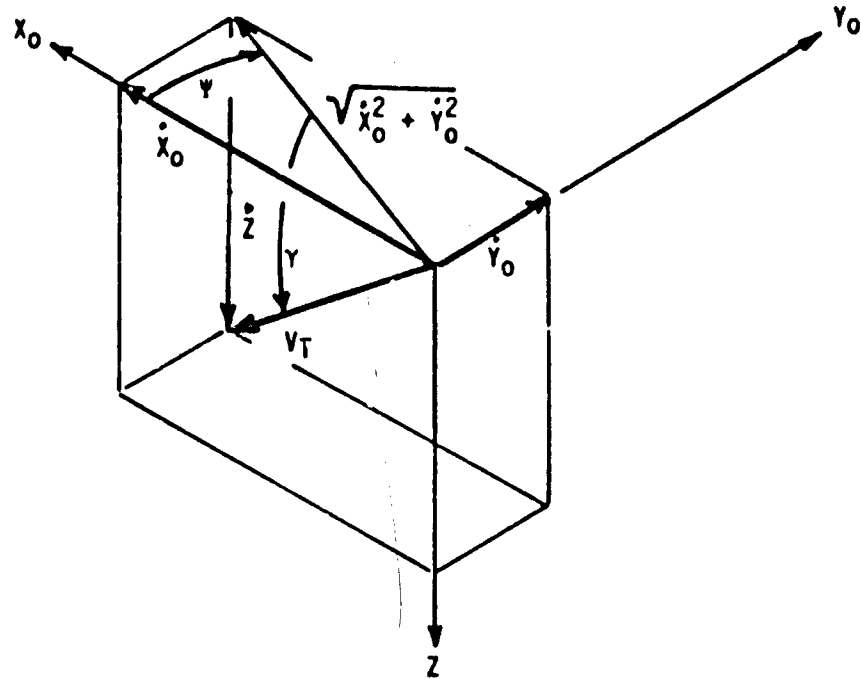


Figure B-4. Flight Path Parameters

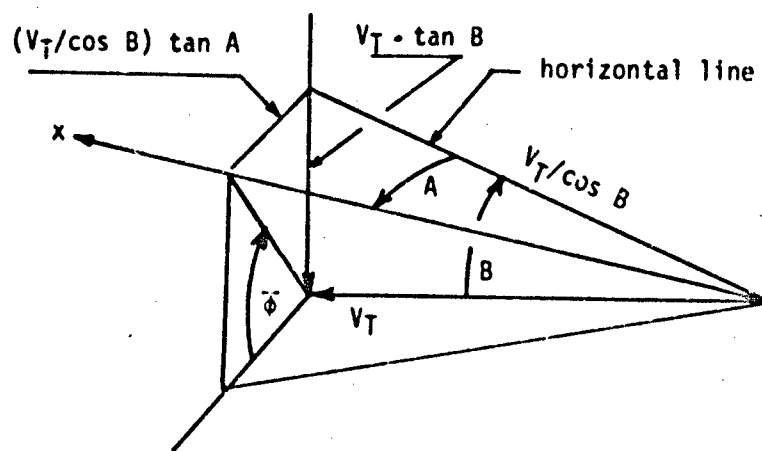
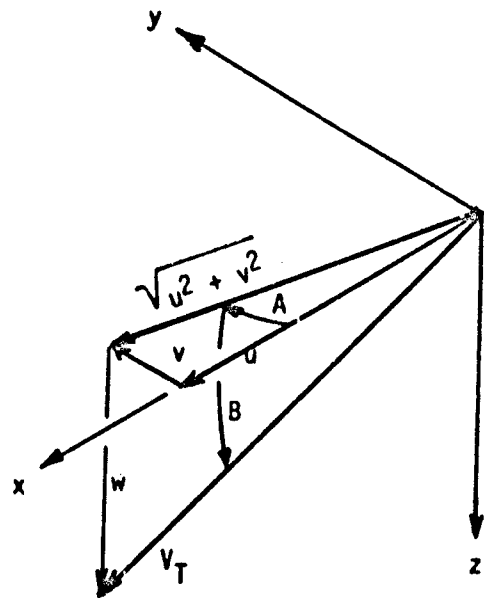


Figure B-5. Definition of Angle  $\phi$

### 3. Aerodynamic Forces

Step 8 The aerodynamic forces in the fixed-plane coordinate system are determined from the following equations:

$$F_x = m(\dot{u} + g \sin \theta) \quad (B-14)$$

$$F_y = m\dot{v} \quad (B-15)$$

$$F_z = m(\dot{w} - g \cos \theta) \quad (B-16)$$

where  $m$  is the dipole mass and  $u, v, w$  are obtained from step (6).

Step 9 Using the angle  $\xi$ , the  $F_y$  and  $F_z$  forces are resolved into force components in the pitch plane (angle of attack plane) denoted by  $F_N$  or normal force and perpendicular to the pitch plane, denoted by  $F_S$  or side force. The forces  $F_N$  and  $F_S$  are then converted to coefficient form in accordance with the following equations. The transformation is described in Figure B-6.

$$C_N = \frac{F_N}{qS} = \frac{1}{qS} \left( -F_y \cos \xi - F_z \sin \xi \right) \quad (B-17)$$

$$C_SF = \frac{F_S}{qS} = \frac{1}{qS} \left( F_y \sin \xi - F_z \cos \xi \right) \quad (B-18)$$

where  $q$  is the dynamic pressure,  $1/2 \rho V_T^2$ , and  $S$  is the aerodynamic reference area, taken to be the dipole maximum projected area, i.e., length times width. The axial force coefficient is obtained similarly

$$C_A = \frac{F_x}{qS} \quad (B-19)$$

### 4. Aerodynamic Moments

Step 10 The fixed-plane moments are given by the following equations, with the intrinsic assumption that the dipole transverse moments of inertia,  $I_y$  and  $I_z$  are equal ( $I_y = I_z = I$ ).

$$M_x = I_x \ddot{p} \quad (B-20)$$

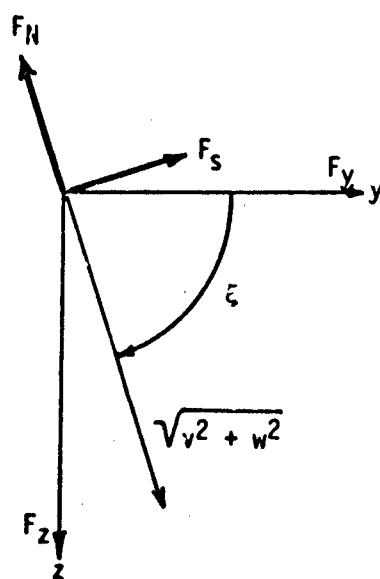


Figure B-6. Force Vector Definitions

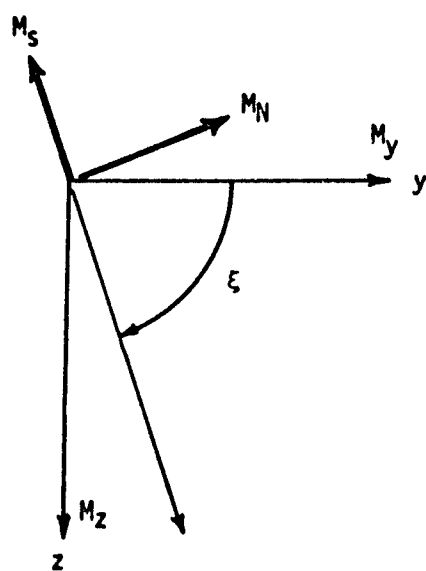


Figure B-7. Moment Vector Definitions

$$M_y = I\dot{q} + pr I_x + r^2 \tan \theta \cdot I \quad (B-21)$$

$$M_z = I\dot{r} - pq I_x - rq \tan \theta \cdot I \quad (B-22)$$

where  $p$ ,  $q$ , and  $r$  are the angular velocities about the  $x$ ,  $y$ , and  $z$  axes, respectively. The angular velocities and accelerations are given below.

$$p = -\dot{\psi} \sin \theta \quad (B-23)$$

$$q = \dot{\theta} \quad (B-24)$$

$$r = \dot{\psi} \cos \theta \quad (B-25)$$

$$\dot{p} = -\ddot{\psi} \sin \theta - \dot{\psi} \dot{\theta} \cos \theta \quad (B-26)$$

$$\dot{q} = \ddot{\theta} \quad (B-27)$$

$$\dot{r} = \ddot{\psi} \cos \theta - \dot{\psi} \dot{\theta} \sin \theta \quad (B-28)$$

Step 11 The moment coefficients corresponding to the pitch plane ( $C_M$ ) and the side moment ( $C_{SM}$ ) are obtained in a manner similar to that used for the force coefficients. The transformations are derived with the aid of Figure B-7.

$$C_M = \frac{M_N}{q S l} = \frac{1}{q S l} [M_y \sin \xi - M_z \cos \xi] \quad (B-29)$$

$$C_{SM} = \frac{M_S}{q S l} = \frac{1}{q S l} [-M_y \cos \xi - M_z \sin \xi] \quad (B-30)$$

$$C_l = \frac{M_x}{q S l} \quad (B-31)$$

The dynamic pressure,  $q$ , and the aerodynamic reference area,  $S$ , are as before;  $l$  is the aerodynamic reference length, taken to be the dipole length.

## APPENDIX C

### CHAFF AERODYNAMIC THEORY

#### 1. Theoretical Aerodynamics of Symmetric Dipole at Low Reynolds Number

The complete motion of bodies with poor aerodynamic shape cannot, within the present state of fluid mechanics, be calculated from the equations of motion for the flow. Therefore, a theoretical treatment of chaff aerodynamic behavior must be restricted to those fluid-dynamic conditions which are amenable to analysis. Thus, we find that the aerodynamic theory is limited to flows for which the viscous effects can be accounted for in a suitably approximate manner, and to body shapes and geometries which are consistent with allowable boundary conditions.

The flow past a small body, such as a chaff element, can usually be described by parameters  $U$ ,  $\ell$ ,  $\mu$ ,  $\rho$ , and  $p_\infty$ , which are the free stream velocity, characteristic length, fluid viscosity, fluid density, and fluid pressure, respectively. By dimensional analysis the number of parameters may be reduced to one, namely, the Reynolds number,  $R_N$ , defined by

$$R_N = \frac{\rho U \ell}{\mu} \quad (C-1)$$

or  $= \frac{U \ell}{\nu}$

where  $\nu$  is the kinematic viscosity.

Before taking up specific cases it is useful to consider the basic characteristics of fluid flow with increasing Reynolds number. There are three principal regimes, which are more or less distinct: 1) steady laminar flow, 2) a regime in which regular time-dependent fluctuations occur in the flow, and 3) a regime in which part of the flow is turbulent. The motion of chaff involves only the first two of these three regimes.

The solution of the exact Navier-Stokes fluid-dynamic equations for the conditions of  $R_N$  tending to zero is due to Stokes. A characteristic property of these solutions is that the inertial forces of the fluid are neglected compared to the viscous and pressure forces. For three-dimensional flow, solutions to the Stokes equations may be found for specified boundary conditions on a solid and at infinity. The Stokes

resistance formula for a sphere of radius,  $a$ , is (see for example, Reference 6).

$$C_D = \frac{D}{1/2 \rho U^2 \pi a^2} = \frac{24}{R_N} \cdot R_N = \frac{24 U a}{\nu} \quad (C-2)$$

Similarly, for a disk one obtains the case of the flow perpendicular to the stream

$$D = 16 \mu U a \quad (C-3)$$

and for the disk edgewise into the flow

$$D = \frac{32}{3} \mu U a \quad (C-4)$$

These results emphasize one of the important features at low Reynolds number: the resistance is relatively insensitive to body orientation.

Although drag predictions using Stoke's equations have been found to be accurate at sufficiently low Reynolds numbers, difference between experimental data and the Stokes predictions become significant when the Reynolds number attains a value near unity. Also, because of the inherent assumptions in the Stokes solution, the Stokes theory cannot determine the resistance of two-dimensional bodies, such as would be representative of long chaff elements.

The so-called Oseen equations are obtained by linearization of the Navier-Stokes equations about zero velocity, and take into account viscosity transport. The Oseen equations are an improvement over the Stokes equations because they provide for approximations which are uniformly valid over the entire flow field at low Reynolds numbers, and because they more accurately represent the physical flow, i.e., a wake in the lee of the body is predicted. The Oseen equations have been used as a starting point for the analysis of the flow around various shapes, as will be discussed in the following sections on Drag and Lift. Here we shall consider only the flow characteristics of two-dimensional circular cylinders of radius,  $a$ . The most comprehensive analysis of this case

---

<sup>6</sup> Lagerstrom, P. A., Laminar Flow Theory, "Theory of Laminar Flows," Vol. IV. High Speed Aerodynamics and Jet Propulsion, Princeton, New Jersey, Princeton University Press, 1964.

is due to S. Tomotika and T. Aoi.<sup>(7)</sup> The drag coefficient is found to be of the form

$$C_D = \frac{8\pi}{R_N} [\epsilon + O(R_N \epsilon)] \quad (C-5)$$

where  $\epsilon$  is the flow perturbation parameter.

Tomotika and Aoi show that by expansion of the stream function the first order prediction for the cylinder drag coefficient is

$$\begin{aligned} C_D &= \frac{8\pi}{R_N} \epsilon = \frac{8\pi}{R_N} \frac{1}{1/2 - \gamma - \ln(R_N/8)}, \quad \gamma = \text{Euler's constant} \\ &= \frac{8\pi}{R_N (2.002 - \ln R_N)} \end{aligned} \quad (C-6)$$

Tomotika and Aoi also show that the drag of the circular cylinder, as determined from Oseen's equations, is composed equally of pressure and frictional drag components.

To appreciate the significance of the resistance formulas for cylinders, it is appropriate to examine the effect of cylinder radius (i.e., chaff size) on both Reynolds number and the drag coefficient. Unfortunately, the relationship between  $C_D$  and the cylinder radius,  $a$ , is given by a transcendental function which must be solved by iteration. Also, to accomplish the solution it is necessary to consider the flight velocity, which for the cylinder in steady vertical descent, is given by

$$U = \frac{\pi a w}{\rho C_D} \quad (C-7)$$

where  $w$  is the chaff weight per unit volume. Combining Equations (C-1), (C-6), and (C-7) we obtain the desired relationships between  $C_D$ ,  $R_N$ , and  $a$ . Figure C-1 shows the resulting variation of  $R_N$  with cylinder radius for values of  $a$  between 0.0001 and 0.1 inches, with  $w = 0.075 - 0.10 \text{ lb/in}^3$  and  $\rho$  and  $\mu$  evaluated for standard sea level

<sup>7</sup> Tomotika, S., and T. Aoi (University of Kyoto, Japan), "The Steady Flow of Viscous Fluid Past a Sphere and Circular Cylinder at Small Reynolds Numbers," Quart. Journ. Mech. and Applied Math., Vol. III, Pt. 2 (1950).

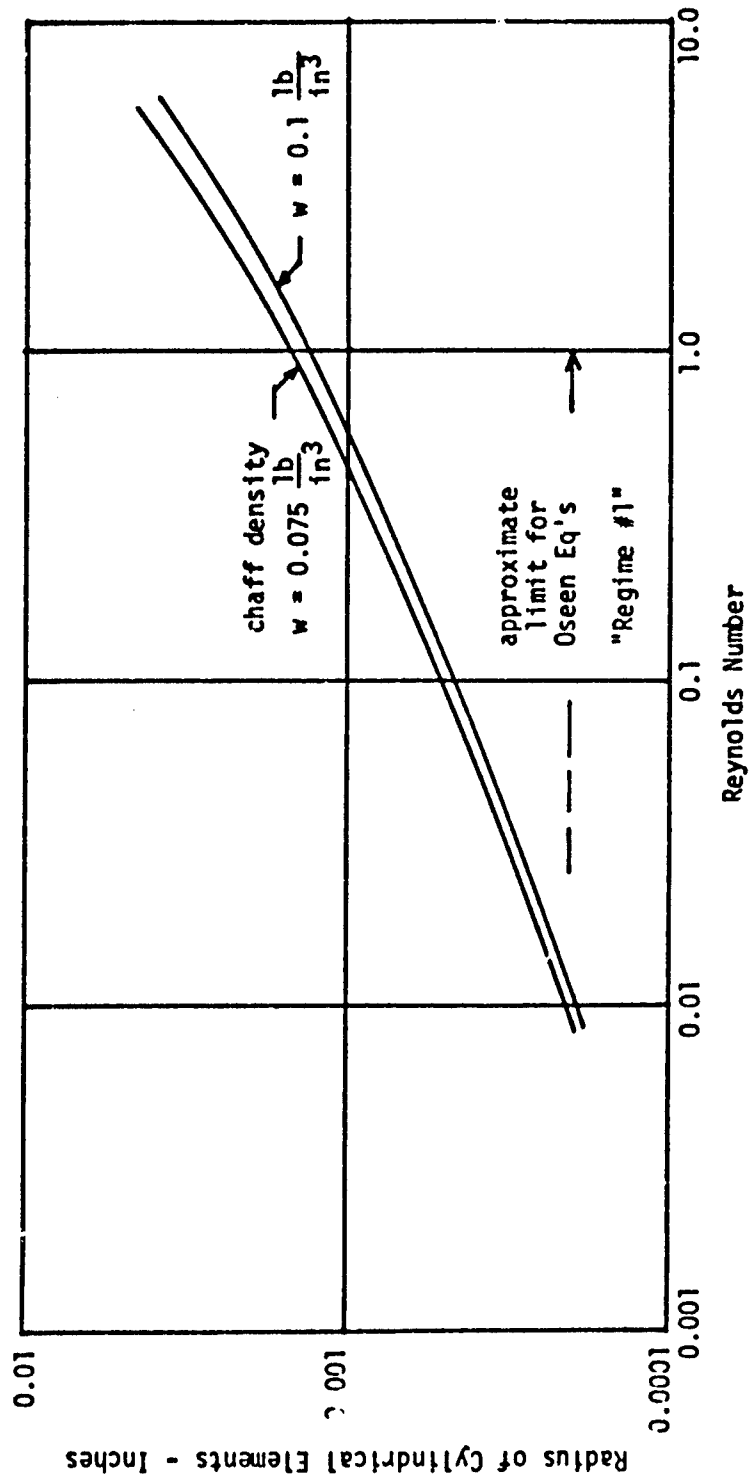


Figure C-1. Effect of Chaff Size on Reynolds Number for Steady Descent (Sea Level Conditions)

conditions. Inspection shows a cylinder radius of about  $1 \times 10^{-3}$  inches (2 mil dipole diameter) corresponds to a Reynolds number of about 0.55 for  $w = 0.1 \text{ lb/in}^3$ . The drag coefficient for this configuration, in accordance with Equation (C-6), is  $C_D = 17.6$ .

Thus, with respect to the principal flow regimes, it is significant that a Reynolds number of unity marks not only the upper extreme of the steady laminar flow regime but also the approximate maximum Reynolds number which will be experienced by a cylindrical dipole with diameter of 0.002 inches or less. A Reynolds number of unity is also the approximate limit for which the Oseen solutions are valid.

At  $R_N = 40$  the previously mentioned second flow regime begins with the appearance of the phenomenon of vortex shedding. Eddies, which at lower values of  $R_N$  had become distended, now periodically breaks away from the cylinder and flow downstream in the wake. The nondimensional shedding frequency is given by the Strouhal number,  $S$ , which is defined as

$$\text{Strouhal number} = S = \frac{nd}{U} \quad (\text{C-8})$$

where  $n$  is the shedding frequency, and  $d$  the cylinder diameter.

The regime  $10 < R_N < 10^4$  is also discussed by Lagerstrom<sup>(6)</sup>. Foil chaff elements, which have a greater characteristic dimension than cylindrical dipoles (i. e., strip width) have typical descent Reynolds numbers of the order of 1.0 - 100.0, and thus can be expected to experience flow conditions representative of the second flow regime. In this range of Reynolds number experimental results described by Lagerstrom show that the total drag coefficient of the cylinder continues to decrease with increasing  $R_N$ , with  $C_{Df}$  approximately equal to  $4/\sqrt{R_N}$ . The ratio of pressure drag to friction drag at  $R_N = 40$  increases to about 1.5, whereas at  $R_N \ll 1$  the ratio is unity. While the above comments apply primarily to cylinders, similar characteristics are noted for bluff shapes such as flat plate, etc. For the flat plate at zero incidence the viscous drag can be evaluated from boundary layer theory. Using the Blasius profile the overall plate drag is  $C_f = 1.328 \sqrt{R_N}$ , which is in good agreement with experiments in the Reynolds number range under discussion.

The foregoing discussion has been concerned primarily with fluid flow and the body drag force. The lift force and moment on an inclined

axisymmetric body in low Reynolds number flow is of considerable interest with respect to chaff dynamics. Unfortunately, solutions for the lift and moment have not received as much attention. Cox<sup>(8)</sup> has found that the Oseen equations do not in general furnish an exactly correct value of the lift force. By the use of the singular perturbation method more accurate functional representations of the aerodynamic forces to  $O(R_N)$  and  $O(R_N^2 \ln R_N)$  are achieved. However, useful solutions for the lift force on two dimensional elliptic cylinders and plates with arbitrary incidence have been obtained from the Oseen equations by Tomotika and Aoi<sup>(9)</sup>, accurate to  $O(R_N)$ . From their results it is found that the drag increases slightly with an increase of either thickness or angle of incidence, and that the lift decreases with thickness ratio while, as a function of incidence, it has a maximum at about 45 degrees.

The aerodynamic moment on an inclined body at low Reynolds number is at most small. Willmarth<sup>(10)</sup>, et al, in their investigation of freely falling disks refers to the work of Gans, who was able to show that for low Reynolds number creeping motion there is no aerodynamic moment produced by fluid pressure on a body that has three mutually perpendicular planes of symmetry. For higher Reynolds numbers no direct computation of the aerodynamic moment as a function of body incidence has been reported; thus, one is led to consider more general analyses of body angular motion.

The angular motion of a solid body in a fluid can be treated from various theoretical viewpoints. The motion of a body in an ideal fluid is

<sup>8</sup> Cox, R. G., "The Steady Motion of a Particle of Arbitrary Shape at Small Reynolds Number," Journal of Fluid Mechanics (1965), Vol. 23, Part 4, pp 625-643.

<sup>9</sup> Tomotika, S. and T. Aoi (Univ. of Kyoto Japan), "The Steady Flow of a Viscous Fluid Past an Elliptic Cylinder and a Flat Plate at Small Reynolds Numbers," Quart. Journ. Mech. and Applied Math., Vol. VI, Pt. 3 (1953).

<sup>10</sup> Willmarth, W. E., et al, "Investigations of the Steady and Unsteady Motion of Freely Falling Disks," Aerospace Research Laboratories Report No. ARL 63-176, October 1963, AD 420 913.

discussed at length by Lamb<sup>(11)</sup>, and reference is made to the earlier work of Kirchhoff, who showed that in the case of the ellipsoid, stable motion is possible only when the direction of motion is along the least axis. For viscous fluids Cox obtains a similar result, showing that the motion of the oblate spheroid (discoid object) is stable only when the flow is parallel to the axis of rotational symmetry and that the prolate spheroid (needlelike object) is stable only when the flow is perpendicular to the axis of rotational symmetry. For creeping flow (i.e., very low Reynolds number) Happel and Brenner<sup>(12)</sup> have applied symmetry considerations to the equations for the hydrodynamic stress tensor, and have determined the motion characteristics of various classes of bodies. The results show that ellipsoids, or bodies of revolution with fore-aft symmetry, which are of uniform density, can attain rotationally free terminal descent for all possible orientations. This has been verified by experimental observation of small spherically isotropic bodies, such as regular polyhedrons, which are noted to fall without rotation.

Happel and Brenner also discuss the motion (and force tensor) of needlelike bodies. The results are of interest because of the applicability to chaff. If the body is a needle-shaped ellipsoid, with the (3) axis denoted as the axis of rotational symmetry, then the translation resistance tensor is

$$K_1 = K_2 = \left[ \frac{8 \pi \phi}{\ln(2\phi) + 1/2} \right] c,$$

$$K_3 = \left[ \frac{4 \pi \phi}{\ln(2\phi) - 1/2} \right] c \quad (C-9)$$

$$\vec{F} = -\mu \vec{K} \vec{U}$$

where  $\phi = l/2c$  and  $l$  is the length of the needle and  $c$  its radius. For large  $l/c$ , (where the constants in Equation (C-9) can be neglected in comparison with the logarithmic terms) the flight path of the needle,

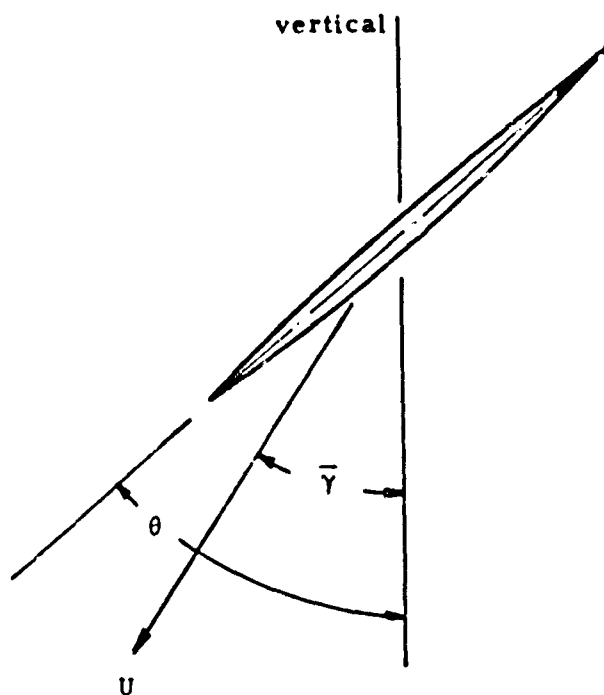
<sup>11</sup> Lamb, Sir Horrace, "Hydrodynamics," Sixth Edition, Dover Publications, New York.

<sup>12</sup> Happel, John, and Howard Brenner, "Low Reynolds Number Hydrodynamics," Prentice-Hall International Series in the Physical and Chemical Engineering Sciences, Prentice-Hall, Inc., Englewood Cliffs, N.J.

descending under the influence of gravity, has been computed. The angle,  $\bar{\gamma}$ , between the vertical and downward direction of motion is

$$\bar{\gamma} = \tan^{-1} \left\{ \frac{-\sin 2\theta}{3 + \cos 2\theta} \right\} \quad (\text{C-10})$$

where  $\theta$  is the orientation of the needle in accordance with the following sketch.



The glide angle,  $\bar{\gamma}$ , is maximum when

$$\theta = \frac{1}{2} \cos^{-1} \left( -\frac{1}{3} \right) = 54.8 \text{ degrees} \quad (\text{C-11})$$

and corresponding direction of movement is given by

$$\bar{\gamma} = \tan^{-1} (0.354) = 19.5 \text{ degrees} \quad (\text{C-12})$$

A more general result can be obtained for the glide angle,  $\bar{\gamma}$ , using the ratio of the transverse and axial resistance factors. Thus, if

we define an axial resistance factor

$$K_3 = \frac{-F_x}{\mu U_3}$$

and transverse resistance factor

$$K_{1,2} = \frac{-F_N}{\mu U_{1,2}}$$

and their ratio as

$$\bar{K} = \frac{K_{1,2}}{K_3}$$

we obtain

$$\bar{\gamma} = \tan^{-1} \left\{ \frac{-\sin 2\theta}{\left( \frac{1+K}{1-K} \right) + \cos 2\theta} \right\} \quad (C-13)$$

$$\text{which is maximum for } \theta = \frac{1}{2} \cos^{-1} \left\{ - \left( \frac{1-\bar{K}}{1+\bar{K}} \right) \right\}$$

## 2. Aerodynamic Forces Acting Upon a Symmetric Dipole

Cylindrical Elements - Flow Perpendicular to Axis For cylindrical dipole with radii less than 0.001 inches, the Reynolds number in steady descent will be less than unity, and the drag coefficient as determined from solution of the Oseen equations, i.e., Equation (C-6), is applicable when the chaff element has near horizontal orientation. Since this result is two dimensional, a correlation should be applied for finite length cylinders. Although no theory is available for short cylinders, we can use the results of Burger as presented by Happel and Brenner for estimating the effect of the slenderness ratio. Burger's drag relation for a cylinder moving perpendicular to its axis is

$$F = \frac{8\pi\mu U_a}{\ln(2a/b) + 0.5} \quad (C-14)$$

where  $2a$  is the cylinder length and  $b$  the radius. The drag coefficient based on area  $4ab$  and  $R_N = \frac{2bU}{v}$  is

$$C_D = \frac{8 \pi}{R_N} \left( \frac{1}{\ln(2a/b) + 0.5} \right) \quad (C-15)$$

As an example, the effect of chaff length on drag is determined using Equation (C-15). Consider the ratio of drag coefficient for 1-mil diameter chaff of lengths 0.25 and 2.00 inches. From Equation (C-15) we obtain the result

$$\frac{C_D(0.25 \text{ length})}{C_D(2.00 \text{ length})} = 1.35$$

Cylindrical Elements - Flow Parallel to Axis The determination of the drag of cylindrical chaff elements in axial flow (or at incidence) requires methods which differ from those used for calculation of the cross flow.

In the case of needlelike bodies in axial flow, the boundary layer near the rear of the body is large compared to the body radius, while near the nose of the boundary layer thickness is small. Glauert & Lighthill<sup>(13)</sup> suggest a mixed solution which provides valid values of the skin friction for all values of the parameter  $\nu x/Ua^2$ , where  $x$  is the distance from the front of the cylinder. The total momentum defect (which is proportional to the drag coefficient) is presented in graphical form in Figure C-2.

A more approximate solution for the axial drag, due to Burger, is presented by Brenner;

$$F = \frac{4 \pi \mu Ua}{\ln(2a/b) - 0.72} \quad (C-16)$$

where the cylinder length is  $2a$  and the radius is  $b$ . The drag coefficient, based on area  $4ab$ , and  $R_N = U2a/\nu$  is

$$C_D = \frac{4 \pi}{R_N} \left( \frac{a/b}{\ln(2a/b) - 0.72} \right) \quad (C-17)$$

---

<sup>13</sup> Glauert, M. B. and M. J. Lighthill F. R. S., "The Axisymmetric Boundary Layer on a Long Thin Cylinder," Proceedings of Royal Society of London, Series A. Mathematical and Physical Sciences, 12 July 1955.

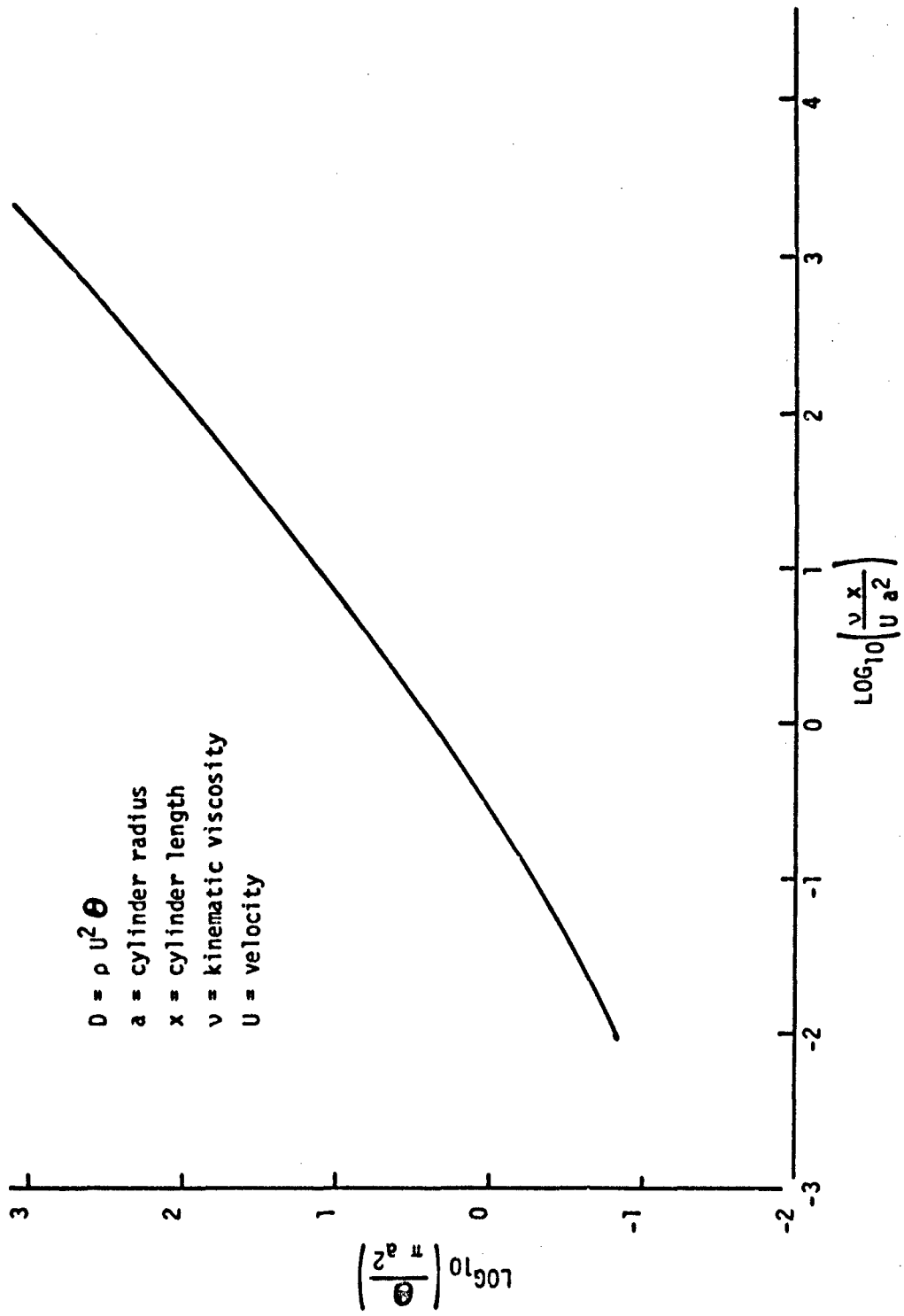


Figure C-2. Drag Parameters of Long Cylinder in Axial Flow (Theory of Glauert and Lighthill)

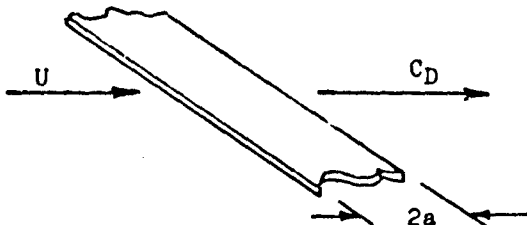
To compare Glauert's and Burger's results, drag coefficients have been computed for a 1-mill-diameter dipole 2-inches in length, descending in vertical orientation at  $U = 1 \text{ ft/sec}$  at sea level. We obtain

$$\text{Glauert's method} \quad C_D = 7.50$$

$$\text{Burger's method} \quad C_D = 3.14$$

Apparently, at  $U = 1 \text{ ft/sec}$  Burger's approximate solution based on creeping flow is unreliable.

Strip Elements - Flow Perpendicular to Axis The drag of a two-dimensional plate (or elliptic cylinder) with axis perpendicular to the flow has been determined by Imai<sup>(14)</sup>, using a general solution of Oseen's equation involving successive approximations in powers of the Reynolds number. The drag of the plate at zero incidence is

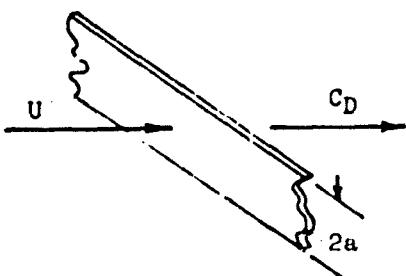


$$C_D = \frac{8 \pi}{R_N (S + 1)} \left[ 1 - \frac{R_N^2}{128} \left( \frac{1}{S} - \frac{5}{12} \frac{1}{S+1} \right) \right] \quad (\text{C-18})$$

while for 90 degrees incidence

---

<sup>14</sup> Imai, Isao, (Univ. of Tokyo, Japan), "A New Method of Solving Oseen's Equations and Its Application to the Flow Past an Inclined Elliptic Cylinder," Proceedings of Royal Society, A 224 (1954), pg. 141.



$$C_D = \frac{8\pi}{R_N S} \left[ 1 - \frac{R_N^2}{128} \left( \bar{S} + 1 + \frac{1}{4\bar{S}} \right) \right] \quad (C-19)$$

where

$$\bar{S} = \ln \left[ \frac{16}{R_N} \right] - \gamma$$

$$\gamma = 0.5772 \dots$$

and  $R_N$  is based on the width of the plate,  $2a$ .

Lift (Normal Force) For strip chaff there are two sources of aerodynamic lift; 1) the inclination of the longitudinal axis, and 2) the orientation of the plate about its axis. These are distinguished in Figure C-3.

A theoretical solution for the effect of  $\alpha$  on the lift and drag of the strip type element is not presently available. For  $\alpha = \pi/2$ , i.e., with pure cross flow, Imai gives both  $C_L$  and  $C_D$  for the two-dimensional flat plate as a function of  $\phi$ . The resulting variations of  $C_L$  and  $C_D$  with  $\phi$  for three representative Reynolds numbers are shown in Figure C-4. The variation of  $C_L$  with  $\phi$  is seen to be closely approximated by  $C_L = (C_L)_{MAX} \sin 2\phi$ .

For  $\alpha \neq \pi/2$  cross flow theory can be invoked. The normal force can be computed from the cross flow component,  $U_N$ , and the cross flow Reynolds number. The axial force can be computed from either the skin friction, or from the Stokes solution for the equivalent cylinder.

As a first approximation to the cross flow, we can take the leading terms in Imai's formulas and obtain the total normal force

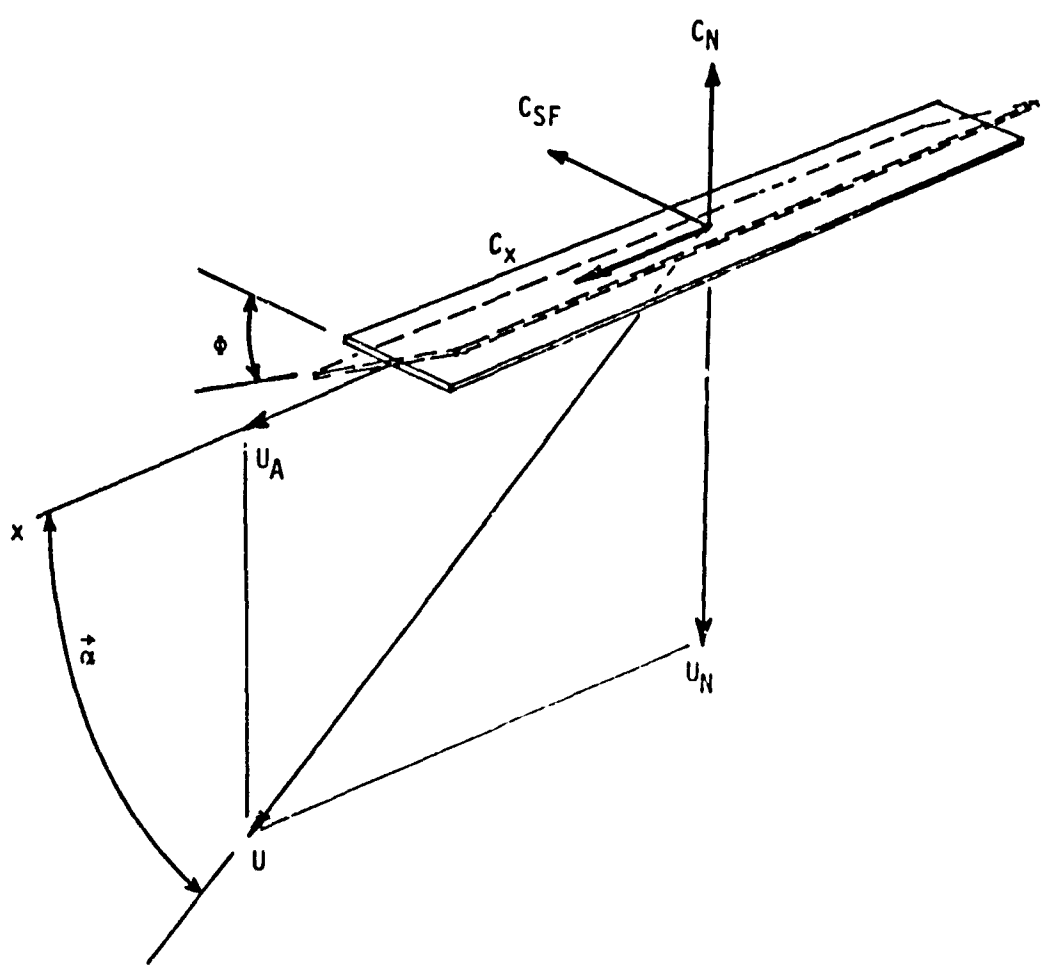


Figure C-3. Aerodynamic Force Notation for Foil-Type Dipole

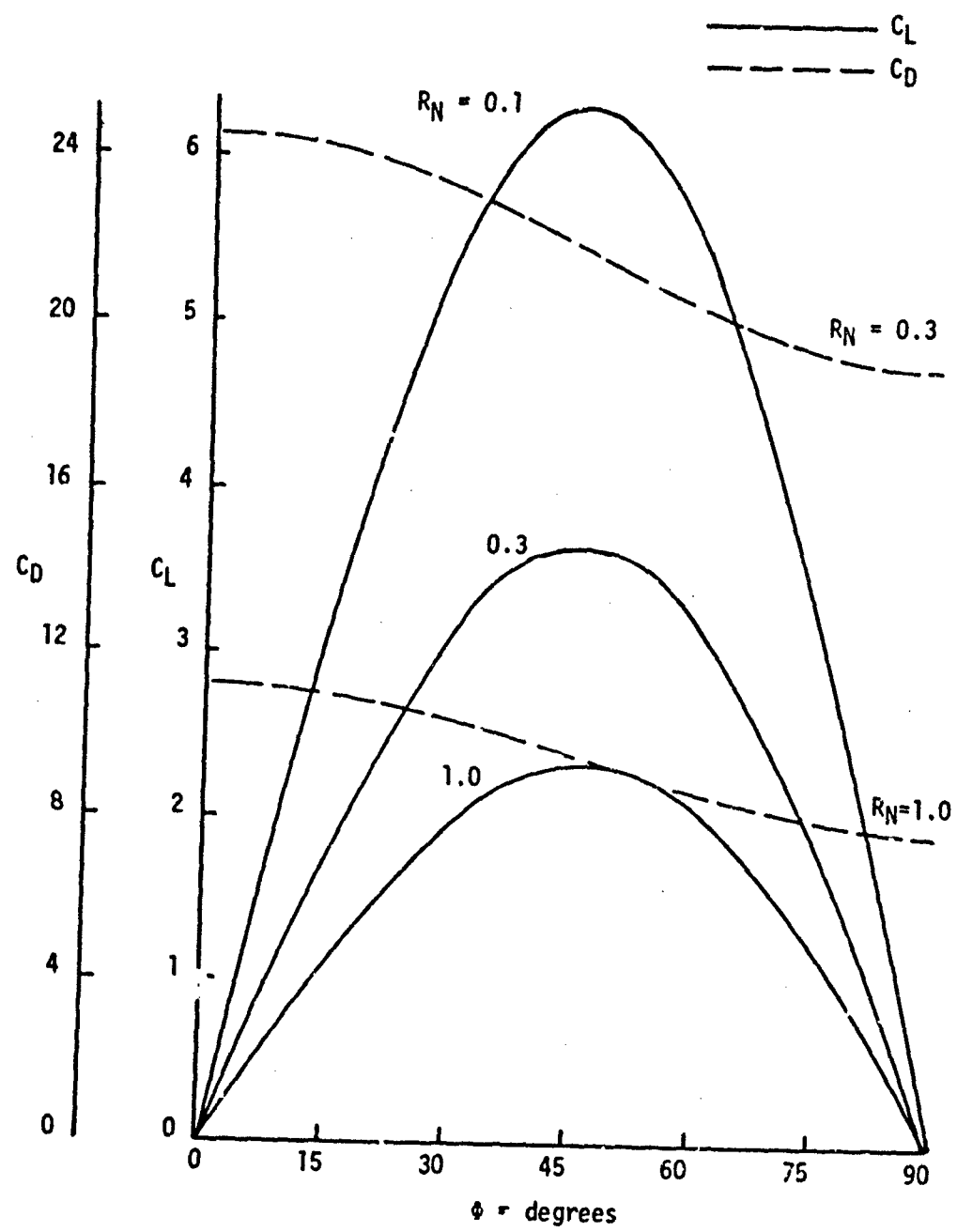


Figure C-4. Effect of Chaff Orientation Parameter  $\phi$  on Section Lift and Drag Coefficients (2-Dimensional Flat Plate Theory)

coefficient as

$$C_N(\alpha, \phi) = \left( \frac{16\pi}{R_N} \right) \left( \frac{2\bar{S}-1}{4\bar{S}^2} \right) \sin \alpha + \left( \frac{16\pi}{R_N} \right) \left( \frac{1}{4\bar{S}^2} \right) \sin \dot{\alpha} \cos 2\phi \quad (C-20)$$

where  $\bar{S} = \ln \left[ \frac{16}{R_N} \right] - \gamma$ ,  $\gamma = .5772$

$$R_N = \rho \frac{U c}{\mu}$$

c = width of strip

U = total velocity.

Thus, the normal force consists of one component which is independent of  $\phi$ , and a second component which depends upon both  $\dot{\alpha}$  and  $\phi$ .

Side Force In the case of a foil dipole there exists a side force as well as a normal force and axial force (see Figure C-3). The side force coefficient,  $C_{SF}$ , is derived in a manner similar to that used for the normal force, with the result

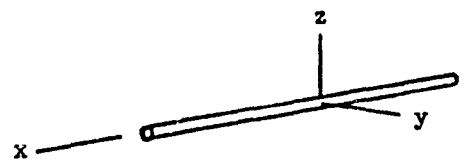
$$C_{SF}(\dot{\alpha}, \phi) = \left( \frac{16\pi}{R_N} \right) \left( \frac{1}{4\bar{S}^2} \right) \sin \alpha \cdot \sin 2\phi \quad (C-21)$$

This force is seen to be identical in magnitude to the  $\phi$  dependent normal force, but with  $\pi/2$  difference in phase.

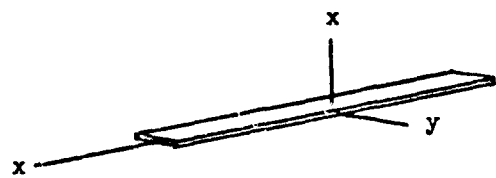
### 3. Aerodynamic Characteristics of an Asymmetric Dipole

Dipole asymmetries provide the driving force for all spiral and glide-type motions. Asymmetries may be either inertial or geometric in form. Several types of asymmetry will usually exist simultaneously, however, the magnitude of each type of asymmetry will vary widely between different dipoles.

All asymmetries are referenced to a basic dipole configuration which is assumed to have at least three planes of mirror symmetry. In addition, it is assumed that all glass dipoles have basic axial symmetry. Representative symmetric dipoles are sketched on the following page.

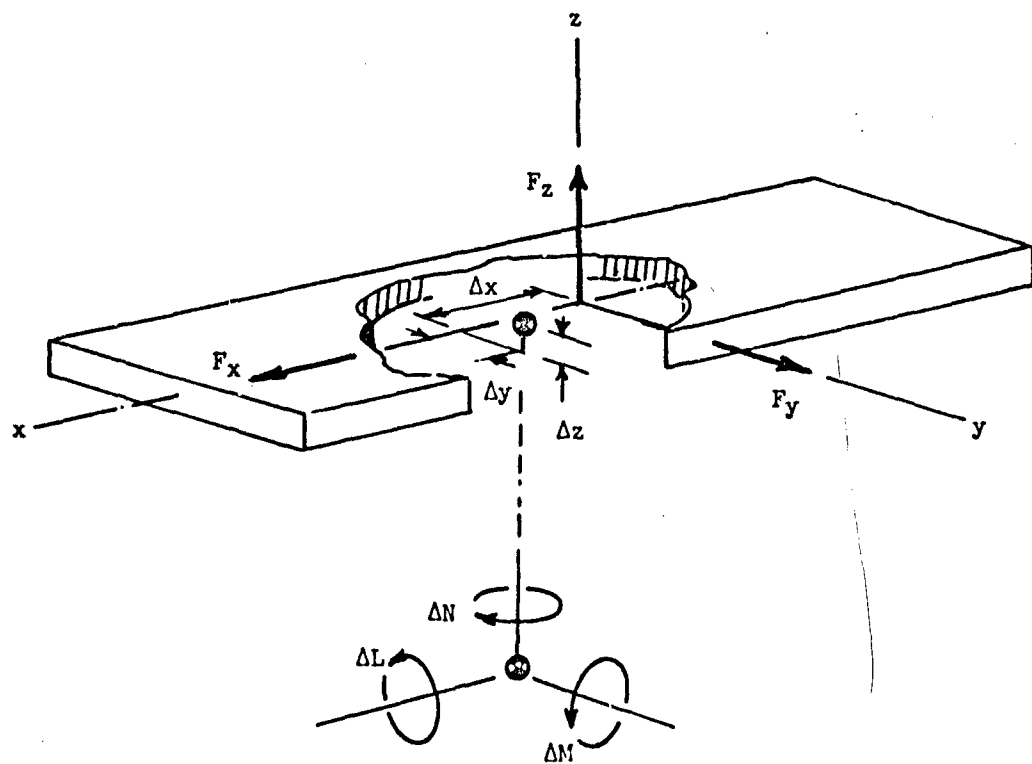


a) Glass-Type Dipole  
(axially symmetric  
about x )



b) Foil-Type Dipole  
(mirror symmetric)

Center-of-Mass Offset The most elementary chaff asymmetry is a displacement of the mass center from the origin of the axes of symmetry (see sketch below).



This type of mass asymmetry results in aerodynamic moments about the center-of-mass of the form

$$\begin{aligned}\Delta L &= -F_z \Delta y + F_y \Delta z \\ \Delta M &= F_z \Delta x - F_x \Delta z \\ \Delta N &= -F_z \Delta x + F_x \Delta y\end{aligned}\quad (C-22)$$

where  $F_x$ ,  $F_y$ ,  $F_z$  are the aerodynamic force components, which are unaffected by mass asymmetry.

Longitudinal Bending Longitudinal bending is a significant source of aerodynamic moment when the dipole axis is closely aligned with the direction of flight. This is because the local viscous force vectors do not, in general, pass through the center of mass. A dipole with longitudinal bend of constant bend radius,  $R$ , can be depicted schematically as in Figure C-5). The moment can be expressed in the form

$$dM = F_T [(\delta - R) \cos \theta + R] ds \quad (C-23)$$

The variable  $F_T$  is the viscous force per unit length and can be evaluated as a function of  $s$  by the methods of Reference 13). For preliminary analysis the average viscous force can be used.

$$F_T = \frac{F_{viscous}}{\ell} = \frac{F_v}{2a} \quad (C-24)$$

Substituting Equation (C-24) into Equation (C-23), letting  $ds = R d\theta$ , and integrating, we obtain

$$M = F_v R \left[ 1 + \left( \frac{\delta - R}{a} \right) \sin \left( \frac{a}{R} \right) \right] \quad (C-25)$$

or in coefficient form

$$C_M = C_{D_{axial}} \left( \frac{R}{2a} \right) \left[ 1 + \left( \frac{\delta - R}{a} \right) \sin \left( \frac{a}{R} \right) \right] \quad (C-26)$$

If the dipole has uniform mass density and if  $R \gg a$  the center-of-mass offset is given by

$$\delta = \frac{a^2}{6R} \quad (C-27)$$

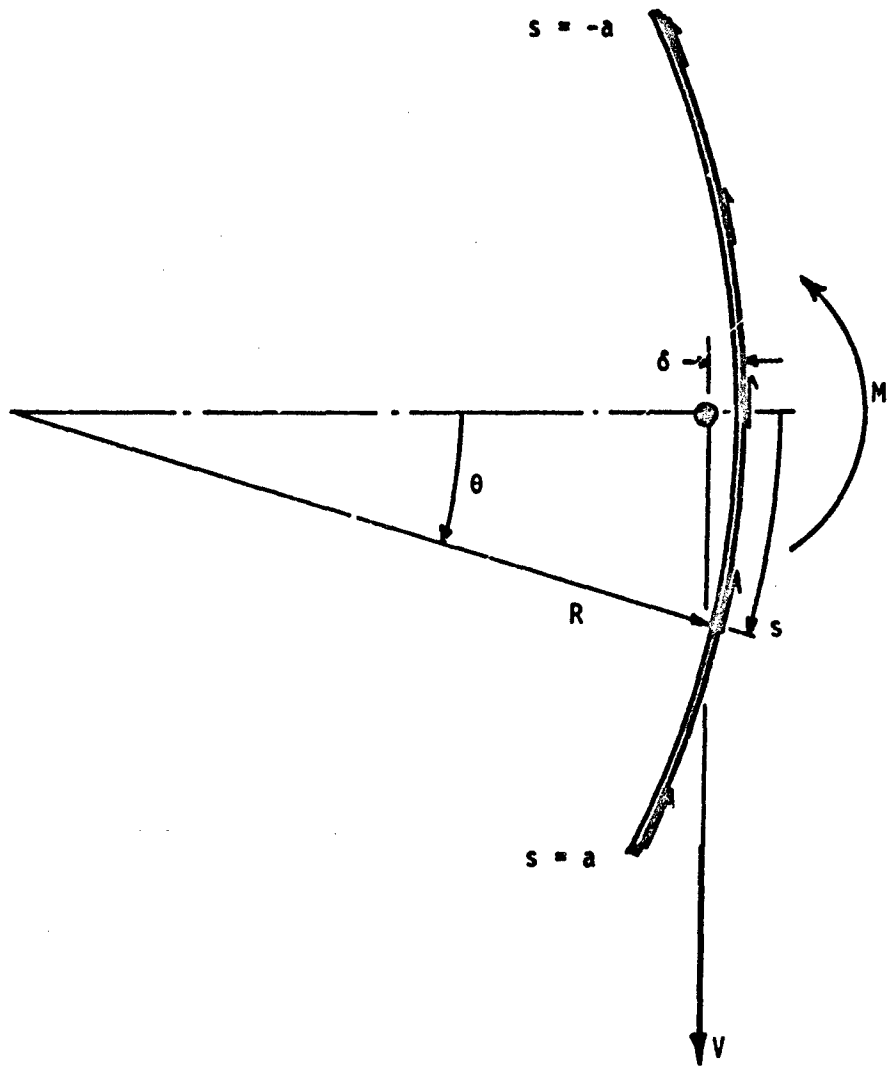


Figure C-5. Schematic of Aerodynamic Moment Due to Axial Viscous Force (Dipole with Longitudinal Bend)

Thus

$$C_M = C_{D_{\text{axial}}} \left( \frac{R}{2a} \right) \left[ 1 + \left( \frac{a}{6R} - \frac{R}{a} \right) \sin \frac{a}{R} \right] \quad (\text{C-28})$$

A second source of aerodynamic moment due to longitudinal bend occurs at finite angles of attack and is due to the variation in normal force along the element. (See Figure C-6).

The elemental moment due to  $C_N$  can be expressed as

$$dC_M \approx \frac{[C_N(\alpha)]}{2a} \left( \frac{s}{2a} \right) ds \quad (\text{C-29})$$

Assuming that  $[C_N(\alpha)]$  is of the form

$$[C_N(\alpha)] = \frac{\bar{C}_N}{V} \sin \alpha, \quad (\text{C-30})$$

noting that  $\alpha(s) = \alpha_R - \theta$ , and letting  $s = R\theta$  we can obtain

$$\begin{aligned} C_M &= \frac{\bar{C}_N}{4Va^2} \int_{-a}^a \left[ s \sin \left( \alpha_R - \frac{s}{R} \right) \right] ds \\ &= -\frac{\bar{C}_N}{2V} \left( \frac{R}{a} \right)^2 \left[ \sin(a/R) - (a/R) \cos(a/R) \right] \cos \alpha_R \end{aligned} \quad (\text{C-31})$$

The  $C_M$  moment due to the normal force variation (Equation (C-31)) is seen to oppose that due to the axial viscous force (Equation (C-28)).

Transverse Bend, Twist, and Kink Examples of transverse bend, twist, and kink are depicted in Figure C-7.

Since these shapes are not amenable to direct analysis, the functional relationship between the aerodynamic forces and moments and the dipole attitude and configuration geometry must be established largely from symmetry considerations. To this end it is useful to establish for the symmetric dipole force and moment coefficients the dependence upon the aerodynamic variables  $\alpha$  and  $\phi$  (see Figure C-3). This dependency is noted in the upper half of Table C-1. For the symmetric dipole the

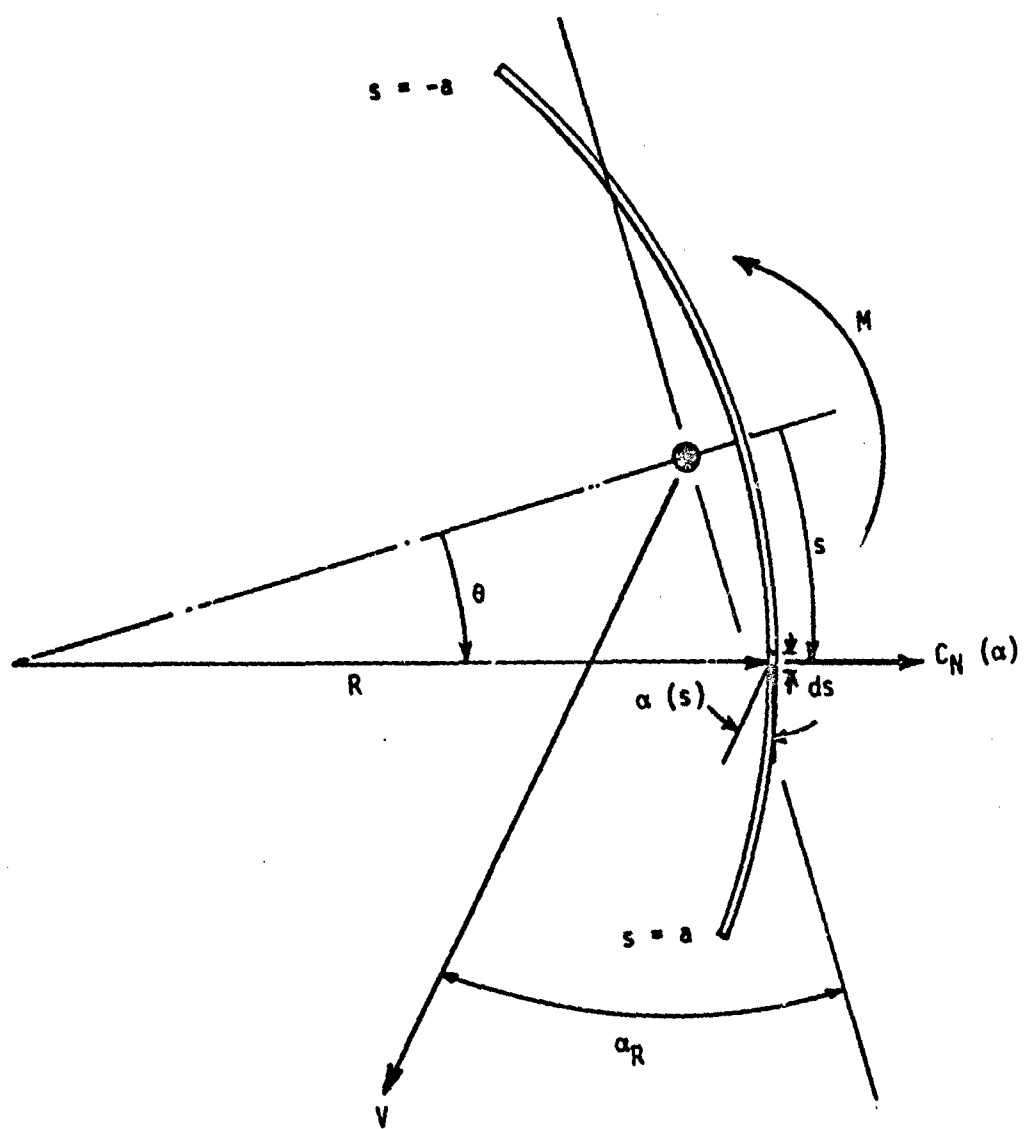
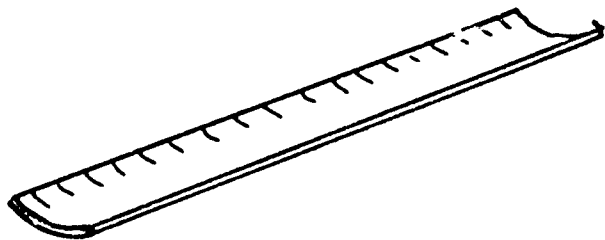
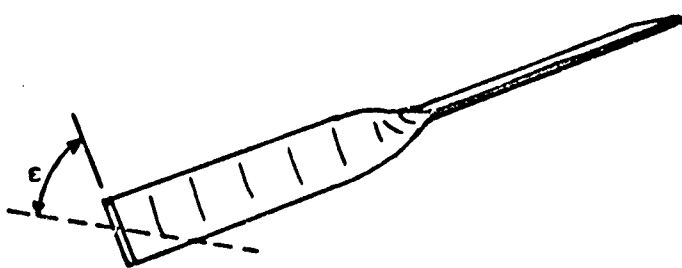


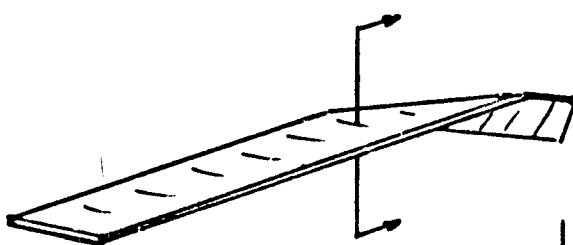
Figure C-6. Schematic of Aerodynamic Moment Due to Normal Force  
(Dipole with Longitudinal Bend)



a) transverse bend



b) twist



c) kink

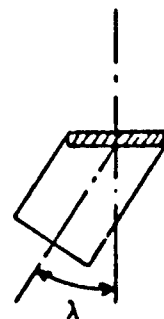


Figure C-7. Asymmetric Dipole Configurations

Table C-1. CHARACTERISTIC FUNCTIONAL DEPENDENCE OF DIPOLE AERODYNAMIC COEFFICIENTS ON  $\alpha$  AND  $\phi$

Dipole Configuration	Aerodynamic Coefficients					
	$C_A = -C_X$	$C_N$	$C_S F$	$C_M$	$C_{SM}$	$C_L$
Symmetric dipole	$k_0 \cos \alpha$	$k_1 \sin \hat{\alpha}$ + $k_2 \sin \hat{\alpha} \cos 2\phi$	$k_2 \sin \hat{\alpha} \sin 2\phi$	$K_0 \sin 2\hat{\alpha}$ + $K_1 \sin 2\hat{\alpha} \cos 2\phi$	$K_2 \sin 2\hat{\alpha} \sin 2\phi$	$K_3 \sin \hat{\alpha} \sin 2\phi$
Asymmetric dipole	—	—	—	—	—	—
longitudinal bend (effect of axial force)	—	—	—	$K_4 \cos \hat{\alpha} \cos \theta$	$K_4 \cos \hat{\alpha} \sin \theta$	—
transverse (or V) bend	—	$k_3 \sin \hat{\alpha} \cos \theta$	$k_3 \sin \hat{\alpha} \sin \theta$	—	$K_5 \sin \hat{\alpha} \sin \theta$	$K_6 \sin \hat{\alpha} \sin \theta$
twist (small $\epsilon$ ), kink	—	$[k_5(\epsilon)] \sin \hat{\alpha} \cos 2\phi$ $[k_5(\hat{\alpha})] \cos(\theta + \lambda)$	$[k_5(\epsilon)] \sin \hat{\alpha} \sin 2\phi$ $[k_5(\hat{\alpha})] \sin(\theta + \lambda)$	$[K_7(\epsilon)] \sin \hat{\alpha} \sin 2\phi$ $[K_7(\hat{\alpha})] \cos(\theta + \lambda)$	$[K_7(\epsilon)] \sin \hat{\alpha} \cos 2\phi$ $[K_7(\hat{\alpha})] \sin(\theta + \lambda)$	$K_8 \cos \hat{\alpha}$ $+ [K_{11}(\hat{\alpha})] \sin(\theta + \lambda)$

force coefficient relationships for  $C_N$  and  $C_{SF}$  are consistent with cross-flow theory (Equations (C-20) and (C-21)), while the moment coefficient dependence upon  $\dot{\alpha}$  is assumed apriori. The harmonic coefficients for both the symmetric and unsymmetric dipoles are assigned arbitrary identities;  $k_i$  denoting the force coefficients and  $K_j$  denoting the moment coefficients.

For asymmetric dipoles the functional dependence of the forces and moments on  $\dot{\alpha}$  and  $\dot{\Phi}$  is shown in the lower portion of Table C-1, where the completeness longitudinal as well as transverse bend is included. The formulas for transverse bend and kink are postulated from both cross-flow considerations and the nature of the configurational asymmetry. In the case of twist with small deflection  $\epsilon$ , the functional dependence is derived analytically from the force and moment definitions for the symmetric element.

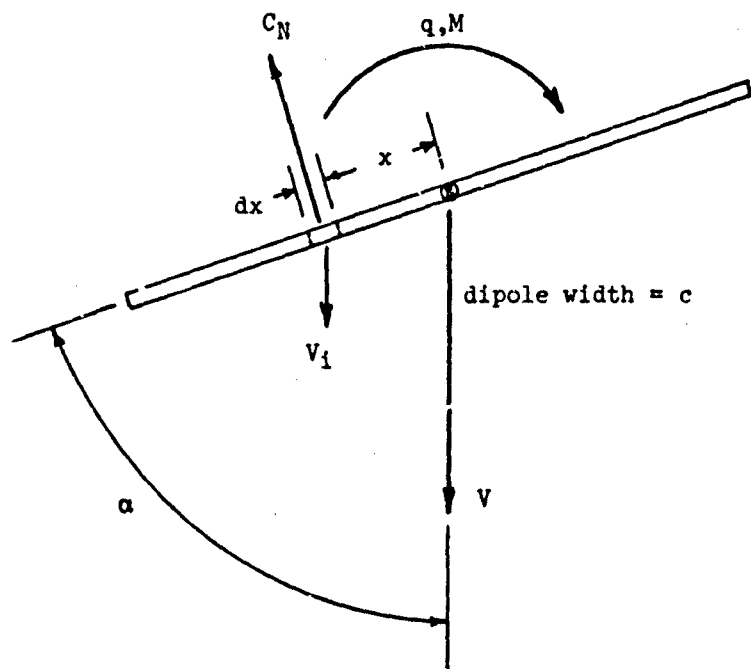
The  $K_j$ 's in Table C-1 are, in general, either positive or negative; thus, if one or more moments due to asymmetry exist for each degree of freedom, it is possible for  $\dot{\alpha}$  and  $\dot{\Phi}$  to have trim values which do not correspond to those for the symmetric dipole. Also, the moment due to asymmetry can result in steady-state angular motions, wherein the moment balance is completed by the inertial and damping moment contributions.

#### 4. Aerodynamic Damping

Estimated values for the aerodynamic damping derivatives corresponding to the plane of total angle of attack and plane of the side moment are required for analysis and prediction of dipole angular motion. The damping moment contributions are particularly significant in the case of chaff configurations, not only because the damping moments tend to be large as a result of the viscous forces, but also because the corresponding static moments tend to be quite small.

Because of the large length to width ratio of the characteristic dipole, it is appropriate to use strip theory for determination of the local cross force along a dipole. It is assumed that the local force has the same dependency upon flow orientation and velocity as does the complete element.

Angle of Attack Plane The following sketch depicts the local flow and force on a dipole undergoing rotation in the angle of attack plane.



It is assumed that the local normal force coefficient for a nominal range of Reynolds numbers can be expressed as

$$C_N(\alpha, V) = \frac{\bar{C}_N}{V_i} \sin \alpha \quad (C-32)$$

where  $\bar{C}_N$  is a constant corresponding to the normal force on a complete dipole.

The local damping moment,  $M(q)$ , is now given by

$$dM = \left( \frac{\bar{C}_N}{V_i} \sin \alpha \right) \frac{1}{2} \rho V_i^2 c x dx \quad (C-33)$$

where  $V_i = V - qx \sin \alpha$

Thus the total damping moment is obtained from

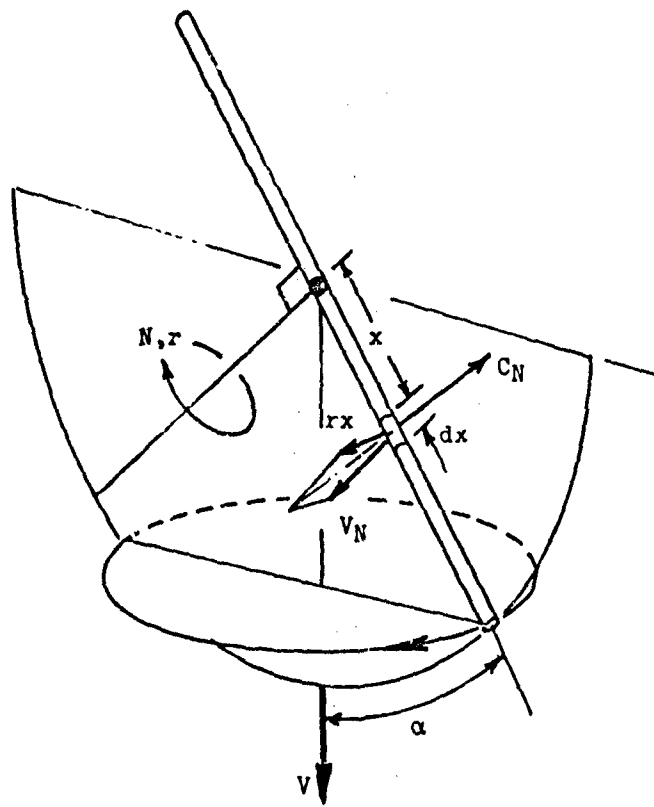
$$M = \frac{\bar{C}_N \rho c}{2} \sin \alpha \int_{-\ell/2}^{\ell/2} (v - qx \sin \alpha) x dx$$
$$M = \frac{\bar{C}_N \rho c \ell^3 q \sin^2 \alpha}{24} \quad (C-34)$$

In coefficient form (using characteristic length,  $\ell$ , and aerodynamic reference area  $S = c\ell$ ) the conventional damping derivative is

$$C_{m_q} = \frac{\partial C_M}{\partial \left( \frac{q\ell}{2V} \right)}$$
$$C_{m_q} = \frac{\bar{C}_N \sin^2 \alpha}{6 V} \quad (C-35)$$

The damping derivative has the same inverse dependence upon velocity as do the force coefficients.

Side Moment Plane For the side moment plane the local cross force and velocity components are depicted on the following page.



The local damping moment  $N(r)$  is given by the differential

$$dN = [C_N(\alpha, v) \sin \xi] \frac{1}{2} \rho v_i^2 c x dx \quad (C-36)$$

where

$$\sin \xi = \frac{rx}{v_N}$$

$$v_N = v \sin \alpha$$

$$v_i = \sqrt{v^2 + (rx)^2}$$

Again using the relation

$$C_N(\alpha) = \frac{\bar{C}_N}{v_i} \sin \alpha$$

and letting  $V_i = V$  (which is a reasonable approximation if  $r$  is small and  $\alpha$  does not approach zero) the differential moment can be written

$$dN = \frac{\bar{C}_N \rho c r x^2 dx}{2} \quad (C-37)$$

After integrating and defining the damping derivative for the side moment plane,  $C_{n_r}$ , as

$$C_{n_r} = \frac{\partial C_n}{\partial \left( \frac{r \ell}{\partial V} \right)}$$

where

$$C_n = \frac{N}{1/2 \rho V^2 c \ell^2}$$

the following solution for the damping derivative is finally obtained

$$C_{n_r} = \frac{\bar{C}_N}{6V} \quad (C-38)$$

## 5. Spiral Dynamics

The characteristic spiral mode of a chaff dipole results from both an unsymmetric trim angle of attack,  $\vec{\alpha}_T$ , (i.e.,  $\vec{\alpha}_T \neq 0, \pi/2, \dots$ ) and an unbalanced static side moment,  $SM$ , which causes continuous azimuthal rotation,  $\dot{\psi}$ . A heuristic model of the aerodynamic forces is depicted in Figure C-8 along with the pertinent motion parameters. The model is appropriate for those cases where the aerodynamic roll angle,  $\phi$ , is either constant or the dipole configuration is axisymmetric and has no axial spin.

The centrifugal force due to chaff spiraling motion is quite small\*, and is balanced by the slight inclination of the normal force

---

\* This deduction is made from observation of dipole spiral motions. Comparing the calculated centrifugal force (obtained from  $CF = m R \Omega^2$ ) with the dipole weight, which is of the same order as  $F_N$ , it is found that  $CF$  is only 2 - 3 percent of  $F_N$ .

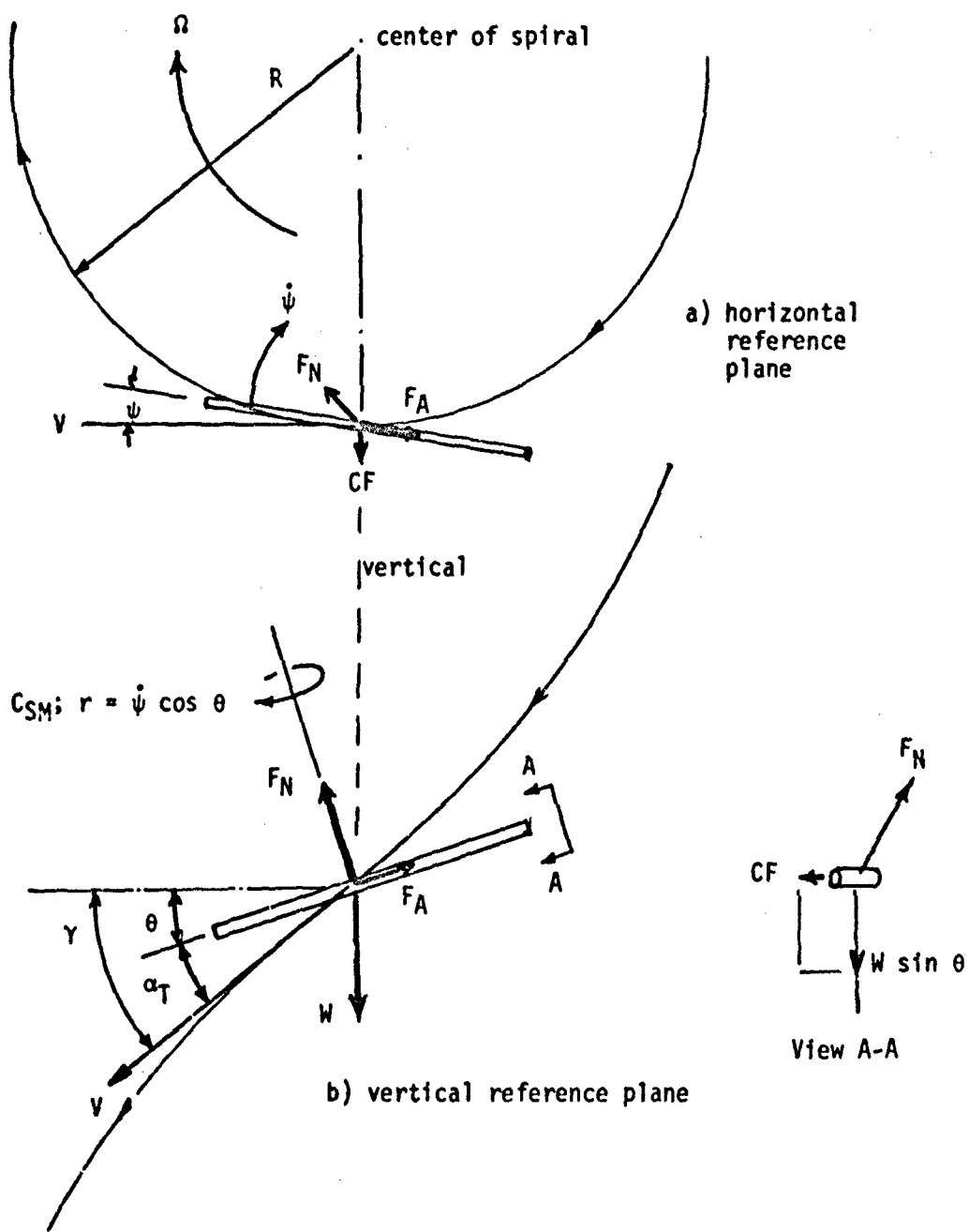


Figure C-8. Schematic of Forces and Moments Acting Upon a Spiraling Dipole

vector,  $F_N$ , from the vertical reference plane as shown in view A-A. The inclination of  $F_N$  is possible because of the small angle of yaw,  $\psi$ .

For steady-state spiral the attitude of the dipole relative to the instantaneous flight path remains constant. Thus the dipole rotation about its center-of-mass,  $\dot{\psi}$ , is also constant and identical to the spiral rate,  $\Omega$ . The yaw rate can be computed from

$$\dot{\psi} \cos \theta = \frac{\text{Side Moment}}{\text{Yaw Damping Moment}} \quad (\text{C-39})$$

which in coefficient form becomes

$$\dot{\psi} \cos \theta = r = \frac{C_{SM}}{C_{n_r}} \left( \frac{2V}{\lambda} \right) \quad (\text{C-40})$$

where  $C_{SM}$  and  $C_{n_r}$  are functions of  $\alpha_T$  and possibly  $\phi$ . The spiraling rate  $\Omega$  is

$$\Omega = \dot{\psi} = \frac{C_{SM}}{C_{n_r}} \left( \frac{2V}{\lambda \cos \theta} \right) \quad (\text{C-41})$$

Dispersion Due to Steady-State Spiral The radius of spiral,  $R$ , is most readily determined from the kinematic relationship

$$R = \frac{V \cos \gamma}{\Omega} \quad (\text{C-42})$$

where

$$V = \sqrt{\frac{2 W \sin \gamma}{\rho C_D S}} \quad (\text{C-43})$$

is the total velocity,

$$\gamma = \cot^{-1} \left( \frac{C_L}{C_D} \right) \quad (\text{C-44})$$

is the flight path angle and

$C_L$  = lift coefficient

$C_D$  = drag coefficient.

The lift and drag coefficients are functions of  $\alpha$  and possibly  $\phi$ .

The horizontal dispersion of a dipole from its release point,  $r$ , depends upon the descent distance. This is easily seen from Figure C-9. The general relationship for  $r$  is given by

$$r = 2R \sin \left( \frac{h}{2R} \frac{C_L}{C_D} \right) \quad (C-45)$$

The maximum radial dispersion is readily seen to be  $r = 2R$ . The descent distance for one complete spiral is obviously

$$h_1 = \frac{2\pi R}{C_L/C_D} \quad (C-46)$$

For  $h \gg h_1$  the probable value of radial dispersion,  $r$ , is found to be

$$\bar{r} = \frac{4}{\pi} R \quad (C-47)$$

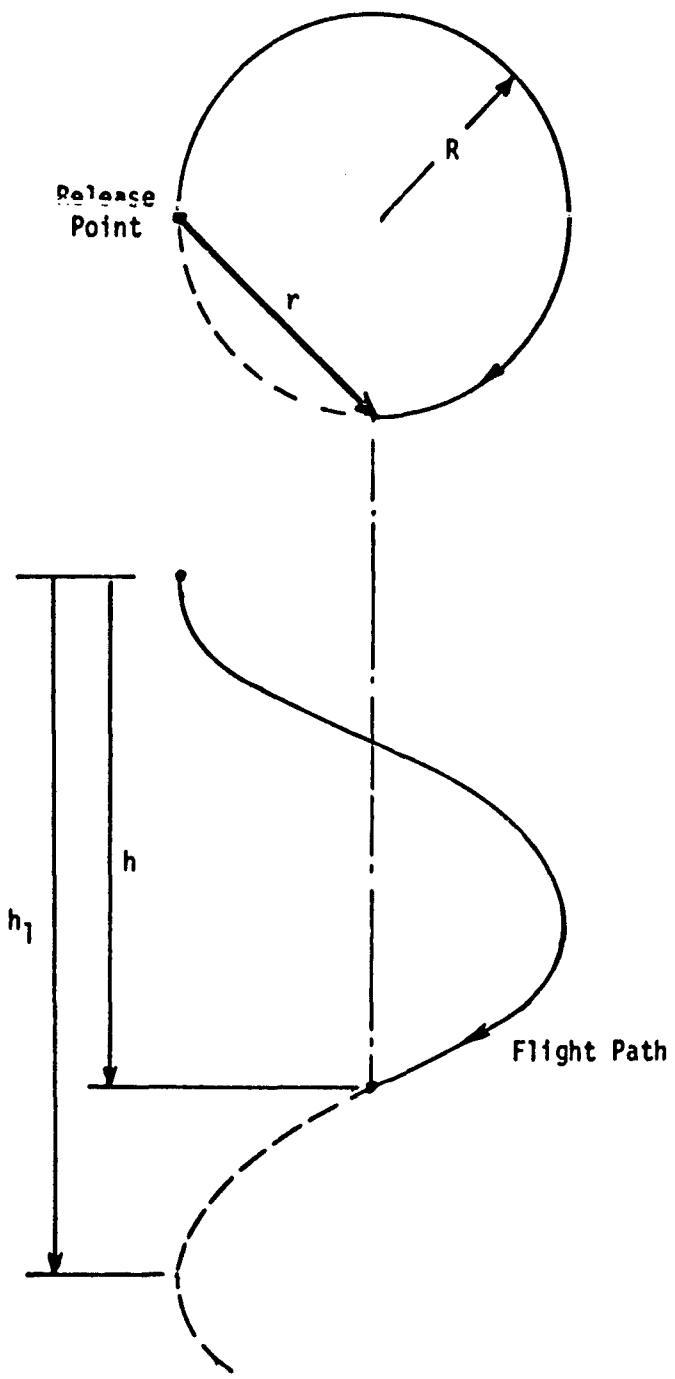


Figure C-9. Schematic of Dipole Dispersion Due to Steady Spiral

## APPENDIX D

### ISOTROPIC TURBULENCE

This appendix presents a method of digital computer modeling for isotropic three-dimensional turbulence applicable to chaff dipoles. The present turbulence model has greater similarity to the relationships for heavy particle diffusion than to the "frozen-flow" spectral models common in aircraft dynamics. Existing techniques for digital simulation of turbulence (primarily used in the aircraft industry) are inappropriate to the present study because of the extremely slow descent velocities of chaff dipoles.

The proposed turbulence model for chaff dynamics incorporates both spacial and temporal variations of the turbulent wind vector, and utilizes as input actual statistical spectral atmospheric turbulence measurements. A summary of the dimensional properties of atmospheric turbulence parameters is given in Appendix E.

The analyses which leads to the final set of equations which are used in the digital computer simulation are presented in this appendix. The statistical variables and functions are defined in Sections D-1 and D-2; the joint Lagrangian-Eulerian correlation function is presented in Section D-3; Section D-4 discusses the development of the equations for numerical digital simulation with the 6-DOF computer program.

#### 1. Eulerian Coordinates

Two distinct reference coordinates, Eulerian and Lagrangian, are commonly employed for identification of turbulence properties. The Eulerian\* reference is used in the overwhelming majority of theories and experiments, for example, the development of the Navier Stokes equations, and experimental measurements in wind tunnels, and from meteorological towers. Experiments in the Lagrangian coordinates are difficult because they involve measurements with respect to the mean fluid movement. However, developments in particle dispersion and air

---

\* The adjective "Eulerian" is used whenever correlations between two fixed points in a fixed frame of reference are considered.

pollution, including atmospheric measurements with tetroons (References 15 through 18), have recently yielded a variety of Lagrangian statistical properties.

With slowly falling particles, such as chaff, the incremental changes in both time and position affect the ever-changing turbulent flow field, as seen by the chaff particle. Herein lies the principal difficulty; that of combining or transferring between coordinates. To surmount this problem an approximate joint correlation has been developed and is presented later using statistical data for both Eulerian and Lagrangian coordinate systems.

The fluid velocities of the atmosphere,  $U$ ,  $V$ ,  $W$ , in the Euler coordinates  $X$ ,  $Y$ ,  $Z$ , as depicted in Figure D-1, are:

$$U = \dot{X}_w + U' \quad (D-1a)$$

where  $\dot{X}_w$  = mean wind velocity

and  $U'$  = turbulent velocity component.

To simplify the eventual relationships, the atmospheric mean wind is assumed to be only in the  $X$  direction. Thus, the other atmospheric velocities are:

$$V = V' \quad (D-1b)$$

$$W = W' \quad (D-1c)$$

Assuming, for example, a stationary, random, turbulent field for  $W'(\tau)$  over a time span of  $t$  seconds, the spacial power spectral density can be written:

$$\Phi(K) = \lim_{t \rightarrow \infty} \lim_{\Delta K \rightarrow 0} \frac{1}{2\pi t (\Delta K)} \int_0^t (W'_{\Delta K})^2(\tau) d\tau \text{ (ft}^3/\text{sec}^2) \quad (D-2)$$

where, in position space,  $K$ (cycle/ft) is the wave number. Similarly, a correlation function can be determined:

$$R(\rho) = \lim_{t \rightarrow \infty} \frac{1}{t} \int_0^t W'(z, \tau) W'(z + \rho, \tau) d\tau \text{ (ft}^2/\text{sec}^2)$$

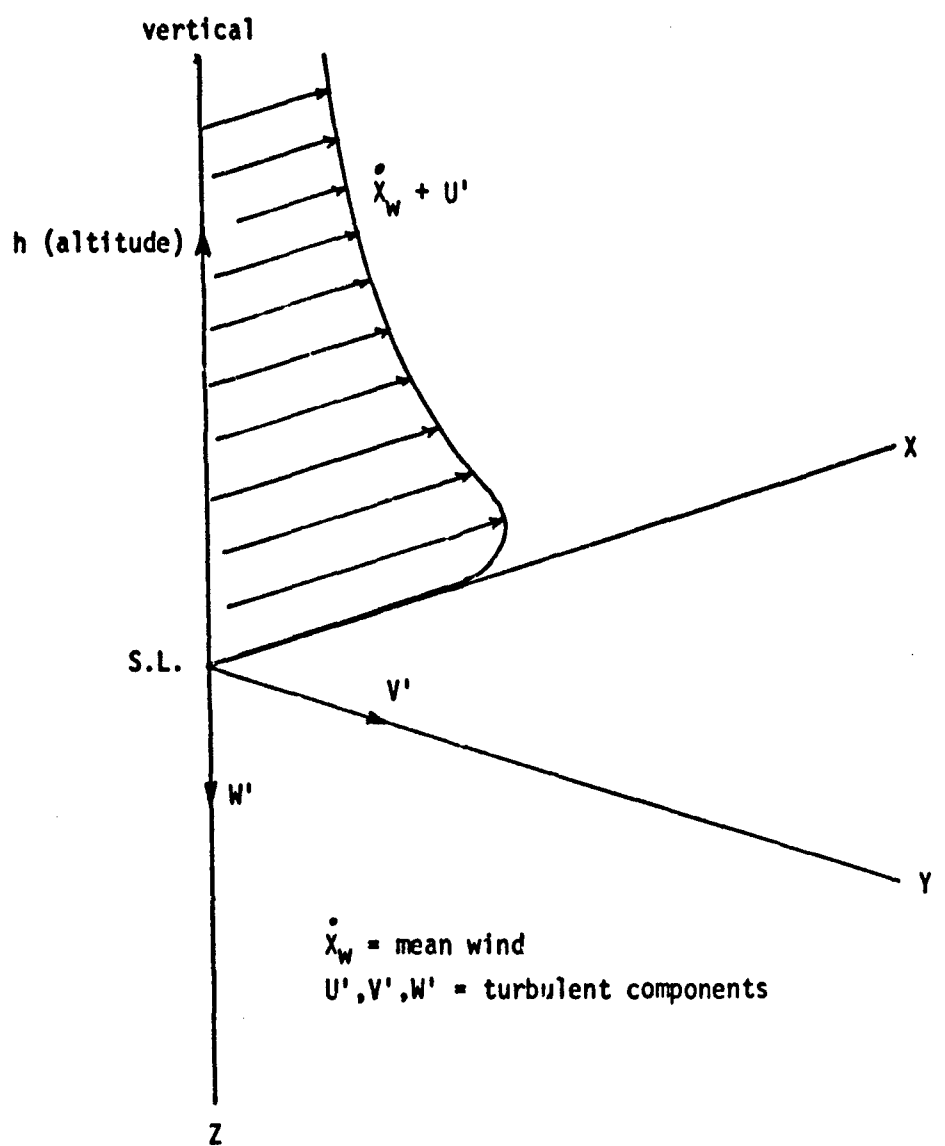


Figure D-1. Reference Coordinates and Turbulent Velocity Components

where  $\rho$  is the separation distance. The correlation coefficient will be denoted:

$$\bar{R}(\rho) = \overline{w'(z) w'(z + \rho)} \quad (D-3)$$

The over-bar refers to stochastic averages. The mean value of turbulence is:

$$\overline{w'} = \sqrt{\bar{R}(\infty)} = 0$$

The mean square value is:

$$\overline{\sigma_w^2} = \bar{R}(0)$$

Similar results are obtained for the  $U'$  and  $V'$  velocities.

Together with the level of turbulent fluctuations  $\sigma_w$  (rms), the most commonly referenced parameter in atmospheric measurements is the intensity:

$$i = \sigma_w / \bar{x}_w \quad (D-4)$$

A dimensional integral scale is also defined:

$$L_z = \int_0^\infty \frac{\bar{R}(\rho)}{\sigma_w^2} d\rho \quad (\text{ft}) \quad (D-5)$$

In the investigation (Reference 19) of high-Reynolds-number shear flow, a modified integral time constant on Eulerian space is determined to be:

$$\tau_E = \left| \frac{d\bar{x}_w}{dz} \right| + \sigma / L_z \quad (D-6)$$

In practice, statistical functions using the spacial correlation  $\rho$  are rarely considered. Rather, autocorrelation functions are employed, and time averages replace ensemble averages. "Taylor's hypothesis" (see Reference 20) is commonly referenced for this conversion. In this hypothesis, the turbulent flow is assumed to be "frozen" and transported with the mean flow. The turbulent components do not change with time (which implies that diffusion is not present). The frozen-flow modeling suggests that ensemble averages, the sequence of events at a

fixed point, are nearly equivalent to the movement of an unchanging pattern past this point. Also, past this point the wave number  $K$  is related to spacial frequency by velocity  $W$  (see Reference 15) with:

$$\omega = 2\pi KW$$

The time separation variable is:

$$\tau = \rho/W$$

The correlation function (symmetric about the origin) and the spectra become:

$$R(\tau) = \int_0^{\infty} \phi(\omega) \cos(\omega\tau) d\omega$$

$$\phi(\omega) = \frac{2}{\pi} \int_0^{\infty} R(\tau) \cos(\omega\tau) d\tau$$

Comparisons of spectra and correlation functions for the atmosphere are described in detail in Appendix E. The simplified correlation function used here is of the form:

$$R(\rho) = \sigma_w^2 \left( e^{-\rho/L_z} \right) \quad (D-7)$$

Although the utilization of the frozen-flow model is quite universal in the dynamic analysis of flight vehicles, it is shown in Reference 21 that this model is limited to vehicles which have an aerodynamic velocity,  $u_a$ ,  $v_a$ ,  $w_a$  in excess of approximately  $4\sigma$ , where  $\sigma$  is the rms turbulent velocity. Typically, the maximum aerodynamic velocity of chaff in the Stokes flow regime is

$$w_a \approx \dot{z} \approx 0 (\sigma) \quad (D-8)$$

and thus the criterion for frozen flow are not satisfied.

## 2. Lagrangian Coordinates

For chaff, the Eulerian modeling must be augmented with Lagrangian terms which describe the time variability of the atmospheric wind.

In Lagrangian space, an integral time constant is:

$$\tau_L = \int_0^\infty \frac{R(\tau)}{\sigma^2} d\tau$$

Reference 23 indicates that this time constant appears related to the Eulerian time constant,  $\tau_E$ . Therefore, the integral time scales can be related by a simple constant or function  $\beta$ , where:

$$\beta = \tau_L/\tau_E \quad (D-9)$$

Values of  $\beta$  from 0.3 to 10 have been reported in the literature, with values of 1 to 6 most prevalent. For turbulence intensities where  $i > 0.15$ , Reference 15 proposes the formulation:

$$\beta = 0.5/i$$

Data correlation for low intensities of turbulence at an altitude of 2500 feet were given in Reference 16 and correspond to the following:

$$\beta = e^{-6.5 i + 2.2} \quad (D-10)$$

Reference 26 discusses turbulence behavior at high Reynolds numbers and intensities, and arrives at:

$$\beta = 4.0$$

Reference 23 discusses simple relations for similarity at small micro-scales and arrives at:

$$\beta \approx 1.0$$

For generalized modeling with moderate to low turbulence intensities, Equations (D-6), (D-9), and (D-10) are combined to determine the Lagrangian time constant:

$$\tau_L = \frac{e^{-6.5 i + 2.2}}{\left| \frac{d \dot{X}_w}{d Z} \right| + \frac{\sigma}{L_Z}}$$

The Lagrangian correlation function (considered in References 23 - 25 and similar in form to Equation (D-7) is:

$$R(t) = \sigma^2 e^{-t/\tau_L} \quad (D-12)$$

### 3. Joint Correlation Functions

A joint Lagrangian-Eulerian correlation function is now defined which incorporates Equations (D-7) and (D-12):

$$R(t, \rho) = \sigma^2 \exp - \left\{ [a (t/\tau_L)^N + b (\rho/L_E)^N]^{1/N} \right\}$$

Values of  $N = 2$  and  $a, b = 1$  are chosen which yield "smooth" functions when  $t$  or  $\rho$  are nearly equal to zero (i.e., small micro-scales). Reference 16 discusses a similar form of the joint correlation function incorporating a time scale of  $\beta = 1$ . It is assumed that this joint correlation function is aligned with the mean wind. This orientation is acceptable when particle velocity is significantly larger than turbulent fluctuation. However, when the chaff particle velocity is of the order of  $\sigma$ , the aerodynamic velocity of the particle  $u_a$ ,  $v_a$ , and  $w_a$  may be equally large; thus any orientation ( $X$ ,  $Y$ ,  $Z$ ) might be denoted as the axis of principal correlation (i.e., the particle becomes lost in the eddy dynamics). However, in a statistical sense this is of little note when the direction of principal correlation is changed with time, because the eventual average direction corresponds to the  $Z$  direction (i.e.,  $\dot{X} - \dot{X}_w = 0$ ,  $\dot{Y} = 0$ ,  $\dot{Z} \neq 0$ ).

Therefore, the principal correlation function becomes:

$$R_p(t, \dot{z}) = \sigma^2 \exp - \left\{ (t/\tau_L)^2 + (t\dot{z}/L_E)^2 \right\}^{1/2} \quad (D-13)$$

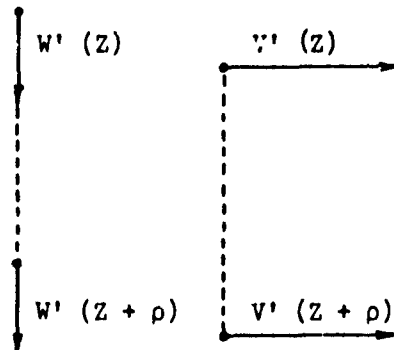
Secondary correlation functions in the  $X$  and  $Y$  directions are also required. These are obtained with the simplifying assumption that above the earth boundary layer the turbulence is isotropic (Reference 27, p. 28). For isotropic conditions the variances of the turbulent components are all equal, i.e. :

$$\overline{u'^2} = \overline{v'^2} = \overline{w'^2} = \sigma_o^2 \quad (D-14)$$

From Reference 28 (VonKarman) the primary and secondary correlation functions

$$R_L(\rho) = \overline{w'(z) w'(z + \rho)}$$

$$R_n(\rho) = \overline{v'(z) v'(z + \rho)}$$



are shown to have the well-known relationship

$$R_n(\rho) = R_L(\rho) + \frac{1}{2} \rho \frac{\partial R_L(\rho)}{\partial \rho} \quad (D-15)$$

The secondary correlation functions, Equations (D-16a), (D-16b) are obtained from Equations (D-13) and (D-15). Equation (D-13) is re-written as Equation (D-16c) which completes the following set of correlation functions for XYZ space:

$$R(t, \dot{x}) = \sigma_o^2 \left\{ 1 - \frac{t \dot{z}^2}{8 L_X^2 \left[ \frac{1}{\tau_L^2} + \left( \frac{\dot{z}}{2 L_X} \right)^2 \right]^{1/2}} \right\}$$

$$\exp \left\{ - t \left[ \frac{1}{\tau_L^2} + \left( \frac{\dot{z}}{2 L_X} \right)^2 \right]^{1/2} \right\} \quad (D-16a)$$

$$R(t, \dot{Y}) = \sigma_o^2 \left\{ 1 - \frac{t \dot{Z}^2}{8 L_Y^2 \left[ \frac{1}{\tau_L^2} + \left( \frac{\dot{Z}}{2 L_Y} \right)^2 \right]^{1/2}} \right\}$$

$$\exp \left\{ - t \left[ \frac{1}{\tau_L^2} + \left( \frac{\dot{Z}}{2 L_Y} \right)^2 \right]^{1/2} \right\} \quad (D-16b)$$

$$R(t, \dot{Z}) = \sigma_o^2 \exp \left\{ - t \left[ \frac{1}{\tau_L^2} + \left( \frac{\dot{Z}}{L_Z} \right)^2 \right]^{1/2} \right\} \quad (D-16c)$$

For isotropic flow, the scale lengths are related by the following (see Reference 28, Von Karman).

$$L_Z = 2L_X = 2L_Y \quad (D-17)$$

#### 4. Numerical Modeling

Turbulent flow is a random process, but unlike Brownian movement the fluid displays interaction and a memory between cells. When sampled over long time periods, turbulence processes display Gaussian number averages with the variance  $\sigma_o^2$ . The following generalized model is proposed which combines memory and randomness, and accommodates the correlation function (Equations (D-16a, b, c)).

$$U'_m = P U'_{m-1} + \sqrt{1 - P^2} G_m \quad (D-18a)$$

$$V'_m = Q V'_{m-1} + \sqrt{1 - Q^2} H_m \quad (D-18b)$$

$$W'_m = R W'_{m-1} + \sqrt{1 - R^2} J_m \quad (D-18c)$$

The values P, Q, R are memory functions, and  $G_m$ ,  $H_m$ ,  $J_m$  are random numbers chosen from a normal distribution of zero mean and standard deviation  $\sigma_o$ .

Equations (D-18a) through (D-18c) are in a particularly attractive form for digital modeling. The subscripts  $m$  and  $m-1$  respectively designate the stepwise present and previous values of the variable.

The following stochastic averages are formulated:

$$\begin{aligned}\overline{U_m^i U_{m-1}^i} &= \sigma_o^2 P \\ \overline{U_m^i U_{m-2}^i} &= \sigma_o^2 P^2 \\ \overline{U_m^i U_{m-3}^i} &= \sigma_o^2 P^3 \\ &\vdots && \vdots\end{aligned}\tag{D-19}$$

The correlation function which identifies the previous sequence is of the form:

$$R(t, \rho) = \sigma_o^2 P^N \tag{D-20}$$

where

$$N = t/\Delta t$$

Then the correlation function is simply:

$$R(t, \rho) = \sigma_o^2 e^{-\log\left(\frac{1}{P}\right)(t/\Delta t)} \tag{D-21}$$

where  $t$  = real time

and  $\Delta t$  = time increment used in 6-DOF computer program.

Memory terms  $P$ ,  $Q$ ,  $R$  can now be determined by equating Equation (D-21) to Equation (D-16a), etc., resulting in the following expressions:

$$P = \exp \left\{ -\Delta t \left[ A + \frac{\dot{z}^2}{8 L_X^2 A} \right] \right\} \tag{D-22a}$$

where

$$A = \left[ \frac{1}{T_L^2} + \left( \frac{\dot{Z}}{2 L_X} \right)^2 \right]^{1/2}$$

$$Q = \exp \left\{ - \Delta t \left[ B + \frac{\dot{Z}^2}{8 L_Y^2 B} \right] \right\} \quad (D-22b)$$

where

$$B = \left[ \frac{1}{T_L^2} + \left( \frac{\dot{Z}}{2 L_Y} \right)^2 \right]^{1/2}$$

$$R = \exp \left\{ - \Delta t \left[ \frac{1}{T_L^2} + \left( \frac{\dot{Z}}{L_Z} \right)^2 \right]^{1/2} \right\} \quad (D-22c)$$

Equations (D-18a, b, c) and (D-22a, b, c) were programmed into the 6-DOF analysis as a subroutine called TURB1. The random wind components, G, H, J are drawn from a subroutine called GAUSS. Currently, the values of  $L_X$ ,  $L_Y$ , and  $L_Z$ , and of  $\sigma_X$ ,  $\sigma_Y$ , and  $\sigma_Z$  are defined for the isotropic state, and are given by Equations (D-17) and (D-14), respectively. The program initiates with the three turbulent wind components all equal to zero.

It should be noted that the equations for turbulence, although involving the time increment  $\Delta t$  and chaff velocity  $\dot{Z}$ , are not integrated directly, but constitute a set of recursion formulas from which the chaff aerodynamic velocity components  $u_a$ ,  $v_a$ , and  $w_a$  are determined, and subsequently the chaff aerodynamic forces and moments. The differential equations of motion comprise only body velocities and accelerations resulting from these aerodynamic forces and moments.

For computational purposes, the time differential,  $\Delta t$ , appearing in Equations (D-22a, b, c) is taken as the integration interval. To avoid an indeterminacy at the start of the integration process, the turbulence velocities are not computed until after three Runge-Kutta integration steps (used to start the numerical integration of the equations of motion) are completed. Once initiated, the time dependency of the turbulence is forced to be singular, such that no ambiguity exists if a re-start of the main predictor-corrector integration scheme occurs.

The following NAMELIST format variables are incorporated in the computer data inputs for j argument values ( $j \leq 10$ ):

$$\dot{x}_W = WM(j)$$

$$\frac{\partial \dot{x}_W}{\partial h} = WDMDZ(j)$$

$$L_Z = WLSCL(j)$$

$$\sigma_0 = WSIG(j)$$

which are inputs at the altitude:

$$h = TABZ(j)$$

## APPENDIX E

### ATMOSPHERIC TURBULENCE DATA

Generally speaking, turbulence can be expected in a fluid when there is shearing flow and when inertial effects are much larger than viscous effects. In the atmosphere, the areas of principal wind shear are near the ground, in jet streams, storm cells, and clouds. Secondary shear layers are caused and influenced by geostrophic winds and thermal-buoyancy inequalities. There is an enormous quantity of measured data on these various situations.

Since this effort is concerned with "representative" behavior, an approximate model was formulated. Total meteorological detail is not within the scope of this effort; for example, non-isotropic flow behavior, such as jet streams, clouds, etc., are not considered (see Appendix D, Equation (D-14)).

Two generalized situations are discussed in this appendix. In Section 1, single valued variables define the free-atmosphere turbulence, i.e., for altitudes above the earth boundary layer.\* Section 2 describes several turbulence parameters as a function of altitude from sea-level to 40,000 feet.

#### 1. Single Valued Turbulence

The relevant data to the digital simulation equations are the principal scale of turbulence,  $L$ , and the standard deviation of turbulent velocity,  $\sigma_0$ . Reference 29 reviews the values of these two parameters as used in various theoretical turbulence ("frozen-flow") programs. Reference 30 gives a comprehensive data summary of medium-altitude turbulence measurement (MEDCAT). The principal dimensional values of turbulence obtained from these and other references are presented in Table E-1. The power spectral functions listed in this table are described in detail in Reference 30. All the spectral functions in the table are similar, with the exception of that from Reference 31. Reference 31 incorporates the Von Karman spectrum, generally accepted as the most accurate distribution function, particularly at the higher wave numbers. But this spectrum is a mathematically irrational function,

---

\* The earth boundary layer extends to 2000 - 5000 feet above ground height.

Table E-1. COMPILED DATA ON MEDIUM ALTITUDE  
TURBULENCE PROPERTIES

References	- L - (Ft)	$\sigma_0$ Ft/Sec	Power Spectral Functions
22	6000	6.9	Von Karman
23	5000	1.0	Dryden
24	1000-2000	6.0	Dryden
21	1000-2000	3.2	Taylor-Bullen
25	1000	1.0	Press-Meadows
20	200-300	3.2	Dryden

and so the simpler Dryden-type spectrum is used here (the actual numerical difference between the two is small). The Dryden principal and secondary spectral distribution functions are respectively:

$$\Phi_L(\Omega) = \frac{2\sigma_0^2 L_Z}{\pi} \left[ \frac{1}{1 + (L_Z \Omega)^2} \right] \quad (E-1)$$

$$\Phi_N(\Omega) = \frac{\sigma_0^2 L_Z}{\pi} \left[ \frac{1 + 3(L_Z \Omega)^2}{[1 + (L_Z \Omega)^2]^2} \right] \quad (E-2)$$

The spacial correlation function corresponding to Equation (E-1) is Equation (D-7) in Appendix D.

The choice of the scale parameters was based principally on the data in References 29 and 30. Reference 31 relates that, "Gust Models based on high-altitude turbulence are in general found to be too severe and unrealistic. Based upon pilot reactions from both fixed-base and flight-simulation studies, much lower values of gust severity and integral scale are indicated relative to those often quoted. Values of 3 ft/sec. for rms severity ( $\sigma_0$ ) instead of 6 or 8 ft/sec., and  $L = 200 - 300$  ft. rather than 2500 ft., were found to be much more realistic."

Reference 30 discusses the nonhomogeneous character of the real atmosphere in which turbulence is not uniformly distributed but concentrated in pockets (similar to CAT). The turbulent region is composed of two sections of Gaussian turbulence: a high-amplitude section which consists of 10 percent of the region with an rms value of 8 ft/sec, and a low-amplitude section made up of the other 90 percent with an rms value of 2. The entire region has a single value of  $\sigma_0 \approx 3.16$  ft/sec. for normal fit, which is quite typical of real turbulence. Figure E-1 shows an averaged model proposed for this situation in Reference 30, p. 139.

Figure E-2 shows normalized spectral distributions, (from Equation (E-1)) for three scale lengths  $L$ , and compares them with normalized data from Reference 30, p. 94. The amplitude of the experimental power spectral data is not precisely known because the spectrum is not measured to all wavelengths. A common method of correlation (Reference 30, p. 217) involves laying the observed spectrum over the theoretical curves and obtaining a match near the

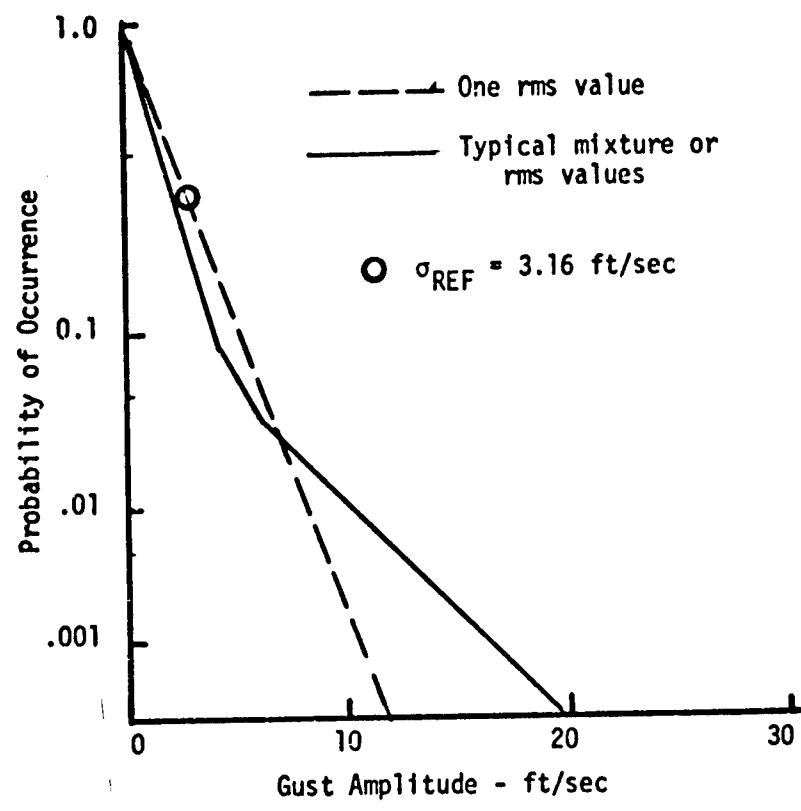


Figure E-1. Theoretical Mixture of Gaussian Amplitudes of Medium Altitude Atmospheric Turbulence

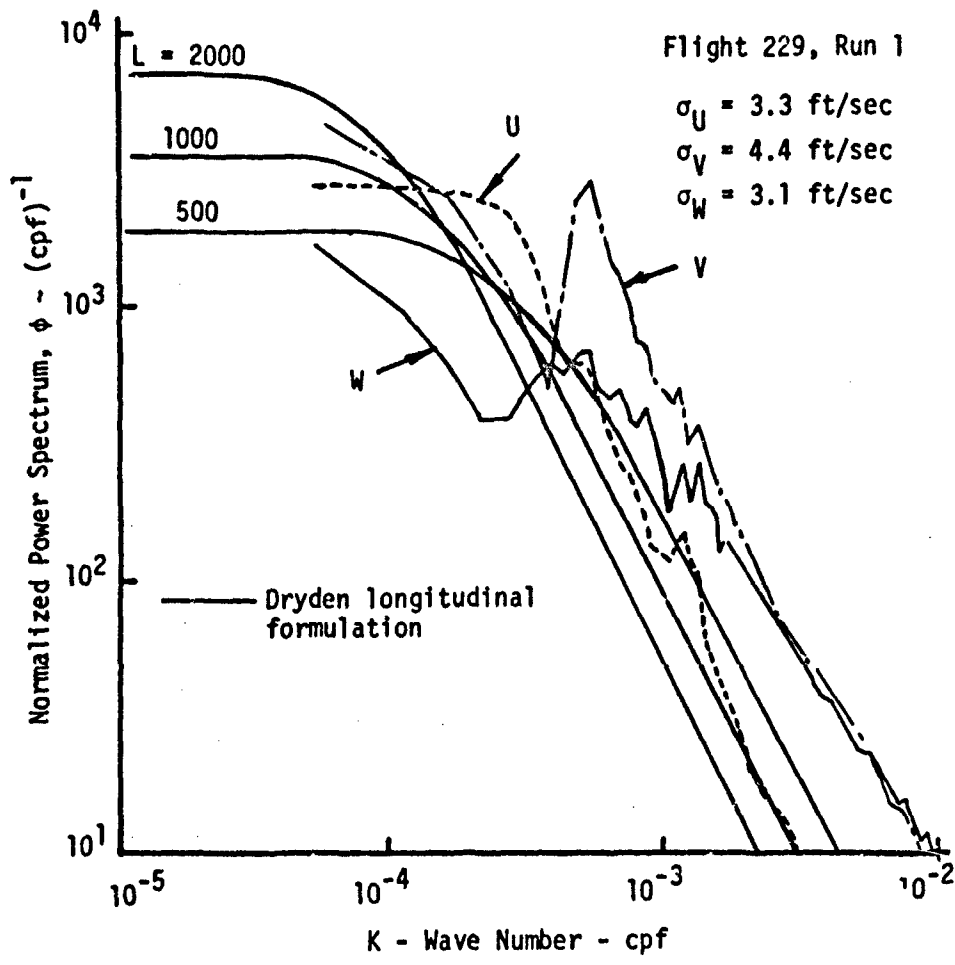


Figure E-2. Power Spectral Density of Turbulent Spectrum;  
Comparing Dryden Formulation to MEDCAT Data

"knee" area. Figure E-2 indicates a good correlation of slopes on both sides of the "knee". However, note that this case, with its different values for ( $\sigma_x$ ,  $\sigma_y$ , and  $\sigma_z$ ) is not truly isotropic.

For the most generalized situations above the earth boundary layer the following values are proposed for chaff dynamic modeling:

$$\begin{aligned}\sigma_o &= 3.0 \text{ ft/sec.} \\ L_z &= 500 \text{ ft.} \\ \dot{X}_w &\geq 40 \text{ ft/sec.}\end{aligned}$$

## 2. Turbulence as a Function of Altitude

The integral scale  $L_z$  and the rms turbulence,  $\sigma_o$ , are variables with altitude. However, above the earth boundary layer, the integral scale is generally assumed constant. The rms turbulence can be determined from the expression:

$$\sigma_o = i \dot{X}_w$$

where  $i$  is the turbulent intensity and  $\dot{X}_w$  is the mean wind velocity. Reference 35 discusses turbulent intensity in the free atmosphere, recommending a nearly constant value above the ground shear layer of:

$$i = 0.01 \text{ to } 0.03$$

Figure E-3, obtained from Reference 35, displays the uniform turbulent intensity above the ground layer ( $h = 2000$  to  $5000$  ft). The rms turbulence intensity is generally much larger within the boundary layer than within the free atmosphere, and it increases with ground proximity. Isotropic flow does not exist in the boundary layer where the rms turbulence values are different in the X, Y, and Z directions. Reference 29, p. 19 expresses rms turbulence in the boundary layer in terms of shear parameters. All three components are assumed to be identical with the value:

$$\sigma_o = 0.8 \dot{X}_w / \ln(h/Z_o) \quad (\text{E-3})$$

where  $Z_o$  is a height scale related to ground protuberances (typically  $1/30$  the characteristic dimension of the protuberance) chosen as  $0.116$  feet. Wind velocity,  $\dot{X}_w$ , for the neutrally stable condition (Reference 36) is calculated using the standard  $1/7$  power law:

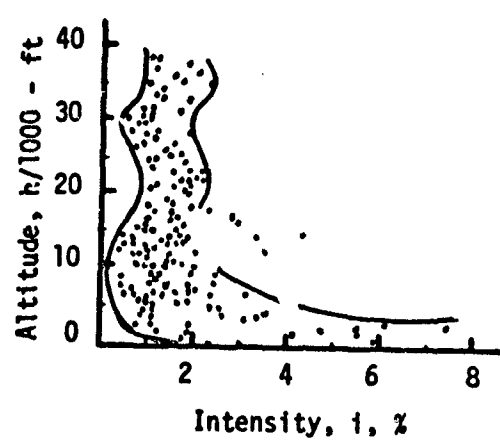


Figure E-3. The Nominal Intensity of Turbulent Fluctuations as a Function of Altitude

$$\dot{X}_w = \dot{X}_{w_0} (h/h_0)^{1/7} \quad (E-4)$$

The edge of the boundary layer is assumed to be at an altitude of  $h_0 = 5000$  ft, with a wind velocity of  $\dot{X}_{w_0} = 40$  ft/sec.

The integral length scale  $L_Z$  also varies within the earth boundary layer. Figure E-4 compares the integral scale length variations with altitude. The orders of magnitude of change reflect the radical differences between the ground layer and the free atmosphere. References 37 and 38 express the length scale as:

$$L_Z = 0.4 h \quad (h < 465 \text{ ft}) \quad (E-5)$$

$$L_Z = 2.1 h^{0.73} \quad (465 \text{ ft} < h < 1300) \quad (E-6)$$

Table E-2 summarizes the turbulence parameters incorporated into the chaff dynamic model for preliminary studies, as obtained from the previously discussed equations. These turbulence values are only approximate representations - the fundamental variability of atmospheric flow precludes modeling every situation. The use of specific statistical data instead of this generalized model is recommended whenever experimental and theoretical correlation of dynamic behavior or dispersion is being performed.

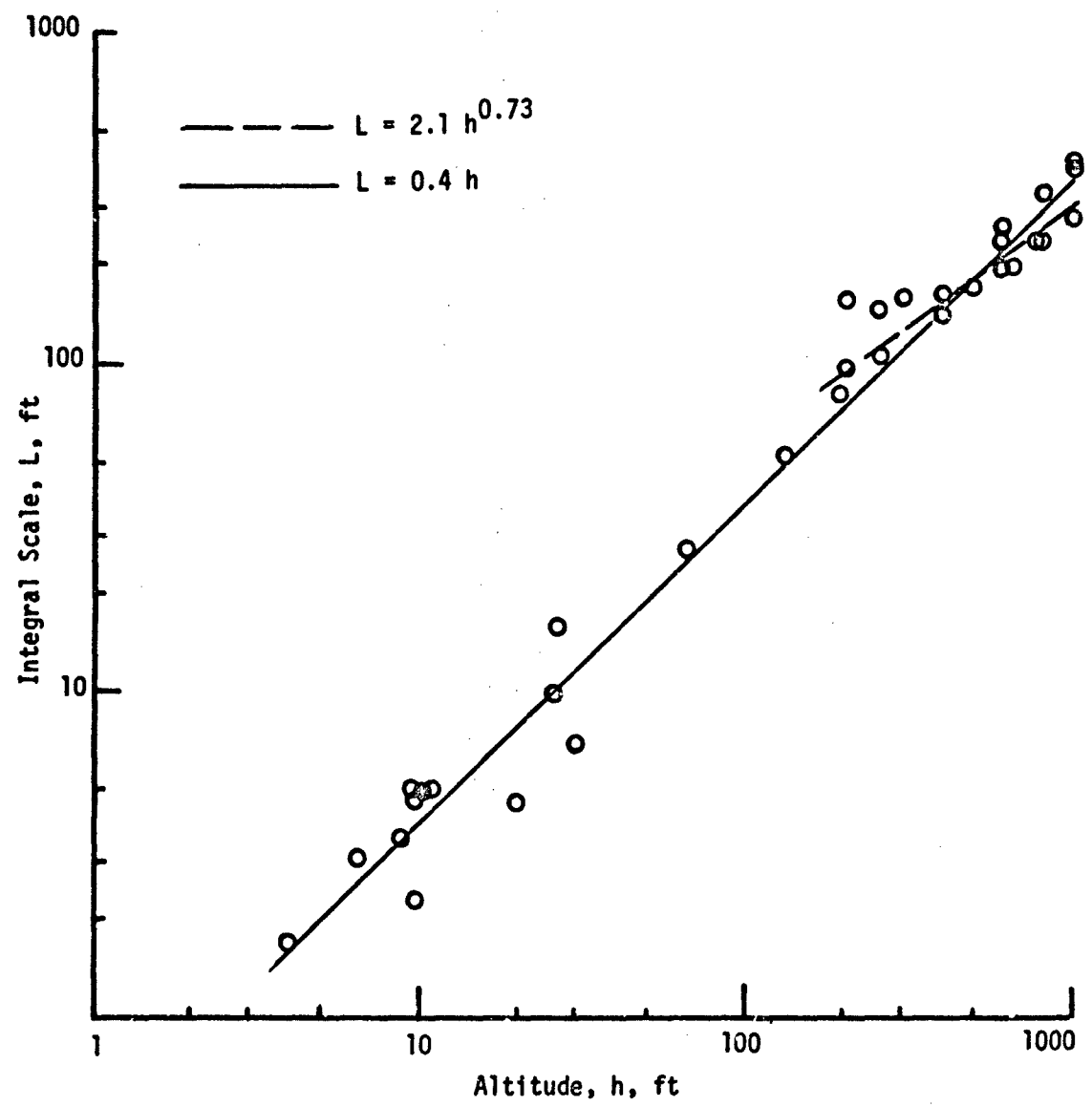


Figure E-4. Turbulent Scale Length Variation with Altitude in Neutral Stability Over Flat Terrain

Table E-2. TURBULENCE PARAMETERS WITH NEUTRALLY STABLE CONDITIONS USED IN THE COMPUTER NAMELIST INPUT

j	h (TABZ) Ft	$\dot{X}_w$ (WM) Ft/Sec	$\sigma_o$ (WSIG) Ft/Sec	$L_z$ (WLSCL) Ft	$\left  \frac{\partial \dot{X}_w}{\partial h} \right $ (WDMDZ) Ft/Sec/Ft
1	0	0	--	0	--
2	25	18.7	2.78	80	.748
3	200	25.3	2.71	325	.0377
4	1,000	32	2.8	500	.0084
5	5,000	40	3.0	500	.002
6	10,000	60	2.25	500	.004
7	15,000	40	2.5	500	.004
8	20,000	40	3.0	500	0
9	30,000	80	2.4*	500	.004
10	40,000	60	1.8*	500	.002

$$* \sigma_o = 0.03 \dot{X}_w$$

( ) parenthetical quantities are NAMELIST variables as described in Appendix D.

## REFERENCES

1. Arvin, J. S. and M. V. McCafferty, The KMS Technology Center, "Chaff Cloud Dynamics," Air Force Avionics Laboratory, Wright-Patterson AFB, Ohio, Report No. AFAL -TR-73-286, September 1973.
2. Alpha Research, Inc., "User's Manual: Extended Capability Magnus Rotor and Ballistic Body 6-DOF Trajectory Program," Report No. AFATL-TR-70-40, May 1970.
3. Alpha Research, Inc., "Amended User's Manual: Extended Capability Magnus Rotor and Ballistic Body 6-DOF Trajectory Program," Alpha Research Report No. 71-2, 26 March 1971.
4. Alpha Research, Inc., "6-DOF Monte Carlo Trajectory Program," Alpha Research Report No. 72-6089-10, 29 September 1972.
5. Mihora, D. J., Astro Research Corp., "Photogrammetry of Minute Chaff Elements in a Quiescent Test Chamber," Astro Research Report No. ARC-TM-320, October 3, 1974.
6. Lagerstrom, P. A., Laminar Flow Theory, "Theory of Laminar Flow," Vol. IV. High Speed Aerodynamics and Jet Propulsion, Princeton, New Jersey, Princeton University Press, 1964.
7. Tomotika, S., and T. Aoi (University of Kyoto, Japan), "The Steady Flow of Viscous Fluid Past a Sphere and Circular Cylinder at Small Reynolds Numbers," Quart. Journ. Mech. and Applied Math., Vol. III, Pt. 2 (1950).
8. Cox, R.G., "The Steady Motion of a Particle of Arbitrary Shape at Small Reynolds Number," Journal of Fluid Mechanics (1965), Vol. 23, Part 4, pp 625-643.
9. Tomotika, S. and T. Aoi (Univ. of Kyoto, Japan), "The Steady Flow of a Viscous Fluid Past an Elliptic Cylinder and a Flat Plate at Small Reynolds Numbers," Quart. Journ. Mech. and Applied Math., Vol. VI, Pt. 3 (1953).
10. Willmarth, W. E., et al, "Investigations of the Steady and Unsteady Motion of Freely Falling Disks," Aerospace Research Laboratories Report No. ARL 63-176, October 1963, AD 420 913.

#### REFERENCES (Continued)

11. Lamb, Sir Horace, "Hydrodynamics," Sixth Edition, Dover Publications, New York.
12. Happel, John, and Howard Brenner, "Low Reynolds Number Hydrodynamics," Prentice-Hall International Series in the Physical and Chemical Engineering Sciences, Prentice-Hall, Inc., Englewood Cliffs, N. J.
13. Glauert, M. B. and M. J. Lighthill, F. R. S., "The Axisymmetric Boundary Layer on a Long Thin Cylinder," Proceedings of Royal Society of London, Series A. Mathematical and Physical Sciences, 12 July 1955.
14. Imai, Isao, (Univ. of Tokyo, Japan), "A New Method of Solving Oseen's Equations and Its Application to the Flow Past an Inclined Elliptic Cylinder," Proceedings of Royal Society, A 224 (1954), pg. 141.
15. Pasquill, F., "Atmospheric Diffusion," Van Nostrand Publishers, London, 1962.
16. Angell, J. K., "Measurements of Lagrangian and Eulerian Properties of Turbulence at a Height of 2500 Feet," Quarterly Journal of the Royal Meteorological Society, Vol. 90, No. 383, January 1974.
17. Angell, J. K., "Lagrangian-Eulerian Time Scale Ratios Estimated from Constant Volume Balloon Flights Past A Tall Tower," Quarterly Journal of the Royal Meteorological Society, Vol. 97, No. 411, January 1971.
18. Notes and telecons on Lagrangian-Eulerian time scale relationships from J. K. Angell.
19. Riley, J., and Corrsin, S., "The Relation of Turbulent Diffusivities to Lagrangian Velocity Statistics for the Simplest Shear Flow," Journal of Geophysical Research, Vol. 79, No. 12, April 1974.
20. Batchelor, G. K., "Homogeneous Turbulence," Cambridge University Press, 1960.

#### REFERENCES (Continued)

21. Csanady, G. T., "Turbulent Diffusion of Heavy Particles in the Atmosphere," *Journal of Atmospheric Sciences*, Vol. 20, May 1963.
22. Meek, C. C. and Jones, B.G., "Studies of the Behavior of Heavy Particles in a Turbulent Flow Field," *Journal of Atmospheric Sciences*, Vol. 30, March 1973, p. 239.
23. Shlien, D. J. and Corrsin, S., "A Measurement of Lagrangian Velocity Autocorrelation in Approximately Isotropic Turbulence," *Journal of Fluid Mechanics*, Vol. 62, 1974, pp. 255-271.
24. Riley and Patterson, "Diffusion Experiments with Numerically Integrated Isotropic Turbulence," *Physics of Fluids*, Vol. 17, 1974, pp. 292-297.
25. Snyder, W. H. and Lumley, J. L., "Some Measurements of the Particle Velocity Autocorrelation Functions in a Turbulent Flow," *Journal of Fluid Mechanics*, Vol. 48, 1971, pp 41-71.
26. Corrsin, S., "Estimates of the Relations Between Eulerian and Lagrangian Scales in Large Reynolds Number Turbulence," *Journal of Atmospheric Sciences*, March 1963.
27. Reynolds, A. J., "Turbulent Flows in Engineering," J. Wiley Publishers, 1974.
28. Friedlander and Topper, ed, "Turbulence - A Collection of Classic Papers," Interscience Publishers, 1961.
29. Houbolt, J. C., "Survey on the Effects of Surface Winds on Aircraft Design and Operation and Recommendations for Needed Wind Research," NASA CR-2360, December 19, 1973.
30. Ryan, J. P., et al, "Medium Altitude Critical Atmospheric Turbulence (MEDCAT) Data Processing and Analysis," University of Dayton Research Institute, AFF-DL-TR-71-82, AD 732 878, July 1971.
31. Gordon, C. K., and Dodson, R.O., "STOL Ride Control Feasibility Study," Technical Report, NASA CR-2276, July 1973.

REFERENCES (Concluded)

32. Porter, R. F., et al, "A Procedure for Assessing Aircraft Turbulence Penetration Performance," NASA CR-1510, March 1970.
33. Lichtenstein, J. H., "Computed Lateral Power Spectral Density Response of Conventional and STOL Airplanes to Random Atmospheric Turbulence," NASA TN-D-744, March 1974.
34. Edinger, et al, "Study of Load Alleviation and Mode Suppression on the YF-12A Airplane," NASA CR-2158, December 1972.
35. Vinnichenko, et al, "Turbulence in the Free Atmosphere," New York Consultants, Bureau Translations, New York, 1973.
36. Counihan, J., "Aerodynamics of Atmospheric Shear Flow," AGARD Conference Proceedings, No. 48, Hartford House, 1970.
37. Luers, J. K., "A Model of Wind Shear and Turbulence in the Surface Boundary Layer," NASA CR-2888, 1973.
38. Etkin, B., "Dynamics of Atmospheric Flight," Wiley and Sons, 1973.

SUPPLEMENTAI

INFORMATION

DEPARTMENT OF THE AIR FORCE  
AIR FORCE WRIGHT AERONAUTICAL LABORATORIES (AFSC)  
AIR FORCE AVIONICS LABORATORY  
WRIGHT-PATTERSON AIR FORCE BASE, OHIO 45433



REPLY TO  
ATTN OR  
TSR (G. Doben)

3 February 1976

SUBJECT: Changes to AFAL-TR-75-81

to. DDC/TSR.  
ALL HOLDERS OF AFAL-TR-75-81

Please make the following changes to AFAL-TR-75-81:

In the text of the report (pages 17 - 70), citations to figure numbers 7 through 28 are in error. The correct citations are 6 through 27, respectively. The numbering on the figures themselves is correct, however.

FOR THE COMMANDER

JAMES G. JOHNSON, Chief  
STINFO Branch  
Technical Services Division  
AF Avionics Laboratory

